
Fatigue Prediction and Response Monitoring on A FPSO

Proefschrift

ter verkrijging van de graad van doctor
aan de Technische Universiteit Delft,
op gezag van de Rector Magnificus prof.dr.ir. J.T. Fokkema,
voorzitter van het College voor Promoties,
in het openbaar te verdedigen

op maandag 28 januari 2008 om 15.00 uur

door

Jerome Johannes VAN DER CAMMEN

maritiem ingenieur

geboren te Rotterdam

Dit proefschrift is goedgekeurd door de promotor:

Prof. dr. ir. J.A. Pinkster

Toegevoegd promotor: Ir. G. Hommel

Samenstelling promotiecommissie:

Rector Magnificus,	Voorzitter
Prof. dr. ir. J.A. Pinkster,	Technische Universiteit Delft, Promotor
Ir. G. Hommel,	Technische Universiteit Delft, toegevoegd promotor
Prof. Dr. ir. R.H.M. Huijsmans,	Technische Universiteit Delft
Prof. ir B. Boon,	Universität Duisburg-Essen
Prof. Dr. W. Fricke,	Technische Universität Hamburg-Harburg
Dr. ir. M.L. Kaminski,	Maritime Research Institute Netherlands
Ir R. Uittenbogaard,	Bluewater Energy Services B.V.
Prof. ir. J. Meek,	Technische Universiteit Delft, reservelid

ISBN 978-90-8559-345-4

Copyrights © 2007 by J.J. van der Cammen

Printed by Optima Grafische Communicatie BV, Rotterdam

Contents

Contents		iii
Summary		vii
Samenvatting		ix
Acknowledgements		xi
Nomenclature		xii
Abbreviations		xvi
1	Introduction	1
1.1	Problem Overview	1
1.2	Fatigue and Structural Integrity Management	3
	1.2.1 Structural Integrity Systems	3
	1.2.2 Fatigue Design Methodology	3
	1.2.3 Integrity Management during Construction	5
	1.2.4 Integrity Management during Operations	5
1.3	Background to Research	6
1.4	Scope of Work	8
2	Model Development for Fatigue Life Calculation	9
2.1	Fatigue Capacity	10
	2.1.1 SN-Curve Data	10
	2.1.2 Stress at the Fatigue Hotspot	11
	2.1.3 Nominal Stress	12
	2.1.4 Stress Factors for Local Geometry and Welding	13
2.2	Environmental Description	14
	2.2.1 Environmental Data Sources	14
	2.2.2 Modelling of Wave Conditions	16
2.3	Loading Conditions	18
2.4	Orientation of Vessel in a Sea-State	20
	2.4.1 Literature	20
	2.4.2 Adapted Calculation Procedure	21
	2.4.3 Full-Scale Validation	24

2.5	Wave Pressure Loading	26
2.5.1	Literature	26
2.5.2	Numerical Modelling	28
2.5.3	Modeltest Validation of Pressure Model	29
2.5.4	Full-Scale Model Validation	33
2.6	Calculation of Global Loads	38
2.7	Cargo Pressures	38
2.8	Long-term Stress Distribution	43
2.8.1	Calculation of Relative Wave Elevations	43
2.8.2	Calculation of Stress Responses	47
2.8.3	Long-Term Stress Distribution	50
3	Application of Long-Term Fatigue Model	52
3.1	Length of Time-Traces	52
3.1.1	Fatigue Accumulation in a Sea-State	53
3.1.2	Distributions of Stochastic Parameters in a Sea-State	56
3.1.3	Fatigue Accumulation through Sea-States	63
3.1.4	Fatigue Accumulation on the Side-Shell	64
3.2	Contribution of Loads	69
3.2.1	Phase Relations	71
3.3	Wave Diffraction and Radiation	72
3.4	Roll Damping	73
3.4.1	Physics of Roll Damping	73
3.4.2	Effect of Roll Damping on Fatigue	74
3.5	Environmental Conditions	78
3.5.1	Accumulated Load as Function of Significant Wave Height	78
3.5.2	Contribution of Wind Waves and Swell	79
3.5.3	Format of Environmental Data	80
3.5.4	Wave Spreading	83
3.6	Vessel Loading Condition	84
4	Fatigue Monitoring Systems	86
4.1	Introduction	86
4.2	Monitoring Systems in Shipping and Offshore Industry	87
4.2.1	Structural Monitoring onboard Naval Vessels	87
4.2.2	Structural Monitoring onboard Tankers	89
4.2.3	Structural Monitoring for Inspection, Maintenance and Repair Programs	91
4.2.4	Monitoring of Structural Damage	92
4.2.5	Monitoring of Weather Conditions on-board Offshore Units	93

4.3	General Discussion for Fatigue Monitoring Systems	94
4.3.1	Purpose of Fatigue Monitoring	94
4.3.2	Functional Requirements of Fatigue Monitoring System	95
4.3.3	Components of FMS	96
4.3.4	Data Processing Techniques for FMSs	98
4.4	Time Domain Methods	99
4.5	Wave Spectrum Methods	99
4.6	Statistical Methods	101
4.6.1	Statistical Correlation Method between Responses	102
4.6.2	Linear Correlation Method	106
4.6.3	Neural Network Method	107
4.6.4	Application of Linear Correlation Method	110
4.6.5	Application of the Neural Network Method	116
4.7	Summary of Results	121
5	Application of Fatigue Model and Fatigue Monitoring System	123
5.1	The Fatigue Monitoring System and Structural Integrity management	123
5.2	Set-Up of Case Study	125
5.3	Long-term Load Calculations	126
5.3.1	Environmental Data and Loading Conditions	126
5.3.2	Measured Response Data	126
5.3.3	Calculation Procedure	128
5.3.4	Calculated Vessel Heading	130
5.3.5	Comparison of Measured and Calculated Response Statistics	131
5.3.6	Discussion of Comparison measurement vs. calculations	136
5.4	Correlation between Response Statistics	137
5.4.1	Measured Response Data	137
5.4.2	Calculation Procedure	138
5.4.3	Calculation Results	140
5.4.4	Summary of Results	147
6	Conclusions and Recommendations	148
6.1	Conclusions	148
6.2	Recommendations	149
	References	151

Appendices

A	Data for Long-Term Load Calculations	162
A.1	Diffraction Calculations in FPSO Integrity JIP	162
A.2	Motion Calculations for Operational Loading Conditions	167
A.3	Structural Data	168
A.4	Environmental Data	170
A.4.1	Sable Field	170
A.4.2	Durward & Dauntless Field	172
B	Sensor Locations	174
	Curriculum Vitae	176

Fatigue Prediction and Response Monitoring on A FPSO

Jerome Johannes van der Cammen

Summary

The fatigue life of structural members is an important aspect in the hull design of a Floating Production Storage and Offloading unit (FPSO). In contrast to the design for ultimate conditions, a fatigue assessment requires a thorough knowledge of the long-term environment to which the unit is exposed and how the unit is operated to estimate an accurate long-term load distribution. Furthermore, the fatigue life of a structural member is sensitive to the load to which it is exposed. This makes that an accurate long-term load distribution must be available to calculate an accurate fatigue life calculation.

In this thesis, a model is investigated and developed to calculate the fatigue life of structural members in the side-shell, deck and bottom of a FPSO. The model is developed in the time-domain and validated against available model test data and full-scale measurement data recorded at FPSO Glas Dowl during operations at the Durward & Dauntless field (UKCS) and the Sable field (offshore South-Africa). It is demonstrated that the individual sea-states can be represented by short time-series, because many sea-states need to be taken into account in a fatigue assessment. This makes the fatigue calculations in time-domain feasible from a computational point of view. In chapter 3, long-term fatigue calculations for a period of a year will be discussed where the sea-states are represented by 3-hours periods and by 200 second periods. Both calculations show similar results, but the calculation time of the 200 second simulations was finished in less than 2 hours, where the 3-hour sea-state simulations required a computational time of approximately 4.5 months.

The sensitivity of the fatigue life in the model is investigated. It is found that the accuracy of the environmental data and loading condition data with which the model is fed, are equally important as the model itself. The vessel is designed with historical environmental data, but the vessel is likely to encounter different environmental conditions during its time at the field. Furthermore, the vessel will most likely be operated differently than assumed in the fatigue calculations. Both parameters have a significant impact on the fatigue life. Therefore, for offshore inspection, maintenance and repair (IMR) and for life-time extension (LTE) work at a yard for the next field, it is of interest to record the loads that the vessel encountered.

In the second part of this thesis, data processing techniques are investigated to derive load accumulation data at specified locations from recorded sensor data. In particular, a processing technique is investigated that quantifies the long-term correlations between the statistics of different vessel responses. The basis of this technique is that all vessel responses are induced by the same wave conditions. In storm conditions all vessel responses will be large where in calm sea-states all vessel responses will be small. This suggests that a long-term relation between the statistics of different vessel responses exists. The developed method aims at describing this long-term relation. Potentially, this technique can lead to a practical and relatively inexpensive monitoring system, since this technique provides the possibility to derive load data in the structure from a limited number of conveniently placed sensors.

The nature of the long-term relations is investigated in this thesis. These long-term relations are derived from example data that can be measured data, or from calculated data. A linear correlation method and a neural network to quantify these long-term relations are investigated. It is found that the methodology works better if the set with example data to derive the correlations is representative and if the measured response and target response are physically closer related. For instance, the vertical wave bending moment is closer related to the pitch motion of the vessel than to the roll motion. Consequently, it is better to predict deck strains from measured pitch motions than from measured roll motions. The neural network was found to be the better method of both, particularly for responses that are physically less correlated and in less representative example data-sets to derive the correlations.

Vermoeiingsvoorspelling en Responsie Meting op een FPSO

Jerome Johannes van der Cammen

Samenvatting

Het vermoeiingsleven van constructieve onderdelen in de romp is een belangrijk onderdeel in het ontwerp van een FPSO (Floating Production, Storage and Offloading) romp. In tegenstelling tot het ontwerp in extreme condities vereist een vermoeiingsanalyse gedetailleerde kennis van de lange termijn omgevingscondities waar het schip aan onderhevig is en hoe de FPSO gebruikt wordt, om een nauwkeurige lange termijn belastingsverdeling te kunnen berekenen. Het vermoeiingsleven van een constructief onderdeel is ook gevoelig voor de belasting waar het onderdeel aan onderhevig is. Dit maakt dat een nauwkeurige lange termijn belastingverdeling nodig is om een nauwkeurige vermoeiingsberekening te maken.

In dit proefschrift wordt een model onderzocht en ontwikkeld om het vermoeiingsleven van structurele onderdelen in de huid, het dek en de bodem van een FPSO te berekenen. Het betreft een tijdsdomein model dat is gevalideerd met beschikbare modeltest data en data gemeten op FPSO Glas Dour, gedurende operaties op het Durward&Dauntless veld (Noordzee, Engelse plat) en op het Sable veld (offshore Zuid-Afrika). De golfcondities kunnen worden beschreven met korte tijdreeksen, omdat er veel golfcondities moeten worden meegenomen in de vermoeiingsberekening. Hierdoor wordt een vermoeiingsberekening in tijdsdomein mogelijk. In hoofdstuk 3 worden lange termijn vermoeiingsberekeningen besproken, waar de golfcondities worden beschreven met tijdreeksen van zowel 3 uur en 200 seconden. Beide berekeningen geven soortgelijke resultaten, maar de berekeningen met 200 seconden waren binnen 2 uur afgerond, terwijl er voor de 3-uurs simulaties een berekeningstijd van ongeveer 4.5 maand nodig was.

De gevoeligheid van het vermoeiingsleven in het model is onderzocht. Hieruit bleek dat de nauwkeurigheid van de omgevingsdata en beladingsconditie data als invoer voor het model even belangrijk zijn als het model zelf. Het schip wordt ontworpen op basis van historische omgevingsdata, maar het is zeer waarschijnlijk dat de golf condities die de FPSO ziet, anders zijn dan deze ontwerpcondities. Ook is het heel waarschijnlijk dat het schip anders geopereerd wordt dan aangenomen in het ontwerp. Beide parameters hebben een aanzienlijke invloed op het vermoeiingsleven. Om deze reden is het wenselijk voor offshore inspectie, onderhoud en reparatie werkzaamheden en voor conversie werkzaamheden op een werf voor een volgend veld om de belastingen op het schip te meten.

In het tweede deel van dit proefschrift worden dataverwerkingstechnieken onderzocht om belastingdata op locaties af te leiden uit gemeten sensor data. In het bijzonder wordt gekeken naar een dataverwerkingstechniek die een lange-termijn relatie tussen de statistieken van verschillende scheepsresponsies beschrijft. De basis van deze techniek is dat alle scheepsresponsies door dezelfde golfcondities worden veroorzaakt. In stormcondities zijn alle responsies groot terwijl in rustig weer alle responsies klein zijn. Dit impliceert dat er een lange-termijn verband tussen de statistieken van verschillende responsies bestaat. De ontwikkelde methode beschrijft deze relatie. In potentie kan deze techniek leiden tot een praktisch en kosteneffectief meetsysteem, omdat deze methodiek de mogelijkheid biedt om belastingdata in de constructie af te leiden van een beperkt aantal makkelijk plaatsbare sensoren.

De aard van deze lange-termijn relaties wordt onderzocht in dit proefschrift. De relaties worden afgeleid uit een hoeveelheid voorbeelddata dat zowel berekende als gemeten data kan zijn. Een lineaire correlatiemethode en een neurale netwerk worden onderzocht om deze relatie te bepalen. De lange-termijn correlatie methodiek blijkt beter te werken als de voorbeelddata representatief is en als de gemeten en berekende responsies fysisch nauwer verwant zijn. Zo is bijvoorbeeld het golfbuigend moment nauwer verwant met de stampbeweging van het schip dan met de slingerbeweging en is het beter om de rekken in het dek te voorspellen met gemeten stampbewegingen dan met slingerbewegingen. Het neurale netwerk blijkt de betere methode, zeker als het toegepast wordt op responsies die fysisch minder nauw gerelateerd zijn en met minder representatieve voorbeelddata om de correlaties uit af te leiden.

Acknowledgements

At the end of five years of hard work, I look back with much pleasure to an interesting and fruitful period. Doing a PhD research next to work is not always easy, but in the end it turned out to be most rewarding. Not only could I gain a lot of theoretical knowledge from university, but I could also gather practical experience in a design environment and get feedback from the crew at the Bluewater vessels. All provided valuable feedback and input for this thesis work. It was quite a challenge to get the theoretical models on the same page with the offshore practices/views, but in the end it worked out.

I like to thank Bluewater to give me the opportunity to do my PhD work and provide the time and resources. Thanks to all my colleagues, for their interest and support. In particular, I would specially like to thank Clemens van der Nat, Ries Uittenbogaard and Jaap de Baan for their continuous support over the years. Thanks guys!

I like to thank my supervisors, Jo Pinkster, and Guus Hommel, for their continuous support in the work. I also like to thank Co Vink, your comments and reviews were most valuable.

I like to thank MARIN for the continuous efforts in the development in the field of fatigue and the efforts in the data processing for the Glas Dowl measurement system. In particular, I like to thank Mirek Kaminski, Pieter Aalberts and Abdel El Mouhandiz. I'm looking forward to continue the 'good work' in the future!

Thanks also to all colleagues from different companies that I met during JIP meetings and conferences. Some of these discussions were very valuable.

I like to thank all my friends for their continuous support. No matter if it was at the tennis court, in art class, in Egyptology class or elsewhere, many were invariably interested in how the research was progressing. Many thanks!

Finally, I like to thank my family, and particularly my father. Thanks dad!

Nomenclature

Roman Symbols

a	Constant in the SN curve
A_L	Lateral wind area
$A_{1/3}$	Significant response amplitude
b	Longitudinal frame spacing
c	Stress-to-load ratio
c_y	Coefficients for lateral force
c_N	Coefficients for moment
D	Wave spreading function, Miner sum
E	Young's modulus
f	Frequency, probability density
F_y	Transverse force
g	Acceleration of gravity
H	Wave height
H_s	Significant wave height
I_{yy}	Longitudinal moment of inertia of the hull-girder
I_{zz}	Transverse moment of inertia of the hull-girder
k	Wave number

K_g	Stress factor that accounts for local geometry
K_w	Stress factor for the weld
L	Effective web spacing
L_{lt}	Long-term accumulated load
L_{pp}	Length between perpendiculars
L_{st}	Short-term accumulated load
m	negative slope of the SN curve
m_n	N-th order spectral moment of response spectrum
M_y	Vertical wave bending moment
M_z	Horizontal wave bending moment
N	Moment, number of cycles
N_a	Number of stress-cycles before failure
O	Occurrence fraction
p	Wave pressure
p_0	Atmospheric pressure
S	Spectral density
s	Wave spreading parameter, stress
T	Vessel draft, wave period
T_R	Repetition time
T_z	Mean zero upcrossing period
V_c	Current speed

Nomenclature

V_w	Wind speed
x	Longitudinal distance, surge motion
y	Transverse distance, sway motion
z	Height of the longitudinal above base, heave motion
z_0	Height of the neutral axis of the hull-girder cross-section above base, distance above the mean waterline
Z	Section modulus of the longitudinal including the effective Plating

Greek Symbols

α	Philips' constant
α_a	Absolute vessel heading
γ	Peakness parameter
Δt	Sample time
ε	Strain
ϕ	Roll motion
μ_r	Relative direction
θ	Pitch motion, wave direction
θ_0	Mean wave direction
ρ_a	Air density
ρ_w	Seawater density

σ	Stress, standard deviation, spectral width parameter
ω	Wave frequency
ω_p	Spectral peak frequency
ζ	Wave elevation
ψ	Yaw motion

Abbreviations

FPSO	Floating production, storage and offloading unit
UKCS	United Kingdom Continental Shelf
IMR	Inspection, maintenance and repair
CAPEX	Capital expenditure
OPEX	Operational expenditure
SCF	Stress concentration factor
VWBM	Vertical wave bending moment
HWBM	Horizontal wave bending moment
COG	Centre of Gravity
CWM	Cubic Weighted Mean
CFD	Computational Fluid Dynamics
VLCC	Very Large Crude Carrier
FMS	Fatigue Monitoring System
MSE	Mean Square Error

1 Introduction

1.1 Problem Overview

Floating production, storage, offloading (FPSO) units are economical and practical development solutions for oil production at (marginal) oil fields. These units are deployed both in benign environments (for example West-Africa), and in harsh environments (for example North-Sea). Figure 1.1 shows as example FPSO “Glas Dowr” on production at the Durward & Dauntless field (North-Sea, UK sector).



Figure 1.1 FPSO Glas Dowr on Durward & Dauntless field (UKCS)

Structural integrity is the ability to withstand the applied loads so that the structure can perform its intended purpose. An adequate structural integrity must be maintained throughout the life of the unit to ensure the safe and reliable operations [1]. If the loads exceed the capacity, the structure is no longer able to fulfil its intended purpose properly.

Structural integrity must be considered from design throughout the operational life [2]. A robust design verified with a conservative design methodology provides a firm basis for adequate structural integrity. During construction, adequate structural integrity needs to be ensured with proper building practices, proper inspection and, where needed, effective repair measures. The structural capacity deteriorates throughout the operational life due to, for example, wear and tear from normal operations, corrosion, fatigue cracking or structural damage caused by overloading. For this reason structural integrity needs to be checked by regular inspections and, when needed, adequate repair measures need to be taken.

The fatigue life of structural details in the hull is an important criterion in the design of a FPSO. Structural details with insufficient fatigue capacity will start to crack over time. An example of a fatigue crack is shown in figure 1.2. Although they are generally not an immediate threat for the safety of the crew and vessel, fatigue cracks may cause leakage and reduce hull strength, and need to be repaired.

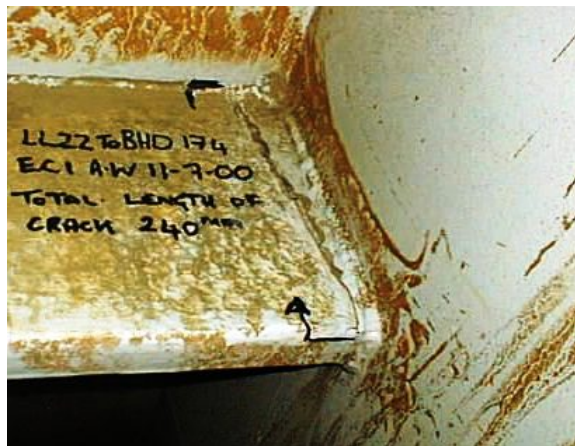


Figure 1.2 Example of fatigue crack in structural detail

Recent experience onboard operating FPSOs shows that cracking in hull details of FPSOs occurs [3]. These fatigue cracks need to be repaired offshore against considerable effort and costs. Improvement in the prediction methods for fatigue loading and fatigue capacity would provide a means to make better fatigue predictions in design.

The current inspection, maintenance and repair (IMR) practices are a time-consuming and costly effort. Given the many structural members in a hull, it would be beneficial if better guidance could be provided for IMR activities.

To define the scope of this research, a brief overview of structural integrity management on vessels and fatigue prediction methodology is given below. Based on this review, the scope in this thesis is outlined.

1.2 Fatigue and Structural Integrity Management

1.2.1 Structural Integrity Systems

Structural management systems are used in different industries, such as in the aeroplane, offshore and shipbuilding industry. Structural integrity management provides a means to ensure adequate structural integrity for the new-built unit and to maintain adequate structural integrity throughout the life of the unit [4,5].

An important aspect of integrity systems is to evaluate the total costs over the life of the unit [4]. Both CAPEX (Capital Expenditure) and OPEX (Operational Expenditure) are important. For a cost-effective solution, a balance between costs and benefits on the long-term is made. Higher construction costs (CAPEX) can be made good with cost savings due to fewer inspections (OPEX) [6].

Apart from prescribing standards for obtaining and maintaining adequate structural integrity structural, these systems ensure that structural data is stored in an easily recoverable format for reviewing purposes [4]. Structural data comprises, amongst other things, as-built drawings, results of inspections, or records of damage and repairs. The review of this data can for instance be used for planning of future inspections, but it can also be used as feedback for future design [7, 8].

Integrity management systems address the design, construction and operations of the unit. All three are discussed below.

1.2.2 Fatigue Design Methodology

Fatigue damage is induced by fluctuating loads, which induce fluctuating stresses in the structural details. These load cycles are induced by the environment in which the unit operates and by vessel operations.

The stress cycles are not large in day-to-day conditions, but the structure is exposed to many load cycles and fatigue damage is accumulated in all sea-states that the vessel encounters. Both the amount and magnitude of the stress cycles are important. Typically most fatigue damage in North-Sea conditions is built up in moderate sea-states, because these sea-states occur often and sufficient stress responses are induced in these sea-states. Severe sea-states give significant stress responses, but because they do not occur often, their contribution to the fatigue damage is relatively small. This will be discussed in chapter 3 (see figure 3.21). This is fundamentally different than assessing the ultimate strength capacity of the structure, where the required structural capacity is determined by one or a few extreme sea-states.

The accumulated fatigue damage in the structure is sensitive to the ranges of the stress cycles. Consider a SN-curve with a constant slope of 3. The fatigue life of the structural member is then inversely proportional to the third power of the stress range. This means that if stress ranges are raised with a factor 2 the fatigue life reduces with a factor 8. This implies that an accurate description of the long-term environment and expected loading conditions must be available for the fatigue assessment. However, the actual loading conditions and environmental conditions can at best be estimated in the design phase. Consequently, considerable uncertainty is associated with the predicted fatigue life.

Many fatigue calculation procedures exist. All main class societies have their own fatigue calculation procedures [9]. All fatigue procedures calculate the fatigue capacity of the structural member and long-term stress distribution that it experiences. From both, the fatigue life of the structural detail is determined.

The fatigue capacity is described by an S-N curve, which gives the number of stress cycles before failure for a given stress range [10]. S-N curves are based on test data. Design codes give applicable S-N curves for structural members or for the calculation method. In the hotspot stress approach, the hotspot stress needs to be calculated by finite element calculations at pre-defined reference points and extrapolated to the fatigue hotspot. The fatigue capacity is described by one SN curve [19]. Following the classification notes of DnV, the stress at the fatigue hotspot consists of a nominal stress times a stress concentration factor [11]. This stress concentration factor depends on the local geometry of the structure and can be evaluated by finite element calculations or from tables in design codes. Local stress raisers due to welding geometry are generally not considered in the calculation of this stress concentration factor and need to be accounted for separately. These values are described in the design codes.

1.2.3 Integrity Management during Construction

Inspections are carried out during the construction of the vessel [12]. During these inspections it is verified that the construction is built according to design specifications. It is important to have an adequate inspection strategy during construction. When defects are detected in an early stage in the construction process they will be relatively easy to repair against relatively low costs. Also an appropriate inspection strategy enables to provide the means to make an as-built history of the vessel.

1.2.4 Integrity Management during Operations

During operations, the structural integrity is maintained by regular inspections and corrective actions on found damage [13]. Inspections in ship structures can be performed on two levels:

- Overall survey,
- Close-up survey.

The purpose of an overall survey is to assess the general status of the structure. This type of survey will produce no detailed results, but identifies problem areas for close-up surveys. In a close-up inspection, detailed inspection data is gathered. Detailed inspections are very time-consuming so only a limited part of the structure can be closely inspected.

Marine structures are periodically inspected because the loads on the structure are uncertain and because limited knowledge exists about the operations and capability of the structure [14]. Inspections are usually the last resort for ensuring safe operations. However, circumstances regarding inspections are far from ideal. Many details need to be inspected in a short period of time. It is impossible to inspect the entire construction and all structural details. Often the details are difficult to reach and the lighting in tanks is bad. Currently used inspection techniques in ship structures are mainly visual inspections. These may be followed up by more advanced Non Destructive Testing (NDT) techniques like Magnetic Particle Inspection (MPI). In [15] an inspector is quoted to put tanker inspections into perspective:

“... picture...a large gymnasium. The compartments...are on that scale. The inspector usually enters this compartment via a ladder from the main deck. He is typically wearing an overall and armed with a flashlight, hopefully an atmosphere monitor, a hammer, pen and instruction book. Often the only available light source is the natural light coming from a few 350 mm diameter tank washing opening in the deck. Usually the tank has not been staged for repairs. Now, given these conditions, consider that the inspector is tasked with being able to find a 25 mm crack on the framing as far away as the back corner of a gymnasium.”

With this in mind it is not difficult to imagine that cracks and other defects are easily missed during inspection. The inspection results do not only vary from inspector to inspector, but also from inspection to inspection with the same inspector [14].

1.3 Background to Research

Until the mid nineties fatigue endurance in ship structures was addressed ‘by experience’ only in the classification rules. The recommended practice and guidance notes for fatigue by DnV were developed because of a growing number of fatigue incidents in local structural details of ship structures, particularly in structural details in which High Tensile Steels (HTS) were used. With the developed code a more direct control on fatigue in ship structures was envisioned [16].

There exist significant differences between FPSO and trading tanker [3]. Tankers typically sail from port to port in fully loaded or in ballast condition. FPSOs continuously produce oil and see all drafts from ballast-load to full-load. These loading conditions include loading conditions with partially filled tanks, which are avoided with regular trading tankers.

FPSOs and trading tankers operate under different environmental conditions [3]. FPSOs are moored at a fixed location throughout their time at the field. Trading tankers sail from port to port through different areas. Tankers are generally designed with generalised wave scatter diagrams applicable for the envisioned trading routes, where site-specific environmental data can be used for the design of FPSOs. Tankers are in port for a significant portion of the time, where FPSOs are continuously exposed to the environment. FPSOs need to endure all weather conditions, where tankers have the ability to avoid adverse whether.

Maintenance and repair requirements are different for FPSOs and trading tankers [3]. Tanker can relatively easily be inspected and repaired in port. FPSOs need to be inspected offshore. Dedicated inspectors and repair crew need to be transferred to the vessel and inspections and maintenance needs to be planned such that their interference with normal production is kept to a minimum. Inspection, maintenance and repairs are considerably more costly offshore than in port.

Given these differences, the fatigue life of tanker and FPSO hulls are different. There has been a struggle with the structural design of FPSOs due to conflicting approaches between the maritime and offshore industries [17]. FPSO hulls are ship-shaped structures, but operated differently than ships. This makes that traditional maritime design rules are not always applicable. The maritime industry typically follows (empirical) rule-based design, where the offshore industry more tends to use first-principle design methods. Classification societies have made significant effort to develop more specific guidance and rules for floating offshore units. Knowledge is still developing in this area [1].

Recent operational experience shows fatigue cracking problems in several operating FPSOs. Because of the redundancy in a ship structure a fatigue crack generally does not pose an immediate threat to safety of the crew and the vessel. However fatigue cracks need to be monitored and ultimately repaired as they may grow and in time lead to failure of the structure. The costs associated with these repairs are generally high.

To investigate the fatigue life of structural members in a FPSO hull, two joint industry projects (JIP) were initiated. The FPSO Integrity JIP [18] addressed the loading side of fatigue and the FPSO Capacity JIP [19] addressed the fatigue capacity of typical structural details in FPSOs.

For the FPSO Integrity JIP, FPSO Glas Dowl was equipped with an extensive monitoring system, measuring amongst other things the wave conditions, motions, strains in deck and side shell longitudinals and wave/cargo pressures [20]. From the measurements the loads that an operating FPSO experiences were investigated and existing computational methods were investigated in selected sea-states [21].

1.4 Scope of Work

The work in this thesis progresses with the results obtained in the integrity I and II JIPs and the FPSO Capacity I & II JIPs and focuses on the loading side of hull fatigue. The fatigue life of a structure is also for a large part determined by the fatigue capacity of structural elements in the hull. Where applicable, use existing fatigue capacity methods are used in this thesis.

The vessel will most likely be operated in different loading conditions and encounter different environmental conditions than anticipated in design. The fatigue life is sensitive to loading conditions and encountered environmental conditions. Therefore, it is of interest to monitor load accumulation over the life of the unit as input for Inspection, Maintenance and Repair (IMR) programs and for conversion work at the yard. Monitoring data could assist in offshore inspections to indicate relevant areas to inspect for fatigue cracks. Furthermore, monitoring data could assist in decision making of preventative repairs for fatigue damage during yard conversions.

The first goal of this research is to develop a practical long-term fatigue life prediction model for deck, side-shell and bottom longitudinals in a FPSO hull. The model will be validated as much as possible against available full-scale measurement data from FPSO ‘Glas Dowr’ and against model-test data.

The second goal in this research is to investigate the application of monitoring systems, capable to log the accumulated loads at selected locations in the hull. Data post-processing techniques and required types and amounts of sensors will be investigated, taking into account the operational convenience of sensors.

The thesis is structured as follows. A long-term fatigue model is developed in chapter 2. Relevant parameters in the model are investigated, and numerical formulations are validated as much as possible against full-scale measurement data and model test data. The application of the fatigue model is investigated in chapter 3. The sensitivities of various parameters in the model are investigated. In chapter 4, the lay-out of a monitoring system for long-term load accumulation monitoring is investigated. Different post-processing algorithms for the system are studied. The performance of these algorithms is studied against full-scale measurement data in chapter 5. Conclusions and recommendations for further research are given in chapter 6.

2 Model Development for Fatigue Life Calculation

In this chapter, a model to calculate the fatigue life of structural members in the deck, side-shell and bottom in a FPSO is investigated. The model is validated as much as possible against available full-scale measured data and model-test data. Most emphasis is put on the calculation of the long-term load distributions.

Fatigue capacity calculation procedures are reviewed from literature in section 2.1.

Important aspects in the calculation of long-term load distributions are the environment in which the unit operates and vessel loading conditions [3]. A representative description of the day-to-day environment needs to be available for a reliable fatigue calculation. Relevant aspects about environmental description and loading condition profile are described in section 2.2 and section 2.3 respectively.

The orientation of the vessel in wind waves and swell determines the load responses and needs to be taken into account [22]. In section 2.4, a procedure is discussed and validated to determine the vessel heading of a turret-moored FPSO in a non-collinear environment.

Wave pressure, global hull bending moments and cargo pressures need to be taken into account in a hull fatigue calculation [11]. Models for these loads are discussed in the sections 2.5, 2.6 and 2.7 respectively.

The combination of these loads to short-term and long-term stress distributions is discussed in section 2.8. Furthermore, the calculation of the fatigue damage and fatigue life is discussed in this section.

2.1 Fatigue Capacity

Prior to the fatigue life calculation, relevant fatigue hotspots in the hull must be identified. Likely candidates for fatigue problems comprise members with large stress-concentration factors in highly loaded areas.

The fatigue capacity determination of a structural member comprises the selection of an applicable SN curve, and the calculation of hotspot stresses for a given load. Both aspects are discussed below.

2.1.1 SN-Curve Data

Applicable SN curves for different types of structural members can be found in design codes, such as [10] or [11]. An SN curve can be expressed as:

$$\log N_a = \log a - m \log \Delta\sigma \quad (2.1)$$

in which a is a constant in the SN curve, m is the negative slope of the SN curve and N_a is the number of stress-cycles with magnitude $\Delta\sigma$ before fatigue failure.

Design codes provide values for a and m . A SN curve can have different values for a and m depending on the number of cycles. See for instance the DnV SN curve for welded material in air or with cathodic protection [11]. Below $N_a \leq 10^7$ cycles, the SN-curve has parameters $m=3$ and $\log a = 12.65$ and for $N_a > 10^7$ cycles, $m=5$ and $\log a=16.42$.

The SN curves can also be specified for different conditions. This is shown in figure 2.1 where SN curves are given for structural members in air or with cathodic protection, and for structural members in corrosive environments. DnV also specifies an alternative SN curve with a constant slope. The use of this alternative SN curve leads to results on the safe side for calculated fatigue lives exceeding 20 years [11].

Equation (2.1) shows that the fatigue life depends heavily on the slope, m , of the SN curve. Consider an SN curve with a constant slope of 3. Then the allowable number of cycles and the fatigue life is inversely proportional to the third power of the stress range. When a stress range increases with a factor 2 the fatigue life decreases with a factor 8. Relatively small differences in stress ranges result in relatively large differences in the fatigue life. Given this large sensitivity of fatigue life, considerable uncertainty must be expected in the fatigue life evaluation.

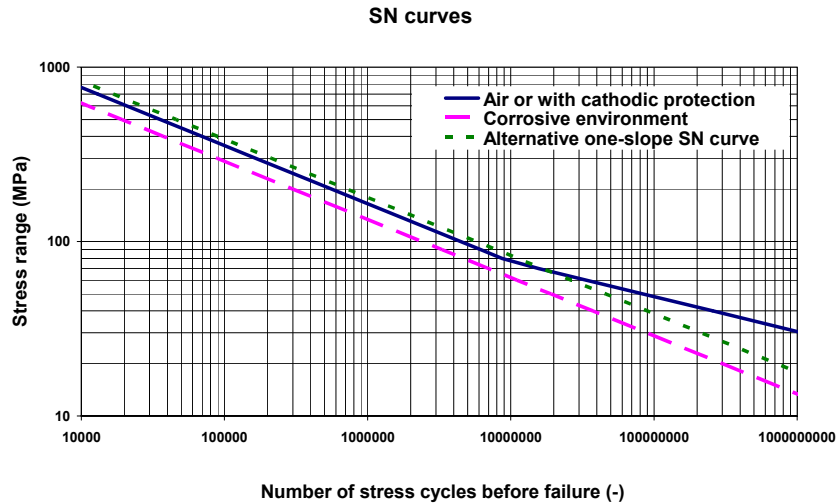


Figure 2.1 DnV SN curves for hull fatigue [11]

2.1.2 Stress at the Fatigue Hotspot

The nominal stress is the stress at the hotspot without the influence of the local geometry and weld included. The nominal stress is the calculated from the applicable load at the structural detail. However, the nominal stress is not the relevant stress for the fatigue assessment; local geometry effects and welding effects need to be included as well.

The relation between the nominal stress and the stress at the fatigue hotspot can be described as [11]:

$$\sigma = \sigma_n K_g K_w \quad (2.2)$$

in which σ is the stress at the fatigue hotspot, σ_n is the nominal stress, K_g is the stress factor that accounts for local geometry and K_w is the stress factor for the weld.

The nominal stress and stress factors for local geometry and weld stress factor are discussed separately below.

2.1.3 Nominal Stress

Nominal stresses induced by wave pressure and by the vertical wave bending moment (VWBM) and the horizontal wave bending moment (HWBM) are relevant for the fatigue assessment of hull members.

To derive a formulation for the nominal stress induced by wave pressure, consider a clamped longitudinal between two web frames under a uniformly distributed wave pressure p . The stress-to-load ratio for pressure load, c_p , between pressure loading, p , and nominal stress, $\sigma_{n,p}$, can be expressed as:

$$c_p = \frac{\sigma_{n,p}}{p} = \frac{bL^2}{12Z} \quad (2.3)$$

in which b is the longitudinal spacing, L is the effective web spacing and Z is the section modulus of the longitudinal including the effective plating.

A relation between the VWBM and stress, c_{my} , and the HWBM and the nominal stress, c_{mz} , can be calculated as:

$$c_{my} = \frac{\sigma_{n,my}}{M_y} = \frac{(z - z_0)}{I_{yy}} \quad (2.4)$$

$$c_{mz} = \frac{\sigma_{n,mz}}{M_z} = \frac{y}{I_{zz}}$$

in which M_y is the VWBM, M_z is the HWBM, z is the height of the longitudinal above base, z_0 is the height of the neutral axis of the hull-girder cross-section above base, I_{yy} is the longitudinal moment of inertia of the hull-girder, y is the horizontal distance of the longitudinal to the centreline, and I_{zz} is the transverse moment of inertia of the hull-girder.

These relations can be refined when considering additional stresses due to local deformations and secondary bending (stresses due to the bending of the entire cargo tank section or frame). The nominal stress can also be determined by finite element calculations [11]. These calculations are also capable to assess secondary bending effects and stress effects due to deformation of the structure.

2.1.4 Stress Factors for Local Geometry and Welding

The stress concentration factor (SCF) for welding, K_w is generally specified in design codes, such as [11]. The SCF for local geometry, K_g , needs to be determined per structural member.

The local SCFs depend on the applied load (bending or axial loading) and the local geometry. Classification notes, such as [11], specify SCFs for local geometry for different structural members under axial loading or a bending moment.

They can also be calculated with finite element analysis. Lotsberg et al. [23] describe the hotspot stress approach, applied on typical FPSO structural details. In this approach, the stress is calculated at two reference points before the hotspot by finite element analysis. Typically, these reference points are located at $\frac{1}{2}t$ and $\frac{3}{2}t$ before the hotspot, but different codes, such as IIW [24], specify different locations (0.4t and 1.0t). The stresses at these reference points are linearly extrapolated to the hotspot. One master SN-curve links the fatigue life to the hotspot stress. The SCF for local geometry is determined from this hotspot stress as the ratio between the hotspot stress and the nominal stress.

The calculated hotspot stresses are sensitive to many parameters, such as the density of the mesh, element types, local geometry (complexity of local stress field) and the location of extrapolation points. A different approach is described by Dong et al [25]. The local stress raisers in the structure are calculated with finite element analysis, and fatigue life is linked to the hotspot stress with one master SN-curve. The method determines the local stress concentration from integration of nodal loads in a section. According to Dong, the numerical results are relatively mesh-insensitive.

Fatigue design is also a matter of common sense. Structural elements with large stress concentration factors at highly loaded locations are likely candidates for fatigue cracking. The fatigue life is very sensitive to the hotspot stresses. This is unfortunate for the accuracy of the fatigue calculation, but this feature also implies that the fatigue life in structural joints can be improved significantly with relatively simple measures, because a little reduction of the hotspot stresses causes a significant increase in fatigue life. A practical improvement may for instance be the application of a bracket, or changing the shape of a bracket. This measure reduces the hotspot stress by reducing the effective length of the longitudinal and decreases the local stress concentration factor.

2.2 Environmental Description

Vital for a proper fatigue assessment is the availability of accurate environmental data. In comparison with a sailing tanker, the environmental conditions in which a FPSO operates, are well defined [3]. A FPSO is permanently moored at the same location, where weather conditions can be registered. In contrast, ships sail through different areas and the encountered wave conditions are much less well defined.

2.2.1 Environmental Data Sources

For the FPSO designer, wave data are generally supplied by a metocean consultant or they are specified in design requirements. It is of interest to have a basic knowledge about the available sources of environmental data.

Knowledge of wave conditions is based on many observations [26]. Various data-sources are:

- Visual observations (for instance from ships),
- Instrumented observations from wave buoys or platforms,
- Satellite data,
- Hindcast data.

Visual observations of wave height, period and direction have been reported from ships in normal service all over the world under the auspices of the World Meteorological Organization (WMO) [27]. The data has been archived by a number of meteorological agencies in different countries. Since the observations are made in accordance with guidance notes prescribed by the WMO, they represent data, which are globally homogeneous in quality. They also cover most sea areas of practical interest, with concentration of density on the main shipping routes. A considerable number of atlases containing data derived from these observations have been published.

Environmental information can also be registered with dedicated instruments, for example wave sensors on a platform or wave buoys. In [27] a comparison is made between visually observed wave data with instrumented wave data at different locations around the world. The wave height data from observations matches well with instrumented data. The quality of the mean zero upcrossing wave period (T_z) data of instrumented data may vary because T_z is sensitive to noise and the method of processing. The comparison shows a large difference between visually observed and measured wave periods.

The most common methods of measuring waves are with wave rider buoys or arrays of wave gauges [28]. Two types of wave rider buoys exist [29]: the heave-roll-pitch buoy and a wave rider buoy with accelerometers. Wave height data and directionality data can be measured through measuring the heave and wave steepness in north and east direction. From these three time-traces and their cross-correlation, a 1-D wave spectrum and a wave spreading function can be calculated. However, wave measurements at a single location, such as measured by wave rider buoys, are not capable to capture the full 3-D character of the wave spectrum [30], because not enough information is measured to quantify the wave spreading. The form of a wave spreading function is postulated and coefficients of this function are determined from the cross-correlation spectra of the measured time-traces [30, 31]. A commonly used wave spreading function is the \cos^{2n} wave spreading function, but in [31] also the sech spreading function is used. Lygre and Crogstad [61] use the maximum entropy method to estimate the shape of the 3-D wave spectrum.

Wave information can also be recorded with weather satellites using a Synthetic Aperture Radar (SAR) [32]. This instrument makes radar images of the sea-surface. These images typically cover 15 x 15 km. The wave properties are derived from these pictures using image processing techniques. The large advantage of satellite measurements is that the measurements cover an area rather than a point [32]. This gives more insight in the origin of the waves.

Wave data can also be obtained through hindcasting [33]. All hindcast models calculate wave spectra per time step from measured wind fields. The sea is modelled with a numerical grid. The energy balance equation, which describes the change of energy of a frequency and directional component, is solved per grid-point [33]. Wave energy transportation through advection, wave energy dissipation through white-capping (breaking waves), bottom friction in shallow water, non-linear transfer of wave energy by wave-wave interactions, wave refraction in shallow water can be taken into account in hindcast models. Wave conditions are divided in a wind wave and a swell component.

The quality of the hindcast output depends on the number of available weather stations in the area where wind data is recorded [34]. In areas like the North Sea many weather stations are available and the quality of the hindcast data is good. In the Southern Hemisphere the density of weather stations is much lower, and consequently, the quality of the hindcast data is lower.

The quality of the hindcast model can be improved by feeding measured wave data, for instance satellite data or wave buoy data [35].

2.2.2 Modeling of Wave Conditions

Figure 2.2 shows an example of a measured wave spectrum at the Sable field in South-Africa. This wave spectrum was measured with a wave rider buoy, which is deployed in the surroundings of the Glas Dowr. The 3-D wave spectrum was calculated from ½-hour of measured buoy data with the maximum entropy method as described by Lygre and Crogstad [61]. The figure shows that two wave systems are present in this sea-state. Furthermore, considerable wave spreading exists in this wave spectrum.

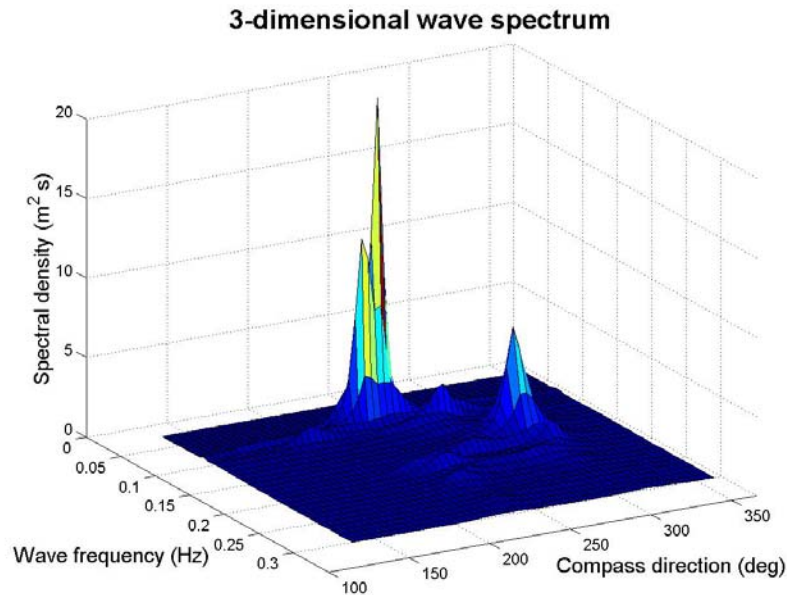


Figure 2.2 Wave spectrum measured at Sable field (South-Africa)

Typically about the Sable field is that the site is exposed to swell originating from both the Atlantic Ocean and the Indian Ocean, next to local wind waves. This makes that significant swell conditions occur at this field. As will be shown in chapter 3, the bulk of the load accumulation in deck and side-shell longitudinals is induced by swell at this field. This is different than at a North-Sea field where the bulk of the load accumulation is induced by wind waves, as will be shown in chapter 5.

The shapes of measured wave conditions at the North-Sea Durward & Dauntless field were analysed in [3]. It was found that the wave spectrum is seldom described well by theoretical spectrum formulations. Often, sea-states with multiple wave systems were encountered. When comparing responses calculated with the measured wave spectrum and the fitted JONSWAP spectrum, it was found that long-term response statistics are similar [3].

In the calculation procedure, the sea-state is characterised by a wind wave system and a swell system. Each wave system is described with a JONSWAP wave spectrum formulation [36]:

$$S(\omega) = \alpha g^2 \omega^{-5} \exp\left[-\frac{5}{4}\left(\frac{\omega}{\omega_p}\right)^{-4}\right] \gamma \exp\left[-0.5\left(\frac{\omega - \omega_p}{\sigma \omega_p}\right)^2\right] \quad (2.5)$$

in which α is the Philips's constant, g is the acceleration of gravity (9.81 m/s^2), ω is the wave frequency, ω_p is the spectral peak frequency, γ is the peakness parameter, and σ is the spectral width parameter.

Information on wave spreading within sea-states is not generally available during design of the vessel. If modelled, an assumption regarding the shape of wave spreading function needs to be made. Forestall and Ewans [75] review existing wave spreading functions. A commonly used wave spreading function is the \cos^{2s} spreading function, $D(\omega, \theta)$ [37]:

$$D(\omega, \theta) = C \cos^{2s}(\theta - \theta_0) \quad (2.6)$$

in which s is the wave spreading parameter, θ is the wave direction and θ_0 is the mean wave direction. C is a constant for which holds that:

$$\int_{-\pi}^{\pi} C \cos^{2s}(\theta - \theta_0) = 1 \quad (2.7)$$

This wave spreading formulation will be used in the long-term fatigue model. The sensitivity of load accumulation to wave spreading is investigated in chapter 3.

2.3 Loading Conditions

FPSOs are operated differently than trading tankers [3]. Tankers typically sail in fully-loaded conditions in the full lag and in ballast condition in the empty lag. Slack tanks are avoided. Due to the continuous production of FPSOs, cargo tanks are partially filled in a significant portion of the time. The loading condition changes constantly over time.

Figure 2.3 shows a typical example of the midship draft during a number of loading cycles (logged at FPSO ‘Glas Dowl’ at the Sable field in South-Africa). The figure shows that all drafts from ballast load to full-load condition are encountered. Figure 2.4 shows the probability density distribution of the draft at FPSO Glas Dowl in approximately one year. The figure shows that not all loading conditions occur equally often.

The characteristics of a loading cycle depend on the vessel characteristics (storage capacity, etc.) and on the field characteristics (flow rates etc.). The loading condition of the vessel has a significant impact on the motions and loads on the FPSO hull. A representative set of loading conditions must be accounted for in the fatigue calculation. Furthermore, the occurrence of the separate loading conditions needs to be taken into account.

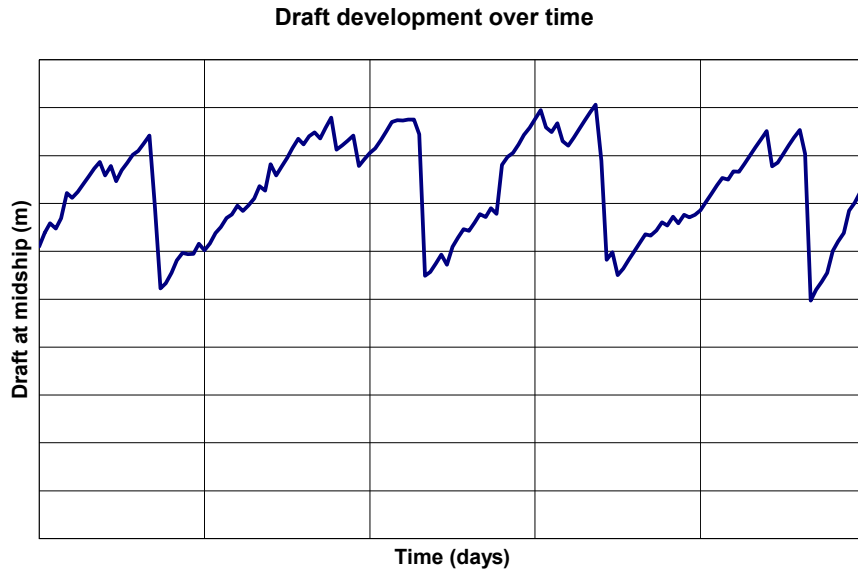


Figure 2.3 Typical draft development of a FPSO

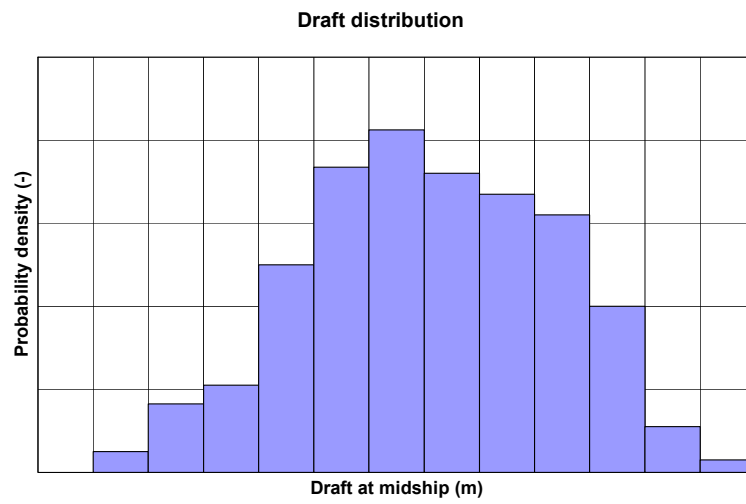


Figure 2.4 Typical draft distribution of a FPSO

2.4 Orientation of Vessel in a Sea-State

2.4.1 Literature

The vessel heading relative to the environment has an important influence on the vessel responses [22], [38], and needs to be taken into account in the fatigue calculation [39].

A spread-moored FPSO has a fixed heading, which is determined by the orientation of the mooring system. A turret-moored FPSO is free to weathervane around its turret. The average vessel orientation in a sea-state is determined by the location of the turret and the environmental forces that are imposed on the hull. These environmental forces are wind, wave and current forces. The heading may actively be controlled with thrusters or supporting tugs.

Calculation procedures to determine the average vessel heading of turret-moored vessels without thrusters or tug assistance in non-collinear environments have been developed. De Souza Jr. and Morishita [40] describe a model that calculates the motions of a turret-moored FPSO. The model is validated against model tests. The average vessel heading was predicted well without dynamics taken into account.

Vestbostad et al. [41] describe a procedure to calculate the mean vessel heading relative to wave and swell and the roll motions of the vessel. They show a comparison between model tests and calculations and the agreement was found to be reasonably good.

In the developed procedure in this thesis, a static model is used to calculate the average vessel heading in non-collinear environments. The advantage of a static model is that a large number of sea-states can be evaluated fast. The model and the performance of the model used in this thesis were described earlier in [42]. The model comprises a FPSO that is free to weathervane around its turret.

2.4.2 Adapted Calculation Procedure

The following calculation procedure is adapted. Wind, waves, current and swell induce yaw moments and transverse and longitudinal loads. The adapted coordinate system is shown in figure 2.5.

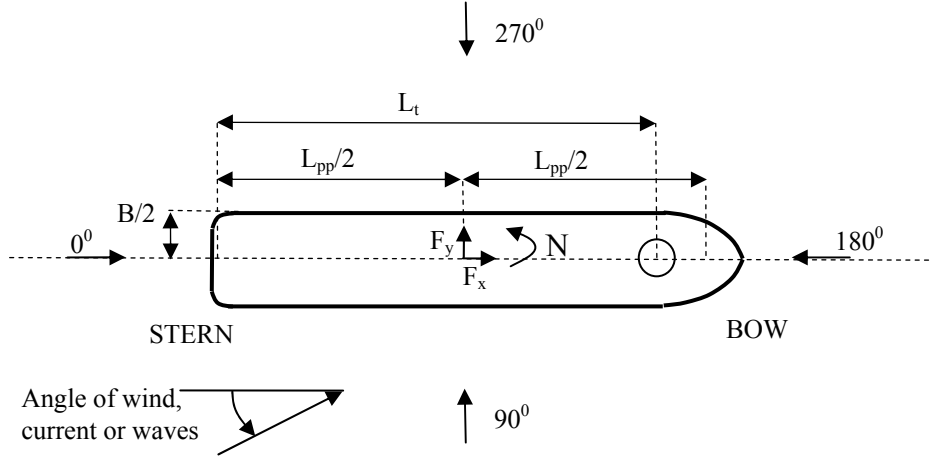


Figure 2.5 Coordinate system

The wind force in lateral direction and wind moment are calculated as function of the absolute vessel heading with the expressions given by OCIMF [43]:

$$\begin{aligned}
 F_{yw}(\alpha_a) &= \frac{1}{2} \rho_a A_L c_{wy} (\mu_{wr}) V_w^2 \\
 N_w(\alpha_a) &= \frac{1}{2} \rho_a A_L L_{pp} c_{wN} (\mu_{wr}) V_w^2
 \end{aligned}
 \tag{2.8}$$

in which F_{yw} and N_w are the lateral wind force and the wind moment, ρ_a is the air density, A_L is the lateral wind area, c_{wy} and c_{wN} are the wind coefficients for lateral wind force and wind moment, μ_{wr} is the relative wind direction, α_a is the absolute vessel heading, and V_w is the wind speed. Values for c_{wy} and c_{wN} as function of the wind direction are given by OCIMF [43]. These wind coefficients are determined from wind-tunnel tests. Alternatively, wind coefficients can be determined with dedicated model-tests.

Similarly, the current forces in transverse direction and the current moment are calculated as function of the absolute vessel heading as [43]:

$$\begin{aligned} F_{yc}(\alpha_a) &= \frac{1}{2} \rho_w L_{pp} T c_{cy}(\mu_{cr}) V_c^2 \\ N_c(\alpha_a) &= \frac{1}{2} \rho_w L_{pp}^2 T c_{cN}(\mu_{cr}) V_c^2 \end{aligned} \quad (2.9)$$

in which F_{yc} and N_c are the lateral current force and the current moment, ρ_w is the seawater density, L_{pp} is the length between perpendiculars, T is the vessel draft, c_{cy} and c_{cN} are the current coefficients for lateral current force and current moment, μ_{cr} is the relative current direction, and V_c is the current speed.

OCIMF [43] describes current coefficients as function of the current direction for a Very Large Crude Carrier (VLCC). These current coefficients were determined with model tests. Alternatively, current coefficients can be determined with dedicated model-tests.

Lateral wave drift forces, $c_{dy}(\mu, T_z)$, and wave drift moments, $c_{dN}(\mu, T_z)$, are calculated with linear diffraction theory in sea-states with unit significant wave height. The drift forces and moments in sea-states with significant wave height H_s are calculated as:

$$\begin{aligned} F_{yww}(\alpha_a) &= c_{dy}(\mu_{wwr}, T_z) \frac{H_s^2}{16} & F_{ys}(\alpha_a) &= c_{dy}(\mu_{sr}, T_z) \frac{H_s^2}{16} \\ N_{ww}(\alpha_a) &= c_{dN}(\mu_{wwr}, T_z) \frac{H_s^2}{16} & N_s(\alpha_a) &= c_{dN}(\mu_{sr}, T_z) \frac{H_s^2}{16} \end{aligned} \quad (2.10)$$

in which F_{yww} and N_{ww} are the drift forces from wind waves, F_{ys} and N_s are the drift forces from swell, H_s is the significant wave height, T_z is the mean zero upcrossing wave period, μ_{wwr} and μ_{sr} are the relative wind wave and swell direction and c_{dy} and c_{dN} are the lateral drift force coefficients, and the drift force coefficient for yaw rotation.

This procedure is performed separately for wind waves and swell, because both have a different wave spectrum. Furthermore, the wind wave and swell direction is generally different.

So far, the wind, wave current and swell forces and moments are calculated at their points of application. When adapting the OCIMF coordinate system, this point is midship for wind and current (see figure 2.3). For wind waves and for swell this point is generally the centre of gravity (COG) of the vessel. The yaw moments around the turret induced by wind, current, wind waves and swell are calculated as:

$$\begin{aligned}
 N_{wt}(\alpha_a) &= N_w - F_{yw}(L_t - x_{wr}) \\
 N_{ct}(\alpha_a) &= N_c - F_{yc}(L_t - x_{cr}) \\
 N_{wwt}(\alpha_a) &= N_{ww} - F_{yww}(L_t - x_{sr}) \\
 N_{st}(\alpha_a) &= N_s - F_{ys}(L_t - x_{sr})
 \end{aligned} \tag{2.11}$$

in which N_{wt} , N_{ct} , N_{wwt} and N_{st} are the moments of wind, current, wind waves and swell around the turret, L_t is the location of the turret before App, and x_{wr} , x_{cr} and x_{sr} are the location of the reference points for wind, current and waves relative to APP, as defined above.

The total yaw moment around the turret, N_{Tt} , as function of the vessel heading is calculated as the sum of the yaw moments around the turret:

$$N_{Tt}(\alpha_a) = N_{wt}(\alpha_a) + N_{ct}(\alpha_a) + N_{wwt}(\alpha_a) + N_{st}(\alpha_a) \tag{2.12}$$

The yaw moments are calculated as function of the compass heading. The mean stable vessel heading is found for the direction that satisfies the following two conditions:

$$M(\alpha_a) = 0 \tag{2.13}$$

and:

$$dM(\alpha_a)/d\alpha_a > 0 \tag{2.14}$$

The mean stable vessel heading is calculated with the first condition (equation 2.13) and the second condition (equation 2.14) ensures that the found heading is stable.

2.4.3 Full-Scale Validation

This procedure was validated against more than 3 months of measured vessel-heading data on FPSO 'Bleo Holm' (Ross field, UKCS). This validation work was previously described in [42].

The purpose of the measurement campaign onboard Bleo Holm was to record and study the roll motions of the vessel [42]. A dedicated roll motion sensor was installed on the vessel. To provide additional information to interpret the data, additional data was stored. This data consisted of time & date, vessel draft data, wind data, and vessel heading data and was recorded with onboard computers for operational purposes (helicopter operations, etc.). Additionally, hindcasted wave, wind and current data were available.

The average vessel headings in 1-hour sea-states were calculated with the described model. As input for the calculation wind tunnel tested wind and current coefficients were used, and the hindcasted environmental data was used. The calculated vessel headings were compared with measured headings. The average vessel headings were determined from the recorded vessel heading time-traces.

The comparison between the measured and calculated vessel headings is shown in figure 2.6. Furthermore, the relative contributions of the wind, waves, current and swell are shown in figure 2.6. Wind waves and wind have the largest influence on the long-term vessel heading distribution. In 67% of the cases, the vessel heading is predicted within 15% of the measured vessel heading. In 84% of the cases, the vessel heading is predicted within 30 degrees of the measured vessel heading. This is also shown in figure 2.7.

The error in heading prediction as function of the significant wave height is shown in figure 2.8. Generally, the largest differences occur in sea-states with significant wave heights smaller than 3 m.

Possible reasons for the differences between measured and predicted headings were investigated in [42]. Comparison between measured and hindcasted wind data shows that particularly in lower sea-states significant differences occur between hindcasted and measured wind direction. Furthermore, logged wind data shows changing wind conditions in some events with low wind speeds. This suggests that a part of the differences may be explained by the accuracy of the environmental data.

The impact of errors in vessel heading predictions in mild sea-states will be discussed in chapter 5.

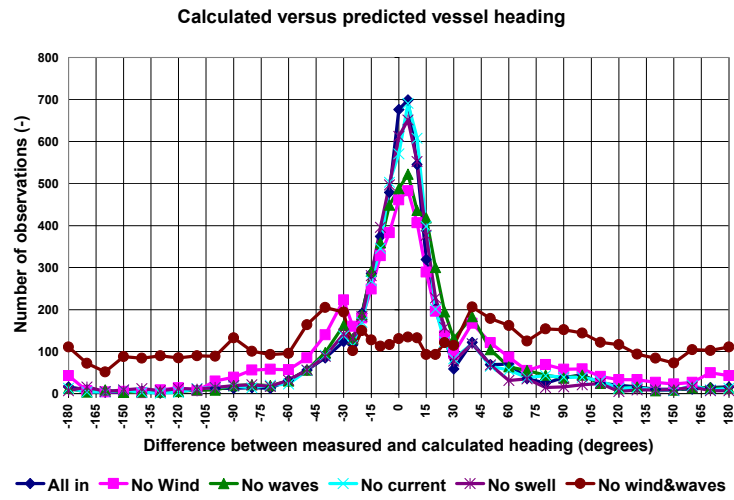


Figure 2.6 Measured vs. calculated vessel headings

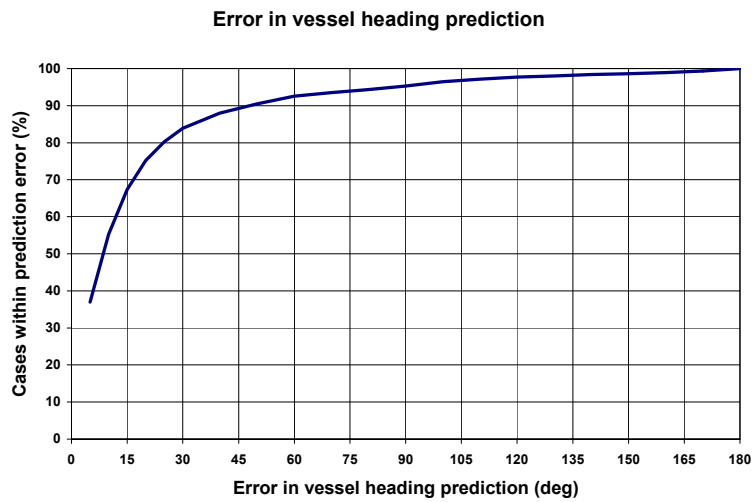


Figure 2.7 Error in vessel heading prediction

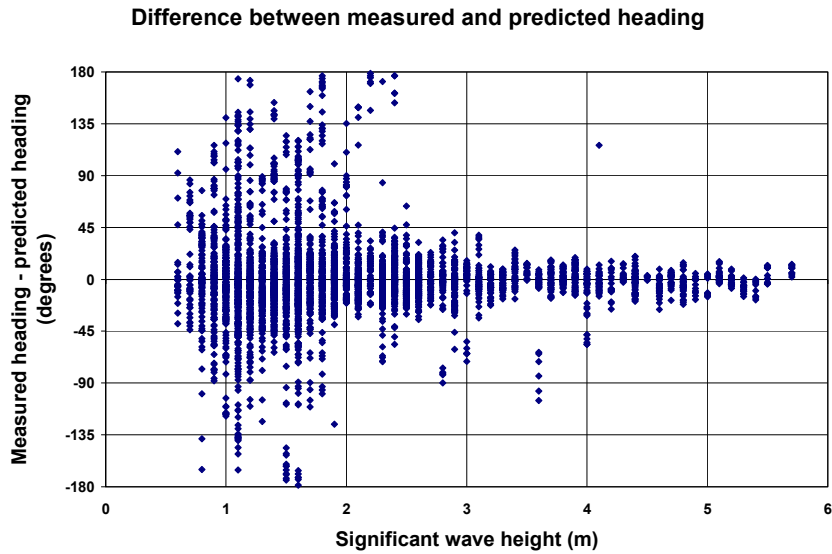


Figure 2.8 Error in vessel heading prediction plotted against wave height

2.5 Wave Pressure Loading

2.5.1 Literature

Wave pressures have an important contribution to the load accumulation in side-shell longitudinals that are exposed to wave action. The amount of load accumulation induced by wave pressure depends on the local draft, vessel motions and wave conditions.

Wave pressure models are described in many publications. Hsao and Chen [44] describe a comparison between linear strip theory calculations with model tests and full-scale measurement data on a Great Lake bulk carrier and a SL-5 container vessel. The calculations compared reasonably well with both the model tests and the full-scale tests. At midship the results were better than at the foreship, which was contributed to the fact that the performance of strip theory deteriorates towards the ends of the vessel, where 3D flow effects are encountered.

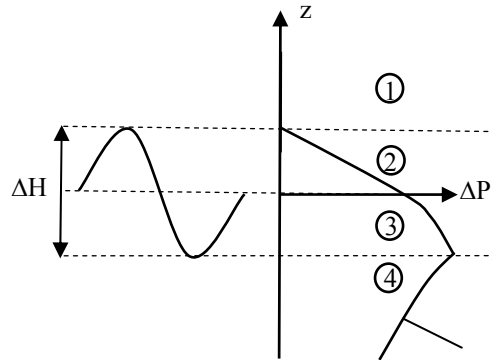


Figure 2.9 Wave pressure function over the height

The side-shell near the mean waterline is intermittently submerged and emerged. This is shown in figure 2.9. Four areas with different wave pressure loading can be distinguished. The side-shell in area 1 is not submerged in wave crests and does not receive wave pressures. Locations in area 2 become submerged in wave crests. In area 3, the side-shell emerged in wave troughs. At locations deeper than the wave amplitude below the MWL, the side-shell doesn't emerge.

Cramer et al [46] propose a method to take into account the effect of intermittent wetting. The method calculates pressure range in a wave with a given height and period. The pressure ranges in the four areas of interest are calculated as:

$$\Delta P(z) \approx \begin{cases} 0 & \Delta H / 2 \leq z < \infty \\ \rho g (\Delta H / 2 - z) & 0 \leq z < \Delta H / 2 \\ \rho g e^{kz} (\Delta H / 2 - z) & -\Delta H / 2 \leq z < 0 \\ \rho g e^{kz} \Delta H & -\infty < z < -\Delta H / 2 \end{cases} \quad (2.15)$$

in which ΔP is the wave pressure range, ρ is the water density, g is the acceleration of gravity, ΔH is the wave pressure, is the height above the MWL, and k is the wave number.

An example of the wave pressure range as function of the height z with this model is shown in figure 2.9. In the model, the wave pressures above the mean waterline are modelled as hydrostatic pressures. This is supported by a publication by Bing et al [47] who discuss model test results of water pressures at a plate above the mean waterline. Their results show that the pressure deteriorates linearly in the wave crests.

Friis Hansen et al [45] propose a pressure model in time-domain, which takes into account the intermittent wetting effect. They discuss that the pressure is composed of the following four components: (1) the undisturbed wave train, (2) effects of change in hydrostatic pressure due to vessel oscillations in calm water, (3) pressure due to diffraction on the side-shell of the unmoving vessel, and (4) pressure from radiated waves generated by ship occupancies in calm water. The first two components are considered dominant and the third and fourth component are neglected. Based on the time-trace of the instantaneous wave pressures are calculated. Pressures above the mean waterline are calculated as hydrostatic pressures and pressures at locations below the mean waterline are calculated and cut-off at atmospheric pressure when the location becomes submerged and don't receive wave pressure. Time-trace examples will be shown in the next section.

Følso [48] describes a model in frequency domain, which takes into account global loads and local wave pressures. The wave pressures are calculated through wave pressure RAOs, instead of through the relative wave elevation. Intermittent wetting is taken into account. Comparison is made with the time-domain model by Friis Hansen et al [45] and good correlation is found. Følso concludes that load combination is important and needs to be considered in side-shell fatigue. Furthermore, he concluded that stress responses in the side-shell may be broadbanded, which has an effect on the fatigue life.

2.5.2 Numerical Modeling

Wave pressures at the mean waterline are not harmonic due to the intermittent wetting effect. Pressure loads around the mean waterline give an important contribution to the long-term distribution at these longitudinals. Furthermore, it is important that the phase relations between the global (wave-bending) loads and local (pressure) loads are taken into account.

A time-domain formulation for the calculation of wave pressures is adapted in this thesis. The advantage of a time-domain model is that both the wave pressure model and the phase relations between the global and local loads can be correctly accounted for. Furthermore, no assumption needs to be made regarding the load cycle distribution, and the broadbandedness of the loads can be taken fully into account.

A similar formulation as described by Cramer et al [46] is adapted in this thesis. The wave pressure, $p(t)$, is calculated from the relative wave elevation time-trace, $\zeta(t)$, as:

$$p(t) = \begin{cases} \rho g(\zeta(t) - Z) & Z > 0 \\ -\rho gZ + \rho g\zeta(t) \frac{\cosh k(h+Z)}{\cosh(kh)} \cos(kx - \omega t) & Z \leq 0 \end{cases} \quad (2.16)$$

in which t is the time, ρ is the seawater density, g is the acceleration of gravity (9.81 m/s^2), z is the distance of location above the MWL (positive upwards), k is the wave number and h is the waterdepth relative to MWL.

The relative wave elevation is a result of vessel motions and incoming waves. Motions and waves have a different effect on the wave pressure on the hull. The motions and wave part are not separated in this formulation, considering that the vessel motions in day-to-day sea-states are small.

2.5.3 Modeltest Validation of Pressure Model

Modeltests were performed to validate the described pressure model. The modeltests and validation were performed for the FPSO Capacity II JIP and are described by Van der Cammen, Kaminski and Francois [50]. A physical model (scale 1:42.84), which closely resembled FPSO ‘Glas Dowr’, was used in the tests. The main dimensions of the Glas Dowr and of the tested model are shown in table 2.1. Modeltests were performed for a draft of 11.3 m, a loading condition commonly encountered at Glas Dowr.

Quantity FPSO	Glas Dowr	Model Unit
Length (Lpp) (m)	232	232
Breadth (m)	42.00	40.48
Depth (m)	21.20	21.76
Draught (m)	14.90	16.02
Displacement (t)	121,620.0	125,486.5
Block coefficient (-)	0.8172	0.8137

Table 2.1 Main properties of Glas Dowr and tested model

Wave pressures, relative wave elevations at various locations along the vessel, vessel motions and wave conditions were recorded. Figure 2.10 shows the location of the pressure sensors and relative wave elevation near midship. The figure also shows the location of the measured wave pressures at Glas Dowr.

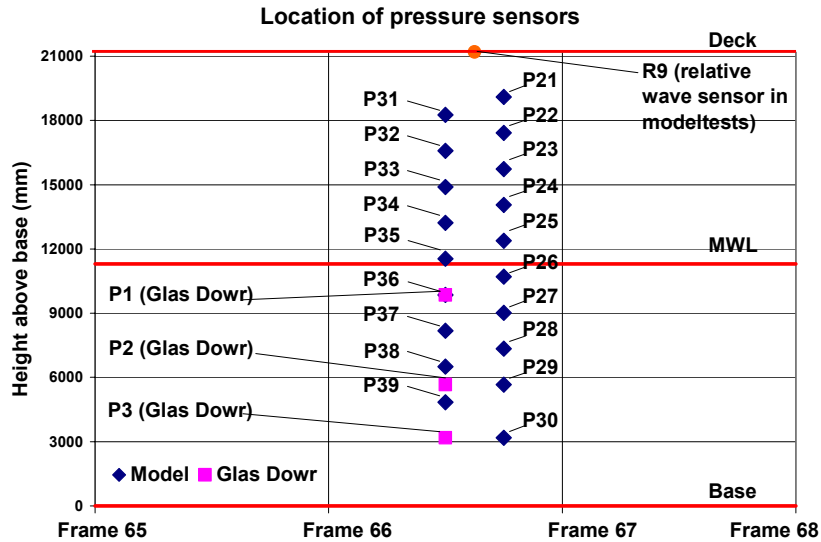


Figure 2.10 Location of measurement sensors

Regular wave tests and irregular tests in long-crested and short-crested waves were performed in the modeltest program. Tests were performed in realistic day-to-day conditions, as observed during the measurement campaign at Glas Dowl at the Durward & Dauntless field (UKCS). Also, a limited number of tests in extreme conditions and high beam-sea conditions were performed.

Wave pressure time-series were calculated with the pressure model. The vessel draft at the wave pressure points and the measured relative wave elevations were used as input for the calculations. The pressure cycle distributions of the measured and calculated pressure time-series were determined with the ASTM rainflow counting procedure [50]. Per test, this comparison was made at all 19 pressure measurement locations. To be able to compare the measured and calculated distributions, the Cubic Weighted Mean value (CWM) of the pressure distributions was determined as:

$$P_{CWM} = \left(\frac{\sum \Delta P^3}{N} \right)^{1/3} \quad (2.17)$$

in which P_{CWM} is the cubic weighted mean pressure, ΔP is the counted pressure range, and N is the total number of counted cycles.

The CWM value is the load range that would lead to the same fatigue damage as the entire load spectrum in case the slope of the SN curve has a constant value of 3. The accumulated loading, L_p , in the time-series is calculated as:

$$L_p = P_{CWM}^3 N \quad (2.18)$$

in which N is the number of counted pressure cycles.

The accumulated loading is proportional to the accumulated fatigue damage acquired in the sea-state given that the slope in the SN curve is 3. The accumulated loading is used, since it makes it possible to quantify the rainflow counted pressure distributions with a single number.

Figure 2.11a shows the measured and calculated accumulated pressure load over the height of the side-shell in a typical day-to-day sea-state and figure 2.11b shows the comparison in a sea-state with large vessel motions. The data in the graphs is normalized to the highest accumulated wave pressure in the measurements.

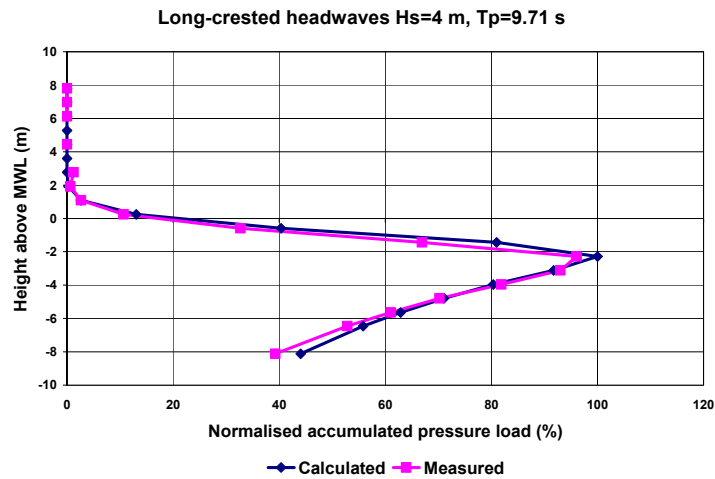


Figure 2.11a Measured and calculated wave pressure accumulation in day-to-day sea-state

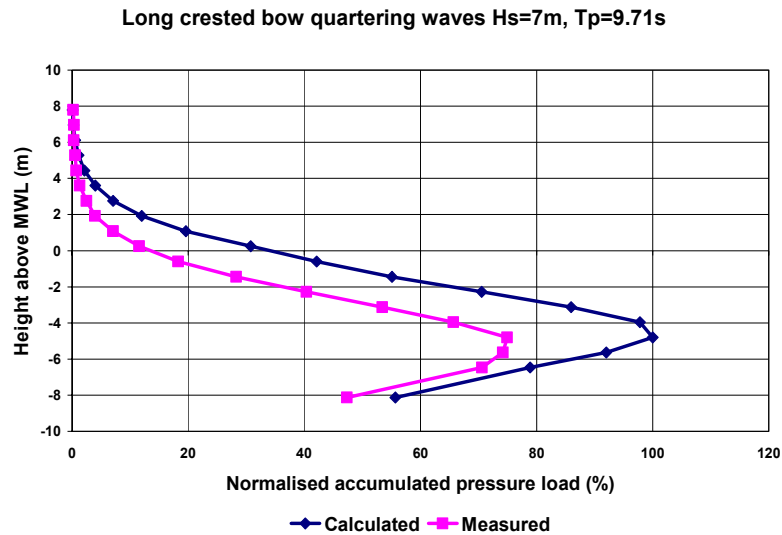


Figure 2.11b Measured and calculated wave pressure accumulation in sea-state with heavy vessel motions

Figure 2.9 showed four areas with different wave pressure loading. The side-shell in area 1 is not submerged in wave crests and does not receive wave pressures. Locations in area 2 become submerged in wave crests. In area 3, the side-shell emerged in wave troughs. At locations deeper than the wave amplitude below the MWL, the side-shell doesn't emerge.

The side-shell in area 3 receives most accumulated wave pressure loading. This can be explained as follows. The wave pressure amplitude in a wave crest is highest at the MWL. These locations emerge in wave troughs and don't receive wave pressure in wave troughs. This limits the magnitude of the wave pressure range. This is shown in figure 2.12.

Moving downward through area 3, the wave pressure amplitude in a wave crest deteriorates, but the wave pressure amplitude in a wave trough increases. In area 4, the structure does not emerge in wave troughs and receives the full wave pressure range. Moving further down, the wave pressure range decreases.

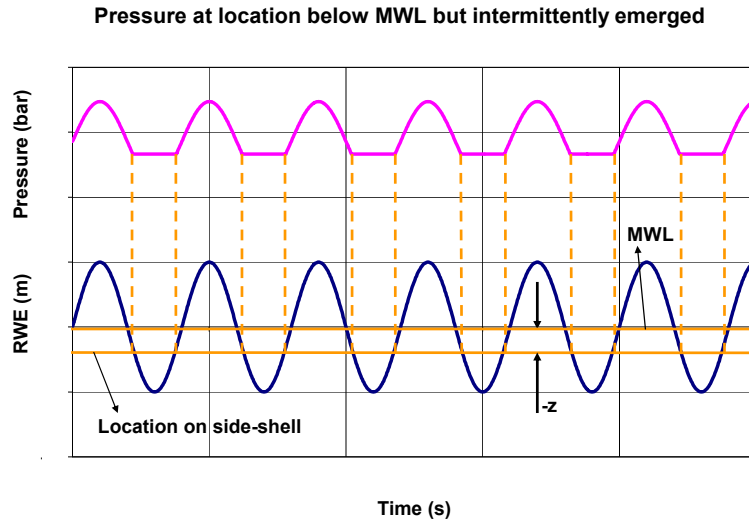


Figure 2.12 Pressure time-trace with intermittent wetting

A good resemblance between measurements and calculations is found in the modeltests for day-to-day conditions. In sea-states with significant vessel motions, the match between modeltests and calculations is not good. Since the events with large vessel motions don't occur often, their contribution in the long-term load accumulation is limited. This will be discussed further in chapter 3.

2.5.4 Full-Scale Model Validation

The wave pressure model was also validated against full-scale measured data at FPSO "Glas Dowl" at the Durward & Dauntless field, UKCS. This validation was also performed for the FPSO Capacity II JIP and previously described in [51].

The locations of the three wave pressure sensors used for the validation work are shown in figure 2.13. These sensors are located at Port Side (PS) of the vessel near midship. In the study, 767 recorded wave pressure registrations of ½-hour duration each were used. This comprises a period of almost 16 days. Loading conditions ranging from ballast condition to full-loaded condition and a variety of wave conditions, ranging from significant wave heights of 0.2 m until 7.3 m significant were encountered in this period.

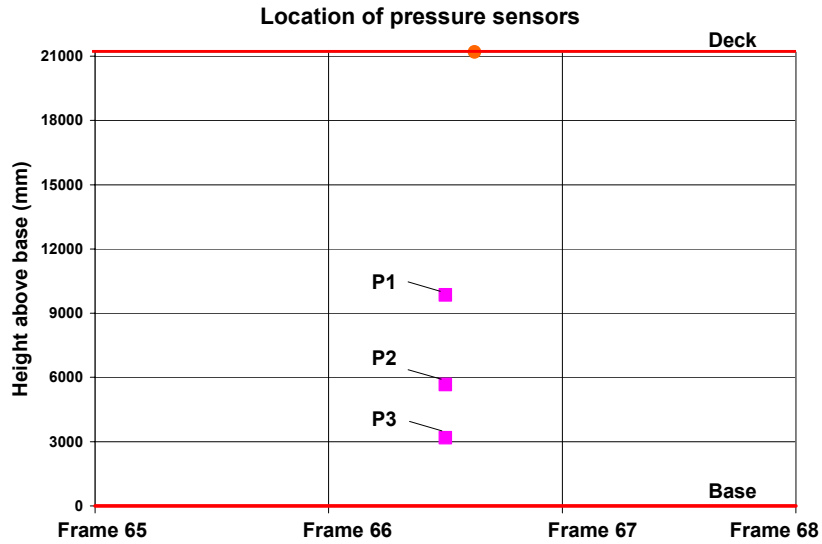


Figure 2.13 Locations of wave pressure sensors at Glas Dowr (PS)

The relative wave elevations measurements were not used in the analysis, since review of time-series indicated unreliable sensor registrations, probably caused by reflections caused by droplets on the sensor. Instead, the relative wave elevation time-series were determined from the measurements at the middle wave pressure sensor (P2). Per sea-state, the location of the mean waterline, z_{mwl} , was estimated from the average wave pressure \bar{p} as:

$$z_{mwl} = z_{sensor} + \frac{\bar{p} - p_0}{\rho g} \quad (2.19)$$

in which p_0 is the atmospheric pressure, ρ is the density of the seawater, and g is the acceleration of gravity.

The relative wave pressure time-series is calculated with equation (2.16). Wave pressure sensor P2 was submerged in all sea-states. With the relative wave elevation time-trace, the wave pressure time-traces at upper pressure sensor (P1) and the lower pressure sensor (P3) are calculated.

The pressure cycle distributions are determined by rainflow counting. As was discussed in section 2.5.3, it is convenient to characterise these stress distributions by a single quantity, being the short-term accumulated pressure load. Short-term accumulated pressure loads are calculated from the pressure cycle distribution with the equations (2.17) and (2.18). They are proportional to the third power of the pressure range. The accumulated load is proportional to the Miner sum in case of a SN curve with a constant slope of 3.

The long-term accumulated pressure loading, $L_{p,lt}$, is calculated as the sum of the short-term accumulated loads in all sea-states:

$$L_{p,lt} = \sum L_p \quad (2.20)$$

A shows a short piece of a measured and calculated wave pressure time-series at P3 (lower sensor) in one sea-state is shown in figure 2.14a. A short piece of a measured and calculated wave pressure time-trace at P1 (P1 below mean waterline, but emerges in wave troughs) is shown in figure 2.14b. The physics in time-domain are represented well by the model, although differences between measurements and calculations are observed.

Figure 2.15 shows the long-term accumulated load at P1 and P3, normalised in percentages (measurements =100%). The calculations over-predict the measurements by 40%. Possible reasons for these differences can be found in the model or in the input (location of MWL and relative wave elevation) for the calculations. Wave pressure is sensitive to the location of the waterline. In a given sea-state, the mean waterline location can be estimated within certain accuracy from the measured wave pressure. When calculating the location of the MWL from the middle or lower pressure sensor, a fair degree of spreading is observed. Accumulated loading due to wave pressure is very sensitive to the location of the MWL.

Load accumulation is proportional to the third power of the load (see equation 2.18). This makes that relatively small differences between measurements and calculations are blown up to relatively large differences in the long-term accumulated loads. See for instance the sixth pressure range of P3 in figure 2.14a (between 20 and 25 seconds). The pressure range in the calculated time-trace comprises approximately 0.32 bar, and the pressure range in the measured time-trace is approximately 0.30 bar. The pressure range from the calculations is approximately 7% higher than the measured range. This corresponds to an accumulated load that is approximately 20% higher from the calculated pressure range than from the measured pressure range. Consequently, a very accurate model and very accurate input data for the model would be needed to keep the load accumulation accurate within a few percents.

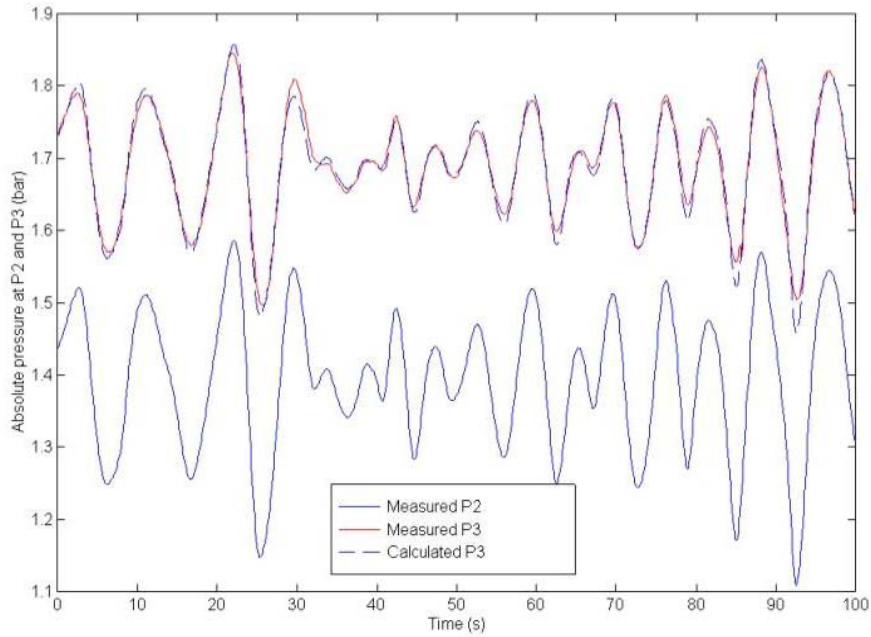


Figure 2.14a Measured and calculated wave pressure time-series

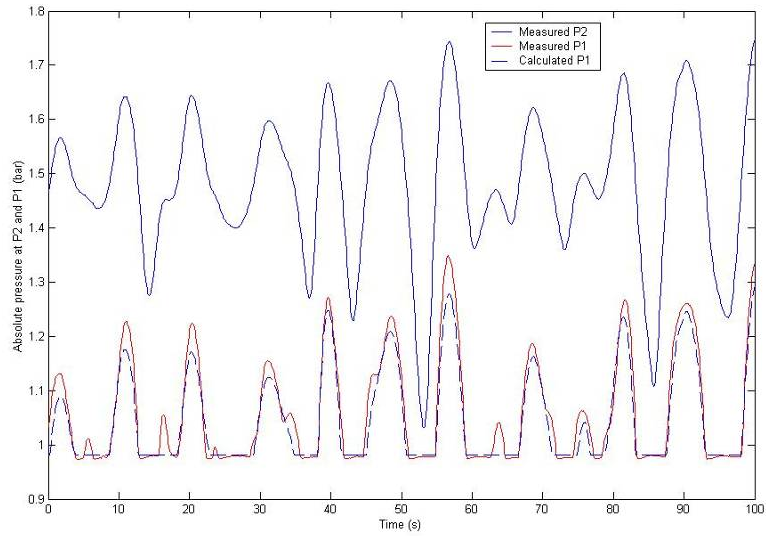


Figure 2.14b Measured and calculated wave pressure time-series

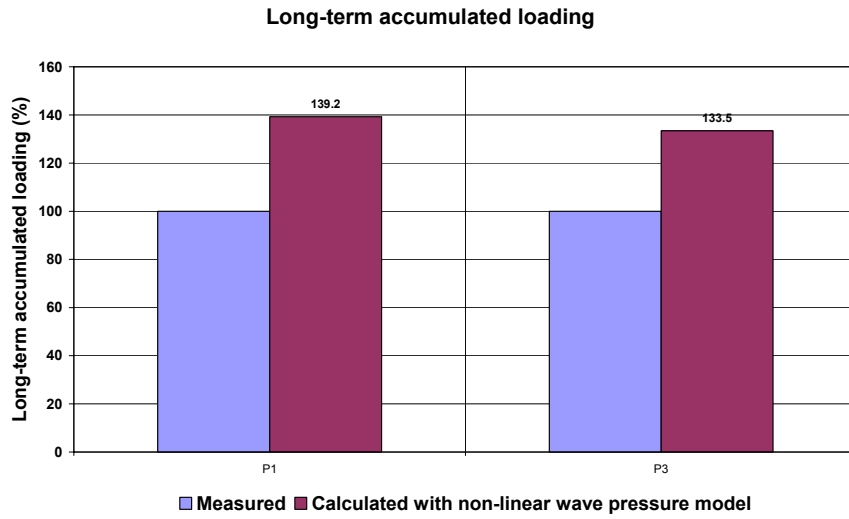


Figure 2.15 Long-term accumulated wave pressure loading from non-linear model

2.6 Calculation of Global Loads

The bending moment in the midship section is an important strength criterion for the design of a vessel [52]. The total bending moment consists of a still-water bending moment, induced by the mass distribution and displacement distribution of the vessel, and a wave bending moment. The wave bending moment is composed of the Vertical Wave Bending Moment (VWBM) and the Horizontal Wave Bending Moment (HWBM).

Wave bending moments are non-linear in extreme wave conditions. These non-linearities are induced by the shape of the vessel; an important source of these non-linearities results from the fact that the side-shells are not vertical [53]. Slamming is of importance in extreme wave conditions [54] and also a non-linear function of wave height.

Non-linearities can result in different hogging and sagging moments. In linear theories, hogging and sagging moments are the same.

For tanker hull-shapes, a large part of the bending moment is due to the still water bending moment [55]. Furthermore, the bulk of the fatigue damage of an operating FPSO is induced in mild to moderate sea-states. As a result, wave-induced non-linearities are small and linear theory is used for the calculation of wave bending moments.

In this thesis, transfer functions of VWBM and the HWBM are calculated with strip-theory and/or diffraction theory.

2.7 Cargo Pressures

Dynamic pressures in cargo and ballast tanks are induced by motions of the vessel. Their magnitude depends on the filling level of the tank, tank location, location in the tank, tank dimensions and the motions of the vessel.

Malenica et al [118] use a linear 3-D potential method to calculate tank pressures due to vessel motions. They recognise that the real sloshing phenomenon in a tank is not correctly modelled, but they rather address the most important part of sloshing dynamics which influences the global behaviour of the ship. The detailed analysis of tank sloshing can not be solved with a linear (and probably even non-linear) potential theory. For this, more sophisticated models such Computational Fluid Dynamics (CFD) methods need to be used.

Violent sloshing in tanks can occur in case of large vessel motions. However, for the problem of fatigue, generally mild to moderate sea-states are important, rather than storm conditions. The motions of the vessel are generally small in these conditions, which makes that violent sloshing needs not be taken into account. As a result, a relatively simple model to calculate tank pressures can be used.

The tank pressures are induced by the acceleration of the cargo and static angle. They are modelled as:

$$p_i(t) = \begin{cases} 0 & z_i > z_s \\ \rho \begin{pmatrix} x_s - x_i \\ y_s - y_i \\ z_s - z_i \end{pmatrix}^T \cdot \left\{ g \begin{pmatrix} -\theta(t) \\ \phi(t) \\ 0 \end{pmatrix} + \begin{pmatrix} \ddot{x}_c(t) \\ \ddot{y}_c(t) \\ \ddot{z}_c(t) \end{pmatrix} \right\} & z_i \leq z_s \end{cases} \quad (2.21)$$

in which $\ddot{x}, \ddot{y}, \ddot{z}$ are the accelerations in longitudinal, transverse and vertical direction in the tank centre, θ is the pitch motion, ϕ is the roll motion, (x_i, y_i, z_i) are the location co-ordinates in the tank and, (x_s, y_s, z_s) are the co-ordinates of the centre of the surface. In a square tank these co-ordinates are given as:

$$\begin{aligned} x_s &= x_c \\ y_s &= y_c \\ z_s &= 2z_c \end{aligned} \quad (2.22)$$

Many web frames are present in the ballast tanks. For that reason the tank pressure due to the accelerations in x-direction is neglected and equation (2.21) reduces to:

$$p_i(t) = \rho(y_s - y_i) \{g\phi(t) + \ddot{y}_c(t)\} + \rho(z_s - z_i) \ddot{z}_c(t) \quad (2.23)$$

The presented formulation to calculate dynamic cargo pressures was proposed and investigated in the FPSO Integrity JIP and tested against full-scale measurement data for a limited number of sea-states [56]. In this thesis work, the model was validated in 489 sea-states with a duration of ½ hour. The ballast pressures were measured at the Glas Dowl working at the Durward & Dauntless field (UKCS). The significant wave height during the measurements ranged from 1-5 meters. Various tank filling levels were encountered during the measurements.

The tank pressures in the ballast tanks were calculated at the pressure sensors P4, P5 and P6 in ballast tank no# 3 PS, which is located near midship. The locations of the sensors in the tank are shown in figure 2.16.

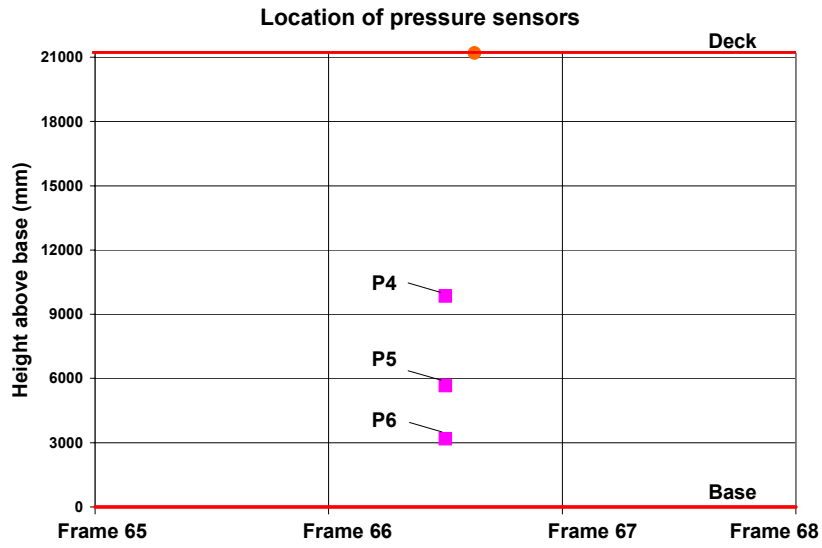


Figure 2.16 Location of ballast pressure sensors

The tank level was derived from the measured tank pressures as:

$$z_c = z_p + \frac{\bar{p} - p_0}{\rho g} \quad (2.24)$$

in which \bar{p} is the mean pressure measured at the lowest pressure sensor, p_0 is the atmospheric pressure (taken as 1 bar), ρ is the seawater density (1025 kg/m^3) and z_p is the vertical distance of the lower pressure sensor to the bottom of the tank (3.177 m).

Time-traces of ballast pressure were calculated with equation (2.22). Recorded vessel motions and the tank level calculated in (2.23) were used as input for this calculation. The pressure cycle distributions of measured and calculated ballast pressure time-traces were determined by rainflow counting.

As was discussed in section 2.5.3, it is convenient to characterise these stress distributions by a single quantity, being the short-term accumulated pressure load. Short-term accumulated pressure loads are calculated from the pressure cycle distribution with the equations (2.17) and (2.18). They are proportional to the third power of the pressure range. The accumulated load is proportional to the Miner sum in case of a SN curve with a constant slope of 3.

The long-term accumulated ballast pressure, $L_{b,lt}$, is calculated as the sum of the short-term accumulated loads in all sea-states:

$$L_{b,lt} = \sum L_b \quad (2.25)$$

in which L_b is the short-term accumulated ballast pressure.

Figure 2.17a shows a short piece of a measured and calculated ballast pressure time-series, at P4, P5 and P6. Figure 2.17b shows the long-term accumulated pressure load from measurements and calculations.

A good agreement between measured and calculated ballast pressure time-traces is observed. Furthermore, a good agreement between long-term accumulated pressure loads is observed.

Pressure ranges in the order of 0.05 bar are observed in the presented time-traces. These pressure ranges are relatively small in comparison with wave pressure ranges. To compare, the wave pressure ranges in figure 2.14a are in the order of 0.3-0.4 bar.

Since equation (2.22) is linear, the ballast pressure for a given tank, location in the tank, and tank level can be expressed as a linear transfer function:

$$p_i(\omega) = \rho(y_s - y_i) \{g\varphi(\omega) + \ddot{y}_c(\omega)\} + \rho(z_s - z_i) \ddot{z}_c(\omega) \quad (2.26)$$

in which ω is the wave frequency.

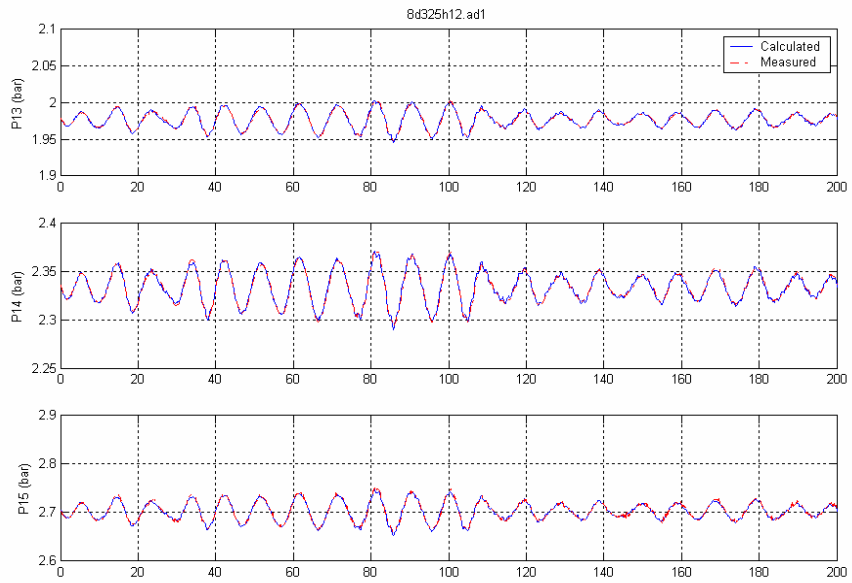


Figure 2.17a Comparison between measured and calculated ballast pressures

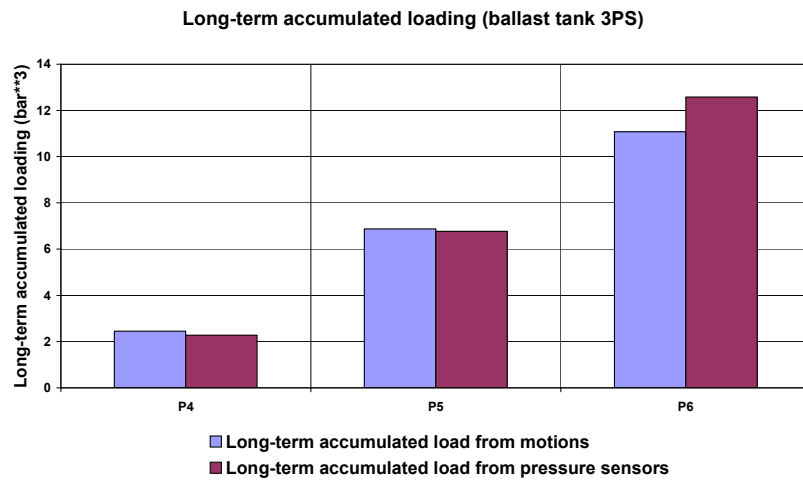


Figure 2.17b Comparison between measured and calculated ballast pressures

2.8 Long-term Stress Distribution

2.8.1 Calculation of Relative Wave Elevations

As was discussed in section 2.5, the wave pressure is calculated from the relative wave elevation. Relative wave elevations can be calculated directly with 3D diffraction theory or they can be calculated from the vessel motions. In 3D diffraction theory, wave diffraction and radiation are taken into account.

Figure 2.18 shows an example of the relative wave elevation transfer function, calculated for Glas Dowlr with a linear 3D diffraction program [59]. The figure shows unexplained numerically unstable behaviour in higher wave frequencies. Sea-states with mean zero upcrossing wave periods of 4 seconds have energy in wave frequencies above 1.5 rad/s. This is shown in figure 2.19, where a JONSWAP wave spectrum with a significant wave height of 4 m is shown and a peakness factor of 3.3. The dotted line shows the wave spectrum with a mean zero upcrossing period of 10 seconds and the continuous line is the wave spectrum with a mean zero upcrossing period of 5 seconds.

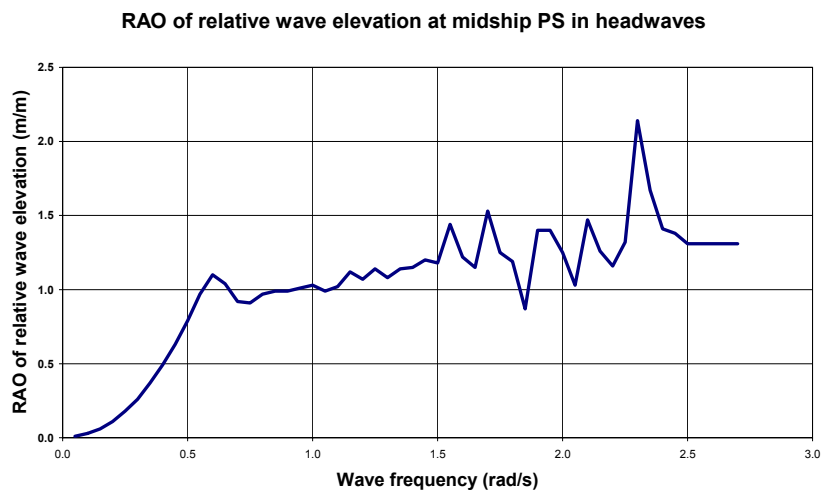


Figure 2.18 Relative wave elevation transfer function of Glas Dowlr in full-load and head-waves

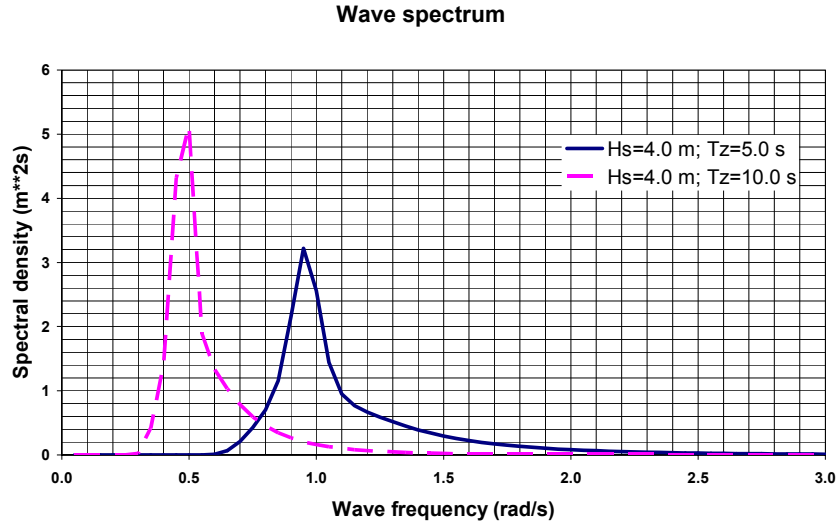


Figure 2.19 Wave spectrum for different wave periods

Sea-states with mean zero upcrossing wave periods of 5 seconds are regularly encountered sea-states. Therefore, in this thesis, the relative wave elevations have been calculated from vessel motions, and using a different method to include wave diffraction and radiation effects.

The relative wave elevation, s , at a specific point along the side of the vessel can be calculated as [49]:

$$s = \zeta_F - z + x\theta - y\phi \quad (2.27)$$

in which z is the heave motion, x is the distance of the vessel centre of gravity (COG) (positive forward), θ is the pitch motion, y is the transverse distance from the vessel COG (positive to PS), ϕ is the roll motion and ζ_a is the incident wave.

The incident wave is defined as:

$$\zeta_F = \zeta_a \cos(kx + \omega t) \quad (2.28)$$

in which ζ_a is the incident wave amplitude, ω is the wave frequency, and k is the wave number calculated with the dispersion relation:

$$k = \frac{\omega^2}{g} \quad (2.29)$$

This formulation comprises the undisturbed wave train and does not take into account radiation and diffraction effects.

This formulation of relative wave elevations does not take into account wave diffraction and radiation. An empirical correction to account for wave diffraction and radiation is applied on the relative wave elevation RAOs:

$$s_D = C_{dif} s \quad (2.30)$$

in which s_D is the relative wave elevation RAO corrected for diffraction and radiation effects and C_{dif} is the correction factor. C_{dif} is based on the comparison of RAOs with and without diffraction effects. The correction parameter depends on the wave direction. For Glas Dowl, an amplification of 1.2 is used in headwaves. For the wind wave side within a sector of 60 degrees off beam-seas, a factor of 2.0 is used, and for the lee-side of the vessel within a sector of 60 degrees off beamseas, a factor of 0.4 is used. In the other wave sectors, this factor is linearly interpolated. The development of C_{dif} as function of the wave direction is shown in figure 2.20.

The correction factor C_{dif} also depends on the wave frequency. The effect of wave diffraction and radiation will be small in long waves, where in short waves, much wave diffraction and radiation will occur. The correction factor is linearly built up between a lower wave frequency and a higher wave frequency. Above this higher wave frequency, the full correction factor is applied. In this study, 0.5 rad/s and 1.0 rad/s are used. Below the lower wave frequency, a correction factor of 1 is applied. This is shown in figure 2.21.

The long-term effect of wave diffraction and radiation will be investigated in chapter 3.

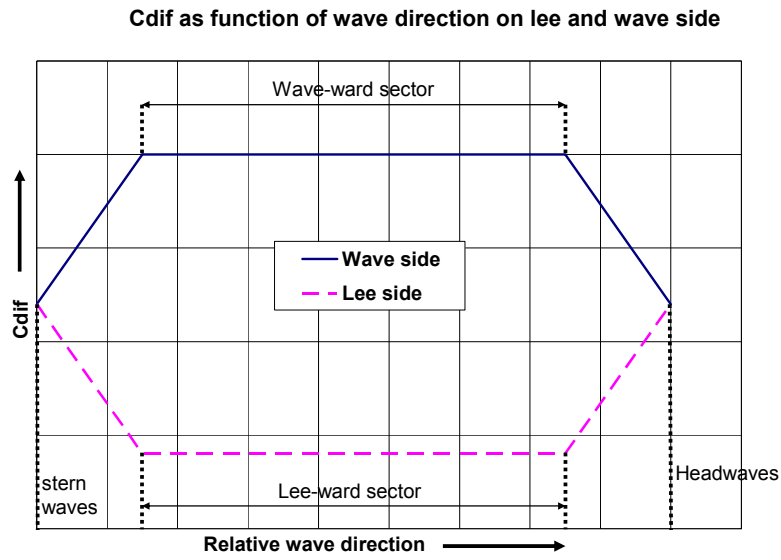


Figure 2.20 C_{dif} as function of wave direction

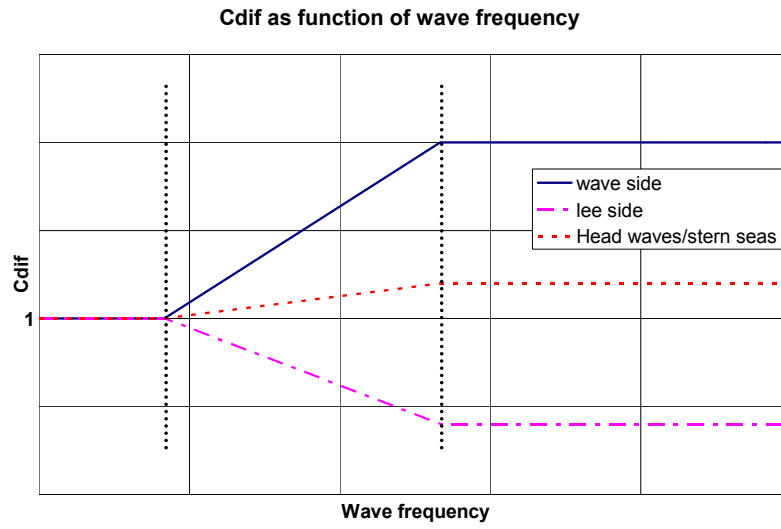


Figure 2.21 C_{dif} as function of wave frequency

2.8.2 Calculation of Stress Responses

It is important to maintain the correct phase relations between the loads. Due to the intermittent wetting effect, the wave pressure can not be easily taken into account in a spectral method. A practical method of maintaining the phase relations between the loads and taking the wave pressure correctly into account is by combining the loads in time-domain.

The spectrum of a response is calculated as [57]:

$$S_r(\omega) = |RAO(\omega, \theta)|^2 S_\xi(\omega) \quad (2.31)$$

in which S_r is the response spectrum as function of the wave frequency ω , RAO is the transfer function, and S_ξ is the wave spectrum.

The response time-trace, $X(t)$, is calculated as [58]:

$$X(t) = \sum_{n=1}^N \sqrt{2S_r(\omega_n)\Delta\omega} \cos(\omega_n t + \varepsilon_n) \quad (2.32)$$

in which t is time (in seconds) and ε_n is the phase angle and N is the number of wave frequencies. The phase angle ε_n is composed of the phase angles calculated with diffraction theory or strip theory and a set of random phase angles:

$$\varepsilon_n = \varepsilon_R(\omega_n) + \varepsilon_{r,n} \quad (2.33)$$

in which $\varepsilon_{r,n}$ is a random phase angle drawn from a uniform distribution between 0 and 360 degrees, and $\varepsilon_R(\omega_n)$ is the phase angles calculated with strip theory or diffraction theory. This separation is necessary to maintain the correct phase relations between the different loading components in time-domain.

The time after which the time-series repeats is:

$$T_R = 2N\Delta t \quad (2.34)$$

in which Δt is the sampling time and T_R is the repetition time of the time-trace.

The sampling time is related to the sampling frequency, f , as:

$$f = \frac{1}{\Delta t} \quad (2.35)$$

To avoid anti-aliasing the sampling frequency needs to be higher than the Nyquist frequency, which is given as:

$$f_n = 2f_{\max} = \frac{\omega_{\max}}{\pi} \quad (2.36)$$

in which ω_{\max} is the highest wave frequency in the response spectrum.

Because relative wave elevations have transfer functions, which do not end at zero in high wave frequencies, relatively high wave frequencies need to be taken into account in the calculations. Calculations are made for wave frequencies until 3.0 rad/s (period of 0.5 s). This gives a Nyquist frequency of 6 rad/s and consequently the sampling frequency in the time-trace needs to be smaller than 1.05 seconds. A fixed sampling frequency of 1 Hz is used.

Time-traces of the relative wave elevation, vertical wave bending moment (VWBM), horizontal wave bending moment (HWBM) and ballast pressure are calculated:

$$\begin{aligned} \zeta_R(t) &= \sum_{n=1}^N \sqrt{2S_{\zeta_R}(\omega_n)\Delta\omega} \cos(\omega_n t + \varepsilon_{\zeta_R}(\omega_n) + \varepsilon_{r,n}) \\ p_{b,i}(t) &= \sum_{n=1}^N \sqrt{2S_{p_{b,i}}(\omega_n)\Delta\omega} \cos(\omega_n t + \varepsilon_{b,i}(\omega_n) + \varepsilon_{r,n}) \\ M_y(t) &= \sum_{n=1}^N \sqrt{2S_{m_y}(\omega_n)\Delta\omega} \cos(\omega_n t + \varepsilon_{m_y}(\omega_n) + \varepsilon_{r,n}) \\ M_z(t) &= \sum_{n=1}^N \sqrt{2S_{m_z}(\omega_n)\Delta\omega} \cos(\omega_n t + \varepsilon_{m_z}(\omega_n) + \varepsilon_{r,n}) \end{aligned} \quad (2.37)$$

The wave pressure time-trace is calculated from the relative wave elevation time-trace with the pressure model described in section 2.5:

$$p(t) = \begin{cases} \rho g (\zeta_R(t) - Z) & Z > 0 \\ -\rho g Z + \rho g \zeta_R(t) \frac{\cosh k(h+Z)}{\cosh(kh)} \cos(kx - \omega t) & Z \leq 0 \end{cases} \quad (2.38)$$

The relation between loads and stresses was discussed in section 2.1. Relations between pressure loads and stresses at the hotspot and relations between global loads and hotspot stresses were discussed. It was discussed that apart from the nominal stress, stress raisers due to local geometry (K_g) and stress factors due to the weld (K_w) need to be included.

These loads are combined to the stress in the hotspot in the structural member as:

$$\begin{aligned} \sigma(t) = c_p K_{g,t} K_w (p_w(t) - p_b(t)) + \\ + K_{g,g} K_w (C_{my} M_y(t) + C_{mz} M_z(t)) \end{aligned} \quad (2.39)$$

Per sea-state, the stress time-trace is calculated for wind waves and for swell separately. The stress time-traces induced by wind waves and swell are assumed statistically independent and a different random phase angle realisation is used for their calculation. The stress time-trace in combined seas is calculated as:

$$\sigma_{t,t}(t) = \sigma_{t,w}(t) + \sigma_{t,s}(t) \quad (2.40)$$

The stress ranges in the stress time-traces in combined seas are counted with the rainflow counting procedure as specified by ASTM [50]. This count results in a short-term stress distribution $N(d\sigma)$; the number of counted cycles is specified per stress range class.

The number of cycles before fatigue failure for a given stress range is given as:

$$\log N_a = \log a - m \log \Delta \sigma \quad (2.41)$$

The fatigue damage, D , is calculated with Miner's rule as:

$$D = \sum \frac{N}{N_a} \quad (2.42)$$

As discussed earlier, it is convenient to quantify the (stress) distributions by a single quantity. This quantity is the accumulated load. To determine this accumulated load, the Cubic Weighted Mean (CWM) stress, A , of the time-trace is calculated:

$$A = \left(\frac{\sum \Delta\sigma_i^3}{N} \right)^{1/3} \quad (2.43)$$

in which $\Delta\sigma_i$ is the i -th counted stress range, and N is the total number of counted ranges.

The short-term accumulated loading, L , is calculated as:

$$L = CWM^3 N \quad (2.44)$$

The short-term accumulated loading is proportional to the fatigue damage (Miner sum) in case of a single-sloped SN curve with slope 3.

2.8.3 Long-Term Stress Distribution

To acquire the long-term stress cycle distribution, a number of representative loading conditions and environments need to be evaluated. Stress range distributions, short-term accumulated loads and the Miner sum are calculated in all these sea-states and loading conditions. In every sea-state a different random phase angle realisation is used.

The Miner sum over all sea-states and loading conditions is calculated as:

$$D_{lt} = \sum_i \sum_j O_i D_{i,j} \quad (2.45)$$

in which O is the occurrence fraction of loading condition i , and $D_{i,j}$ is the Miner sum accumulated in sea-state j and loading condition i .

The fatigue life (in years) is calculated as:

$$Life = \frac{N_S T_S}{24 \cdot 365 \cdot 3600 D_{lt}} \quad (2.46)$$

in which N_S is the number of sea-states and T_S is the length of the time-traces (in seconds).

The long-term accumulated load, L_{lt} , is calculated as:

$$L_{lt} = \sum_i \sum_j O_i L_{i,j} \quad (2.47)$$

3 Application of Long-Term Fatigue Model

In the previous chapter, a time-domain model for fatigue life assessment of structural members in the deck, side-shell and bottom of a FPSO was presented. In this chapter, the feasibility of the model in terms of computational time will be demonstrated. Furthermore, the sensitivity of various parameters to the accumulated loading will be investigated. These parameters are: the contribution of different loads, wave diffraction and radiation, non-linear roll damping, wave spreading, the contribution of wind waves and swell, and sensitivity to loading condition and environmental data.

3.1 Length of Time-Traces

Time-domain simulations with long time-series are time-consuming. Below, it will be demonstrated that short time-series can be used in a long-term fatigue calculation. This is due to the following two reasons:

- Different phase realisations for time-series generation result in different time-series and short-term load accumulations. The shorter the time-series, the larger this spreading will be. However, it will be shown that the expected value of the short-term accumulated loading is virtually independent of the length of the time-series.
- Load accumulation and fatigue damage are built-up through many sea-states. The summation of the load accumulations in many sea-states gives the long-term accumulated load. It will be shown that the variation in the long-term accumulated is small in comparison to the variation in the short-term accumulated load due to the summation over many sea-states.

It will be shown that the use of short time-traces reduces the computational time significantly, which makes the formulated time-domain model feasible from a computational point of view.

3.1.1 Fatigue Accumulation in a Sea-State

The load accumulation and fatigue damage in a given sea-state are directly related to the standard deviation and the response period of the stress response. This is illustrated below.

The stress range distribution of a narrow-banded stress time-series can be described with a Rayleigh distribution as [57]:

$$f(\Delta s) = \frac{\Delta s}{4\sigma^2} \exp\left(-\frac{\Delta s^2}{8\sigma^2}\right) \quad (3.1)$$

in which $f(\Delta s)$ is the stress range probability and σ is the standard deviation of the stress response.

The number of stress cycles as function of the stress range, $n(\Delta s)$, is given as:

$$n(\Delta s) = f(\Delta s) \frac{T_S}{T_z} \quad (3.2)$$

in which T_z is the mean zero upcrossing period of the stress response, and T_S is the sea-state duration.

The accumulated load, L , in a sea-state is given as:

$$L = \int_{\Delta s=0}^{\infty} \Delta s^3 n(\Delta s) \Delta s \quad (3.3a)$$

or in discrete form:

$$L = \sum_i \Delta s_i^3 n_i \quad (3.3b)$$

in which n_i is the number of counted cycles in stress bin Δs_i .

In this formulation, a SN curve with a constant slope of 3 is used. As was discussed in chapter 2, it is convenient to describe the distribution by a single quantity. This quantity is the accumulated load, which is a constant times the Miner sum in case the slope of the SN curve has a constant value of 3.

An example of this stress cycle distribution in a 3-hour sea-state is shown in figure 3.1. In this example, the standard deviation of the stress is 0.3 N/mm² and the mean zero upcrossing period is 5 seconds. The accumulated load per stress bin ($\Delta s^3 n$) is also shown in the figure.

In this example, the long-term accumulated load as calculated with equation (3.3) is 1760 MPa³. The equivalent stress range that gives this same equivalent load accumulation can be calculated as:

$$\Delta s_{eq} = \left(\frac{L}{N} \right)^{1/3} \quad (3.4)$$

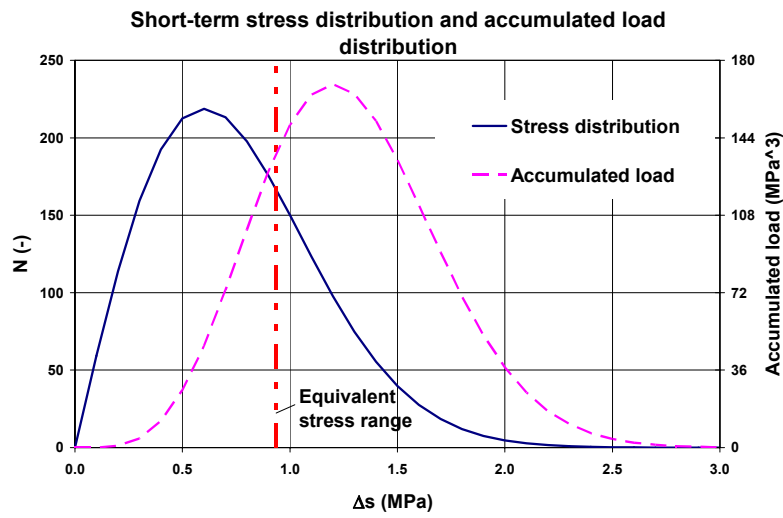


Figure 3.1 Rayleigh stress distribution and accumulated load distribution

In this example, the equivalent stress range is 0.93 MPa. The equivalent stress range is also shown in figure 3.1.

It can be mathematically demonstrated that this equivalent stress range is equal to 3.11σ . More general, the accumulated load can be written in terms of the standard deviation and mean zero upcrossing period as:

$$L = (3.11\sigma)^3 \frac{T_S}{T_z} \quad (3.5)$$

This equation shows that the accumulated load is proportional to the third power of the standard deviation and inversely proportional to the mean zero upcrossing period.

In figure 3.2, the short-term accumulated load in a 3-hour sea-state is shown as function of the standard deviation of the stress. For comparison, the mean zero upcrossing period of 5 s and 10 s are plotted. The accumulated load is sensitive to the standard deviation. Doubling the magnitude of the standard deviation, from for example 0.4 MPa to 0.8 MPa, increases the accumulated load with a factor 8. The accumulated load is proportional to the number of stress cycles and inversely proportional to the mean zero upcrossing period. Reducing the mean zero upcrossing period from 10 to 5 seconds increases the accumulated load with a factor 2.

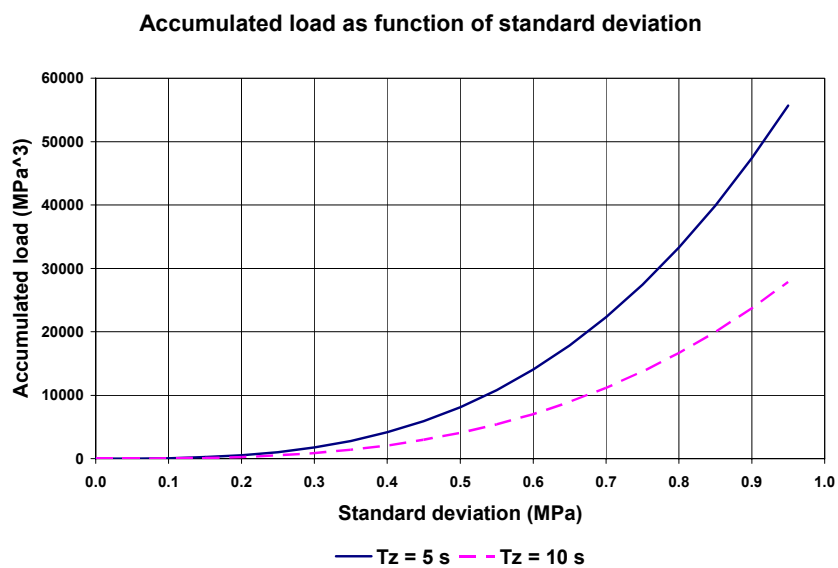


Figure 3.2 Accumulated load as function of standard deviation

3.1.2 Distributions of Stochastic Parameters in a Sea-State

Time-series with different phase realisations have different statistical properties. This makes the standard deviation, the mean zero upcrossing period and short-term accumulated load stochastic quantities. Their distributions depend on the length of the time-trace.

The nature of these distributions is investigated in a sea-state with a significant wave height of 3.0 m and a mean zero upcrossing period of 7.2 seconds. The wave spectrum is described with a JONSWAP formulation with a peak parameter of 3.3. This spectrum is shown in figure 3.3.

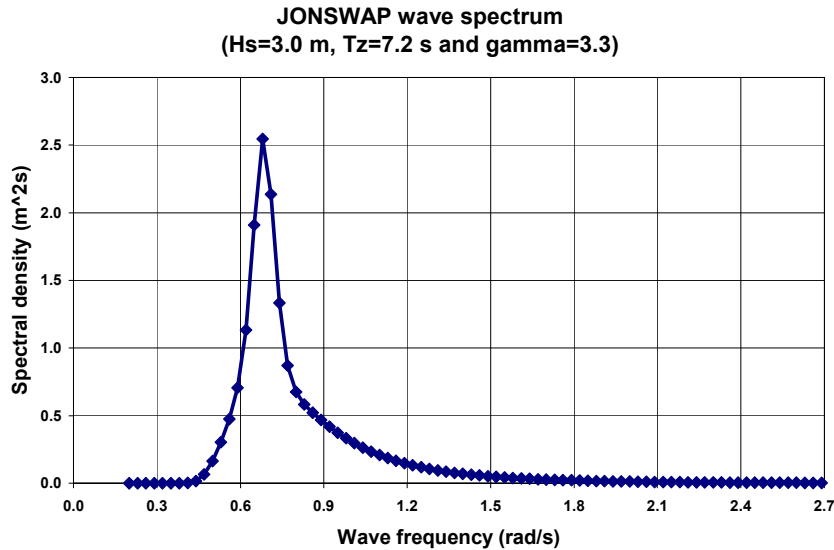


Figure 3.3 JONSWAP wave spectrum

Wave trains with different lengths and different phase realisations are calculated. The length of the time-series and the number of simulations are summarised in table 3.1. Fewer time-series have been generated for the 1-hour and 3-hour simulations, considering that the spreading of the statistical parameters is smaller in longer than in shorter time-series.

Time-trace duration (s)	Number of simulations
200	1000
400	1000
800	1000
1800	1000
3600	200
10800	50

Table 3.1 Performed time-trace simulations

The wave trains, $\zeta(t)$, are calculated from the wave spectrum, S_{ζ} , as:

$$\zeta(t) = \sum_{n=1}^N \sqrt{2S_{\zeta}(\omega_n)\Delta\omega} \cos(\omega_n t + \varepsilon_n) \quad (3.6)$$

in which ω_n is the wave frequency and ε_n is a random phase angle, drawn from a uniform distribution between 0 and 360 degrees and N is the number of wave frequencies.

To avoid anti-aliasing, the sampling frequency needs to be higher than the Nyquist frequency, which is given as:

$$f_n = 2f_{\max} = \frac{\omega_{\max}}{\pi} \quad (3.7)$$

in which ω_{\max} is the highest wave frequency in the response spectrum. (2.7 rad/s in the current calculations) The time-series are calculated with a sampling frequency of 1 Hz (sampling time of 1 s).

The time after which the time-series repeats is:

$$T_R = 2N\Delta t \quad (3.8)$$

in which Δt is the sampling time of the time-series.

The longer the time-series, the more time-steps need to be evaluated, but also more wave frequencies need to be evaluated per time-step. For example, consider a 200 second time-series and a 3-hour time-series. Because the 3-hour time-series is 54 times longer, 54 times more wave frequencies need to be evaluated per time-step, and 54 times more time-steps need to be evaluated in the 3-hour sea-state. This means that the amount of computations is in the order of $54^2 \approx 2900$ times more for the 3-hour time-series than for the 200-second time-series.

The significant wave height, mean zero upcrossing period and accumulated load are calculated for each simulated wave train. The significant wave height, H_s , is calculated from the standard deviation, σ_ζ , of the wave train as:

$$H_s = 4\sigma_\zeta \quad (3.9)$$

The mean zero upcrossing period is determined by counting the upcrossings from the time-series. The short-term stress distribution is counted from the time-series through rainflow counting with the algorithm as described by ASTM [50]. The short-term load accumulation is calculated from this distribution with equation (3.3b).

The 3-hour accumulated wave loading, L_{3H} , is calculated as:

$$L_{3H} = L \frac{10800}{T} \quad (3.10)$$

in which T is the time-trace duration and L is the short-term wave accumulation.

Distributions of the significant wave height, mean zero upcrossing period and 3-hour accumulated wave load are made for each time-trace length. The expected value and the coefficient of variation (COF) of these distributions are determined and reviewed. The COF is defined as:

$$COF = \frac{\sigma_D}{\mu_D} \times 100\% \quad (3.11)$$

in which σ_D is the standard deviation of the distribution and μ_D is the expected value of the distribution.

Figure 3.4 shows the distribution of the accumulated wave load for the 200-second and 1800-second time-series. The standard deviation of the 200-second distribution is larger than for the 1800-second distribution, but the expected values are similar.

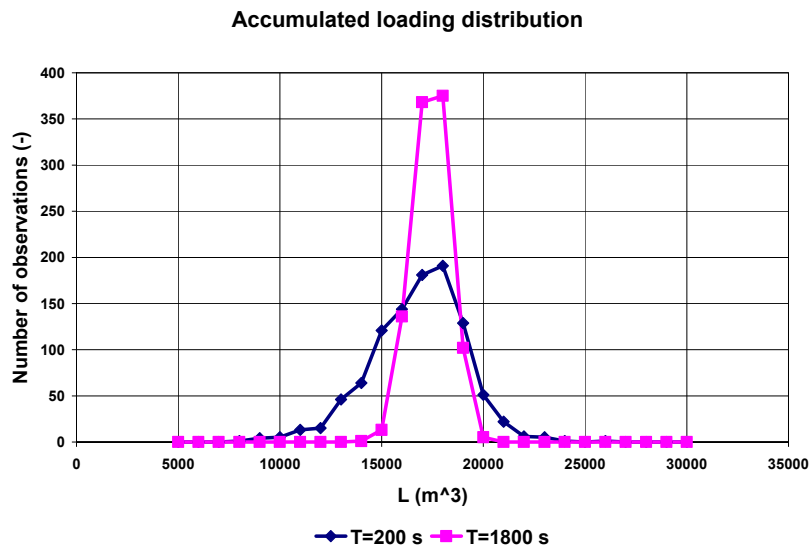


Figure 3.4 Distribution of accumulated wave load

Figure 3.5 shows the expected value and coefficient of variation (COV) of the significant wave height as function of the time-trace length. The expected value and COV of the mean zero upcrossing period as function of the time-trace duration are shown in figure 3.6, and the expected value and COV of the accumulated wave load as function of the sea-state duration are given in figure 3.7. These graphs are also summarised in table 3.2.

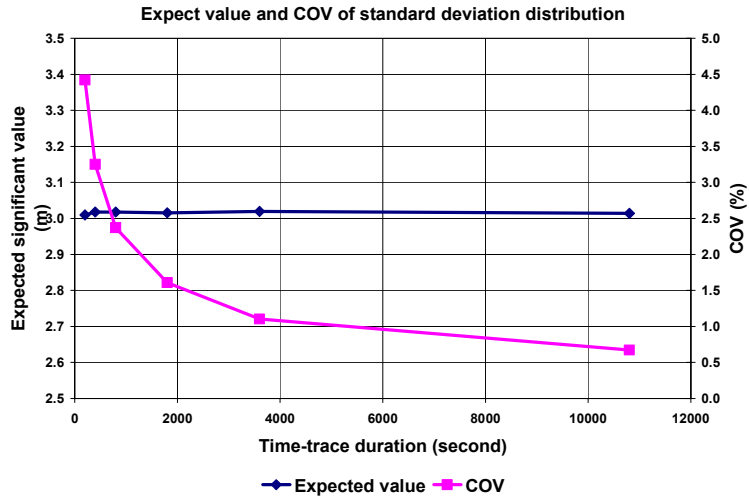


Figure 3.5 Expected value and COV of standard deviation distribution

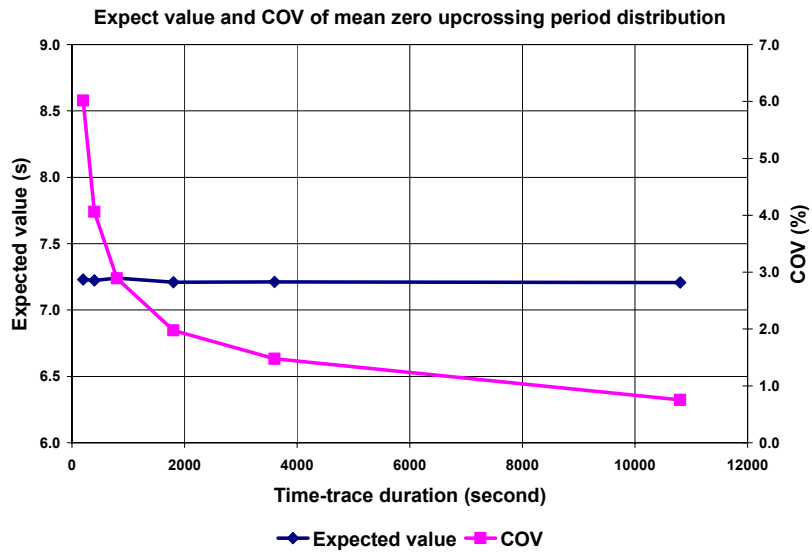


Figure 3.6 Expected value and COV of mean zero upcrossing distribution

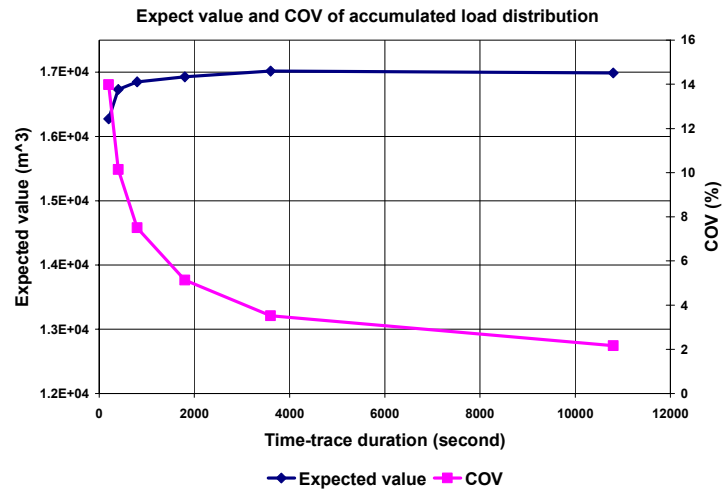


Figure 3.7 Expected value and COV of load accumulation distribution

Time-trace duration (s)	Significant wave height		Mean zero upcrossing period		Accumulated load (3 hour)	
	Mean (m)	COV (%)	Mean (s)	COV (%)	Mean (m ³)	COV (%)
200	3.0	4.4	7.2	6.0	16273	14.0
400	3.0	3.2	7.2	4.1	16731	10.1
800	3.0	2.4	7.2	2.9	16852	7.5
1800	3.0	1.6	7.2	2.0	16929	5.1
3600	3.0	1.1	7.2	1.5	17018	3.5
10800	3.0	0.7	7.2	0.8	16988	2.2

Table 3.2 Expected values and COV of distributions

The mean values in the significant wave height distribution and mean zero upcrossing period are virtually independent of the time-series duration. The COV of the significant wave height distribution and mean zero upcrossing period decreases rapidly with increasing time-trace duration.

The length of the time-trace has a small effect on the mean value of the load accumulation. As can be observed in figure 3.4, the distribution is not entirely symmetrical. This skewness is much smaller in the 1800-second distribution, since the probability of cycles with larger magnitude is larger in longer time-series. To illustrate, the maximum double-amplitude in a Rayleigh distribution, is directly proportional to the number of wave cycles:

$$D_{\max} = 2\sqrt{2\ln\left(\frac{T}{T_z}\right)}\sigma_D \quad (3.12)$$

in which T is the time duration of the sea-state, T_z is the mean zero upcrossing period and D_{\max} is the maximum value.

This relation shows that the probability of higher values increases in longer sea-states.

Figure 3.8 shows a distribution with a 200-second wave-train and a distribution with a 3-hour wave-train. These distributions were determined by rainflow counting. Longer time-series contain more cycles and provide a better description of the short-term response distribution.

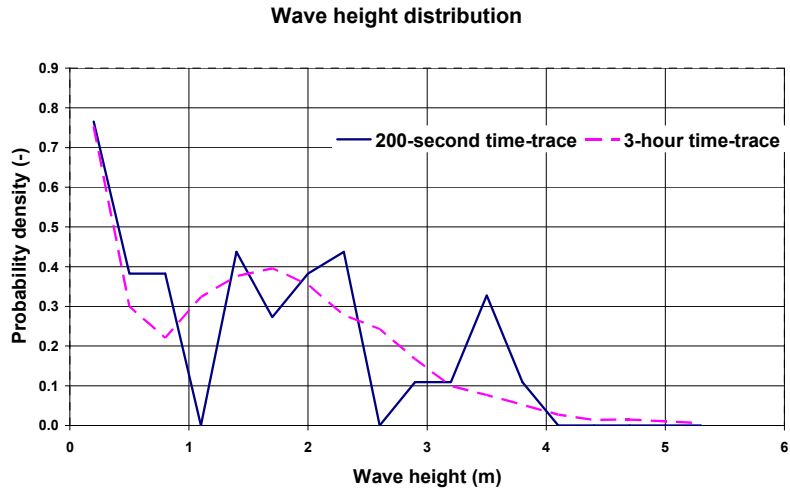


Figure 3.8 Wave height distribution (determined by rainflow counting)

3.1.3 Fatigue Accumulation through Sea-States

Load accumulation and fatigue damage are built up over a long period of time. As will be illustrated, random variations in the accumulated load within sea-states tend to level out over time. For that reason, long-term load accumulation and fatigue damage are associated with the expected value rather than with the standard deviation of the load accumulation distribution. Because of the many sea-states, the long-term variation in long-term accumulated load reduces significantly and the short-term variation in the short-term loading becomes of secondary importance.

To illustrate this, the long-term wave load accumulation is calculated as function of the number of sea-states. The long-term wave load accumulation is calculated as:

$$L_{lt} = \sum L_{3h} \quad (3.13)$$

This calculation was made for the time-traces lengths of 200, 400, 1800 and 10800 seconds with the short-term accumulated load data described in section 3.1.2.

The long-term accumulated wave load as function of the number of sea-states is shown in figure 3.9. The 200 second time-series and 10800 second time-series give a similar development of the long-term accumulated load in time. It was discussed earlier in section 3.1.2 that the use of shorter time-series gives slightly lower accumulated wave loads. In this case, the long-term accumulated load with the 200-second simulations is 5% lower than with the 3-hour time-traces and the 400-second simulations give 2.5% lower long-term accumulated load than the 3-hours simulations.

To compare, if a fatigue life of 25 years would be calculated with 3-hour simulations, a fatigue life of 26 years would be found with 200-second simulations. The results of fatigue calculations are sensitive to input data, because the accumulated load is proportional to the third power of the stress range. Considering this, the accuracy of the 200-second time-series is deemed acceptable.

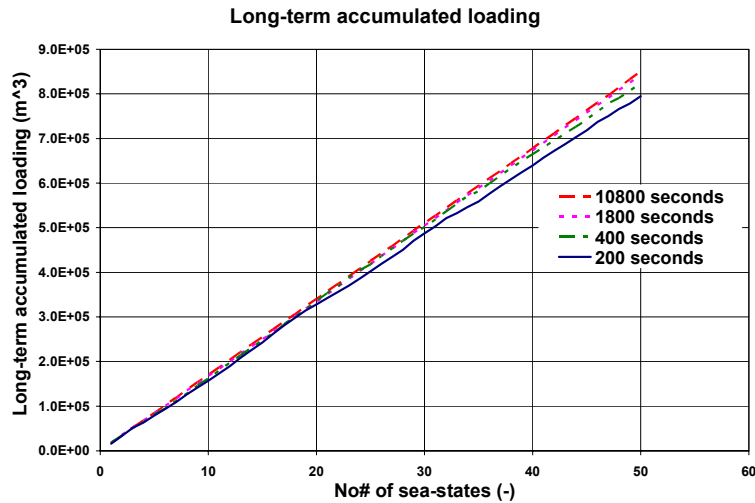


Figure 3.9 Long-Term Load Accumulation

3.1.4 Fatigue Accumulation on the Side-Shell

The above illustrates why short time-series can be used in the fatigue assessment with many sea-states. In this section, a fatigue calculation with different time-trace durations on a side-shell structure is performed. These calculations are made for the Glas Dowlr at the Sable field, offshore South-Africa. The Sable field is exposed to both the Indian Ocean and the Atlantic Ocean. Apart from local wind waves, significant swell conditions are encountered at the Sable field. These swell conditions can originate from both the Atlantic Ocean and the Indian Ocean. As will be shown later, swell has a significant contribution to the load accumulation at this field.

The developed model that is described in chapter 2 is used for these calculations. One year of environmental data, at the Sable field offshore South-Africa is used in the calculations. Wind, wind wave, current and swell data are specified per 6-hour period. The data is obtained through hindcasting and validated against available measurements and satellite data. For wind and current, the speed and direction are specified, and for wind waves and swell, the significant wave height, mean zero upcrossing period and direction are specified. As was specified in the metocean data, the wave spectra are modelled with a JONSWAP wave spectrum. A peak factor of 1.5 was used for wind waves and a peak factor of 4.0 for swell. The dataset is explained in further detail in appendix A.

The long-term load accumulation are made for 21 longitudinals for time-series lengths of 200, 400, 1800, 3600 and 10800 seconds. The used structural data is specified in appendix A and is representative for the side-shell of the Glas Dowlr.

The calculations are made for Glas Dowlr in full-load condition. Motions and section loads were calculated in the FPSO Integrity JIP [59]. These transfer functions are used in the present long-term load accumulation. A summary of these transfer functions is given in appendix A.

Figure 3.10 shows the long-term load accumulation model calculated as function of the height above the Mean Water Line (MWL) when using different time-trace lengths. The figure shows a good resemblance between the calculations with different time-trace lengths. The calculations with 200 second time-trace duration give slightly lower accumulated loads than the 3-hour simulations. The reason for this was already explained in section 3.1.2. For a fatigue calculation, the resemblance can be called good.

The calculated long-term stress distributions at the deck longitudinal and side-shell longitudinals L40, L38 and L24, with time-series of 200, 400, 1800, 3600 and 10800 seconds per sea-state, are shown in the figures 3.11 – 3.14. The heights of these longitudinals above/below the Mean Water Line (MWL) are summarised in table 3.3. The intermittent wetting effect occurs in L40, where the sideshell submerges in wave crests, and in L38 where the side-shell emerges in wave troughs. The deck longitudinal is only exposed to global loads, where L24 is exposed both to wave pressure and global loads.

The long-term stress cycle distributions of all longitudinals are not sensitive to the time-trace duration. The stress distributions of L40 and L38 can not be captured accurately by a theoretical distribution such as the Weibull distribution.

A reasonable representation of the load accumulation and fatigue damage can be obtained by using short time-series. This saves significant computational time. The 3-hour calculations took more than 4.5 months to complete, where the 200 second calculations were completed within 1.8 hours. The used computer for the calculations was a Pentium III processor with 998 MHz clock speed. As discussed earlier, this reduction in computational time is a result of the fact that in longer time-series more wave frequencies need to be evaluated per time-step, and that more time steps need to be evaluated.

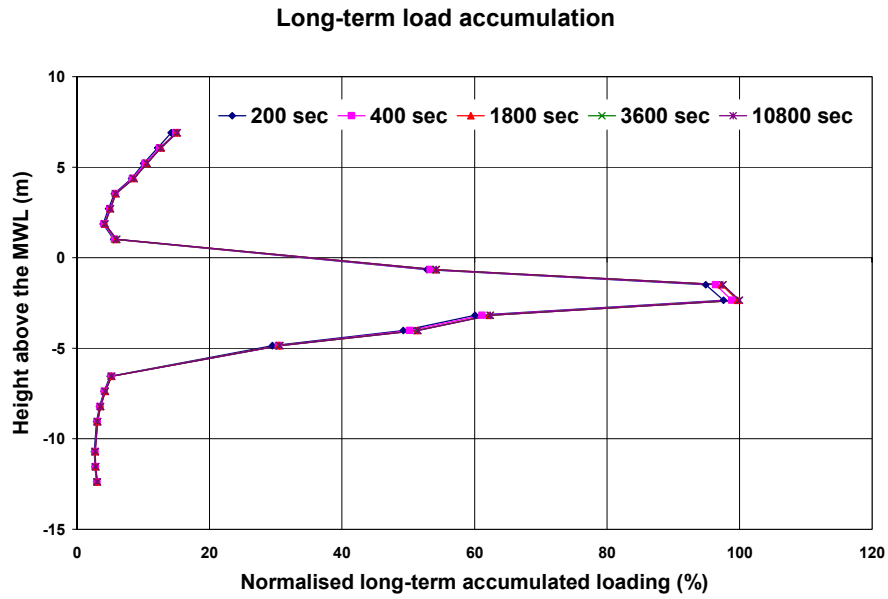


Figure 3.10 Long-term load accumulation as function of height of the vessel

Longitudinal	Height above MWL (m)
Deck longitudinal	6.3
Side-shell longitudinal L40	1.02
Side-shell longitudinal L38	-0.66
Side-shell longitudinal L24	-12.383

Table 3.3 Location of longitudinals relative to the MWL

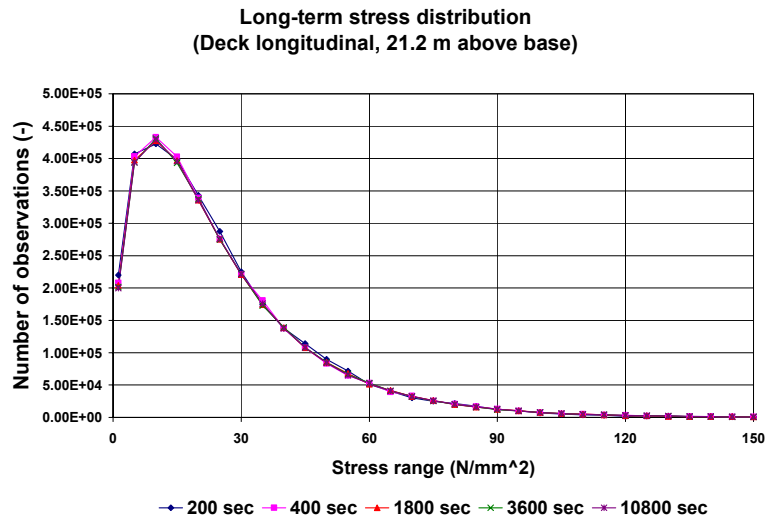


Figure 3.11 Long-term stress distribution in deck longitudinal

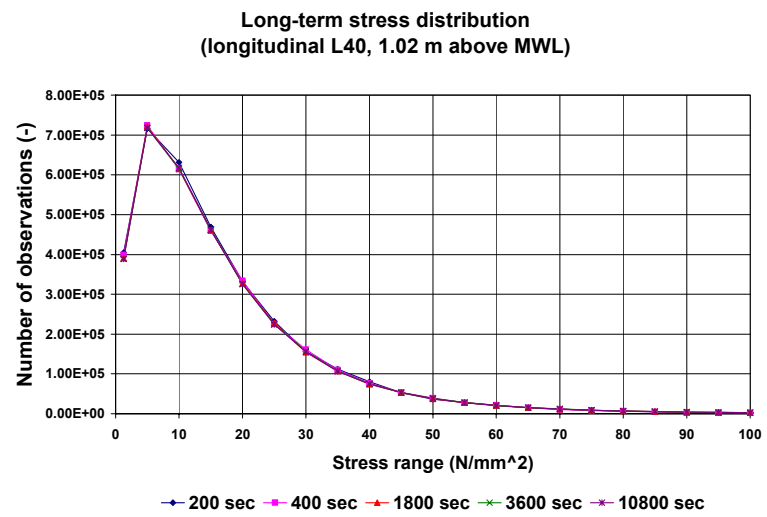


Figure 3.12 Long-term stress distribution in side-shell longitudinal L40

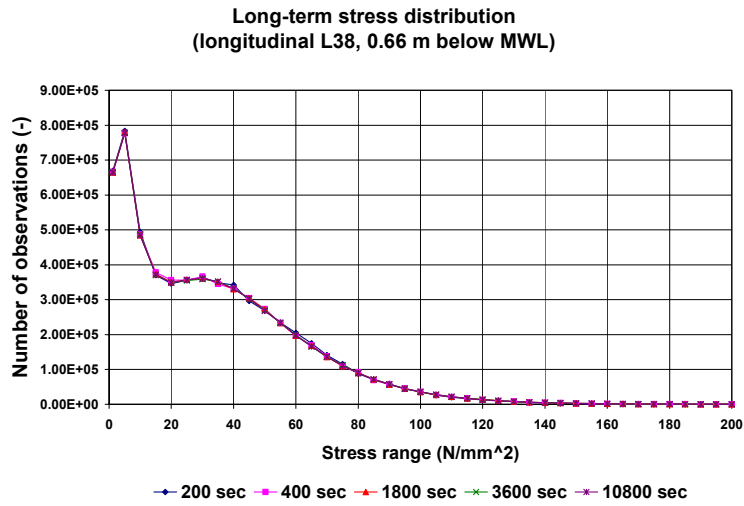


Figure 3.13 Long-term stress distribution in side-shell longitudinal L38

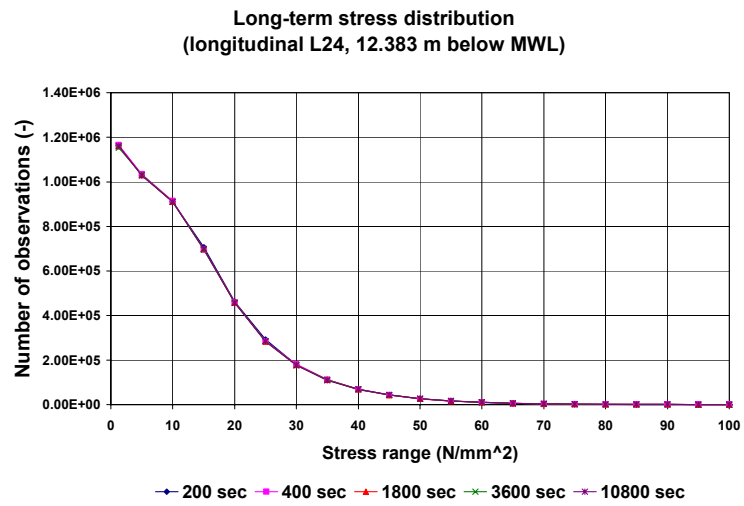


Figure 3.14 Long-term stress distribution in side-shell longitudinal L24

3.2 Contribution of Loads

As explained in chapter 2, different loads contribute to the long-term accumulated load. The loads that are taken into account in the model are: the wave pressure, the Vertical Wave Bending Moment (VWBM), the Horizontal Wave Bending Moment (HWBM) and cargo pressure. The contribution of these loads on the total load accumulation depends on the location. In this section, the contribution and correlation between the different loads are investigated. The 200-second calculations that were described in section 3.1.4 are used as basis.

To explain the development of the accumulated load over the height of the side-shell, the long-term load accumulation has been recalculated for the VWBM, HWBM, wave pressure and ballast pressure separately, with time-domain simulations of 200 seconds. The result is shown in figure 3.15.

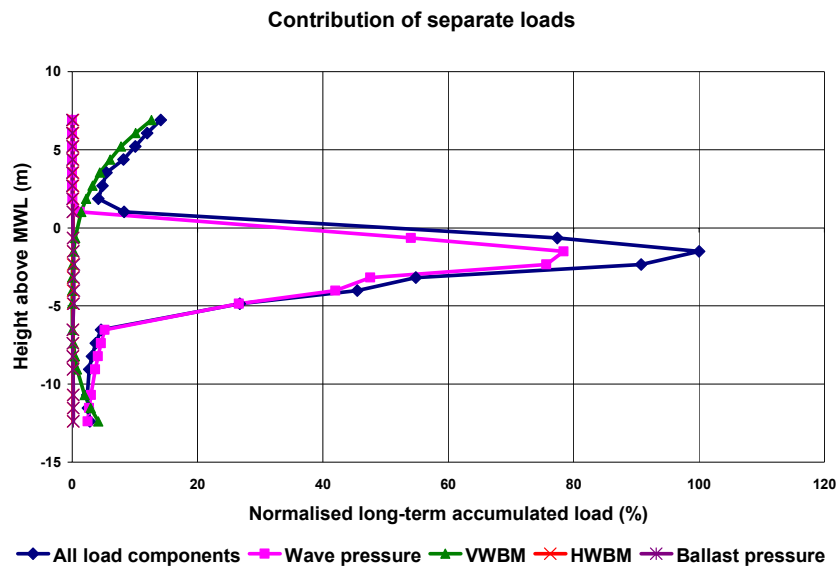


Figure 3.15 Contribution of separate loads

Depending on the locations on the side-shell, the VWBM and wave pressure are the loads that contribute most to the long-term accumulated load. The HWBM and ballast pressure contribute less to the long-term accumulated load. (Their contribution is small, but not negligible.)

The side-shell can be divided in four locations with different wave pressure regimes. These locations were previously described in chapter 2 (figure 2.9). From top to bottom, these areas are: (1) locations above wave crests where no wave pressure acts upon the structure, (2) locations above the mean waterline (MWL) that are exposed to wave pressures in wave crests, (3) locations below the MWL that emerge in wave troughs, and (4) area below the MWL that do not emerge in wave troughs.

The long-term accumulated load in locations in (1) is mainly induced by the VWBM. The deck receives most load accumulation, since it is situated furthest away from the neutral axis of the hull-girder.

Locations in (2) are exposed to wave pressures in wave crests. The accumulated load due to these pressure loads is small. Since these locations are also located near the neutral axis of the hull-girder, the contribution of the VWBM is also small.

The contribution of the VWBM is still small at locations in (3), because they are situated near the neutral axis of the hull-girder. The wave pressure contributes most to the long-term accumulated load. The magnitude of the long-term accumulated load increases downward, because the locations emerge less in wave crests, and consequently receive a larger wave pressure amplitude in the wave trough. In (3) the distance to the MWL is such that the pressure decay is not significant.

The load accumulation is induced for a significant portion by the VWBM and the by the wave pressure at locations in (4). The contribution of the wave pressure decreases downward, because of the pressure decay with increasing distance below the surface. The contribution of the VWBM increases with increasing distance below the MWL, since the distance to the neutral axis increases.

A positive VWBM induces a tensile stress in the deck, but a compressive stress in the bottom. Consequently, stresses induced by the VWBM above the neutral axis of the hull-girder are in counter-phase with VWBM stresses below the neutral axis. This means that the phase relation between stresses induced by VWBM and the other loads are different below and above the neutral axis.

As shown in figure 3.15, the long-term load accumulation of all load components together is larger than the sum of the load accumulations of the separate loads. The phase relations between the different loads are important and need to be taken into account correctly.

3.2.1 Phase Relations

The stress at the hotspot is induced by different loads. These loads are added in time-domain and, depending on their phases, their combined fatigue damage may be more or less than the sum of the fatigue damages that they induce individually. As was discussed in chapter 2, phase relations are important and need to be maintained between loads for an accurate fatigue assessment. Their influence on load accumulation is investigated below.

Consider the time-series of the 3-hour stresses R_1 , R_2 and R_3 . These time-series have been calculated with equation 3.6. The phase realisations have been drawn from a uniform distribution between 0 and 360 degrees. For R_1 and R_2 , the same phase realisations have been used to calculate the time-series. A different phase realisation was used for the calculation of R_3 . This makes that R_1 and R_2 are stochastically correlated and R_1 and R_3 are stochastically uncorrelated.

The standard deviations and mean zero upcrossing periods of the time-series for the processes R_1 , R_2 and R_3 are given in table 3.4. The standard deviation of R_1 is approximately a factor 10 higher than that of R_2 and R_3 . The mean zero upcrossing periods of R_1 , R_2 and R_3 are almost the same. The accumulated load has been determined by rainflow counting and is given in the last column in table 3.4.

Consider the stresses:

$$R_4 = R_1 + R_2 \quad (3.14a)$$

and:

$$R_5 = R_1 + R_2 \quad (3.14b)$$

The standard deviation, mean zero upcrossing period and accumulated load of R_4 and R_5 are also given in table 3.3. The standard deviation of R_4 (summation of 2 correlated time-series) is 9% higher than the standard deviation of R_5 (summation of 2 uncorrelated time-series). The accumulated load of R_4 is 33% higher than the accumulated load of R_5 .

This shows that small loads with high correlation with the other response can increase the load accumulation significantly and that the phase relations between loads need to be taken into account correctly.

Response	St. dev. (MPa)	Tz (s)	L (MPa³)
R1	0.74	10.5	11209
R2	0.07	10.5	11
R3	0.07	10.4	12
R4=R1+R2 (correlated)	0.81	10.5	14919
R5=R1+R3 (Uncorrelated)	0.74	10.5	11253

Table 3.4 Influence of phase relation

3.3 Wave Diffraction and Radiation

In this section, the contribution of wave diffraction and radiation on load accumulation is investigated. Wave diffraction and radiation effects were previously discussed in chapter 2. It was discussed that the relative wave elevation RAOs from the 3-D diffraction calculations showed (non-physical) numerically unstable behaviour in high wave frequencies, see figure 2.18. Rather than using these transfer functions, an empirical correction for wave diffraction and radiation on the relative wave elevation from the undisturbed wave train is used in this thesis. This correction is a function of wave direction and wave frequency. The correction was discussed in chapter 2. The empirical correction method will be tested in chapter 5 where a comparison will be made between measured and calculated responses.

The calculations that are described in section 3.1.4 are used as basis for the comparison. Radiation and diffraction were taken into account in these calculations. The calculations were made again, using the same input, but omitting the correction for wave diffraction and radiation.

Figure 3.16 shows the calculated long-term accumulated loads with and without wave diffraction and radiation. The wave diffraction and radiation correction only affect the wave pressure and not the global loads. There is no influence in the deck area and minor influence in the bottom longitudinals. The effects of wave diffraction and radiation are most pronounced around the MWL. Wave diffraction and radiation increase the load accumulation in this area, in this case by more than 20%. Wave diffraction and radiation have a significant effect on the long-term load accumulation and need to be taken into account.

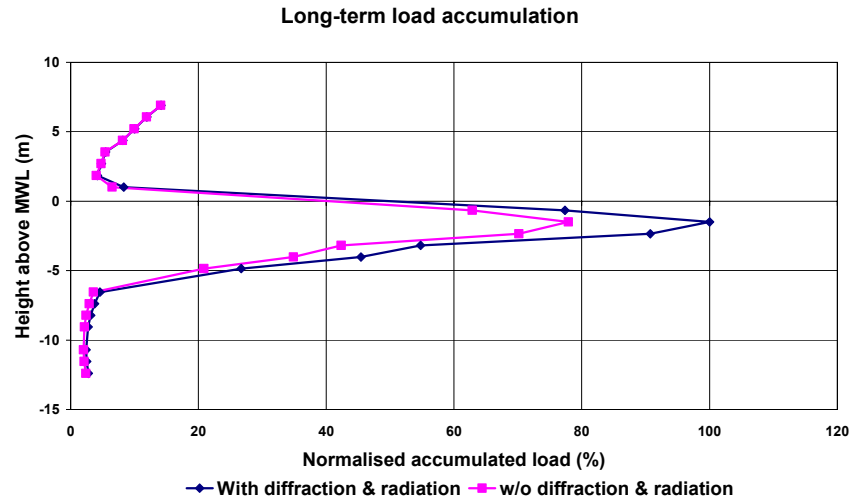


Figure 3.16 Influence of radiation and diffraction effect

3.4 Roll Damping

3.4.1 Physics of Roll Damping

The roll motions of a vessel are non-linear, mainly due to the non-linearity in the roll damping [62]. Strip theory and diffraction theory are not capable to calculate non-linear roll damping.

Empirical methods are commonly used to calculate non-linear roll damping coefficients [63]. Additionally, roll damping coefficients may be determined from model tests. A third possibility to evaluate non-linear roll damping coefficients is with advanced numerical methods, such as Computational Fluid Dynamics (CFD), see for instance Spiros et al [64].

The roll damping can be divided in a linear part and a quadratic part [65]. Figure 3.17 shows as example the trend in roll damping coefficient as function of the roll amplitude. The roll damping coefficient depends on the magnitude of the roll motion. Consequently, different roll damping coefficients should be used in different sea-states.

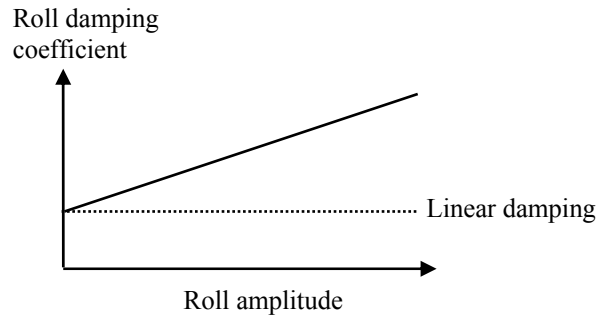


Figure 3.17 Roll damping coefficient as function of roll angle

Ikeda, Himeno and Tanaka [66] distinguish the following roll damping components:

- Friction damping (B_F),
- Lift damping (B_L),
- Wave damping (B_W),
- Eddy damping (B_E),
- Bilge keel damping through normal force on bilge keels (B_{BKN}),
- Bilge keel damping through pressure distribution over the hull (B_{BKH}).

The effective viscous roll damping is given as the sum of all these separate components [66]:

$$B_e = B_F + B_L + B_W + B_E + B_{BKN} + B_{BKH} \quad (3.15)$$

3.4.2 Effect of Roll Damping on Fatigue

Much of the recent research in the field of roll motions of FPSOs focuses on the prediction and mitigation of large roll motions. See for instance the roll JIP [69], which investigates prediction models for roll motions of FPSOs and means to mitigate the risk of large roll motions. Kragtwijk et al. [70] discuss that large roll motions may occur in relatively mild sea-states where the vessel is not heading into the swell. Ferrari et al. [71] and Na et al. [72] discuss that bilge keels are effective means to mitigate large roll motions.

The roll motions in day-to-day sea-states are generally small. Since wave frequencies are generally not near the natural roll period of the vessel in day-to-day conditions, bilge keels will not significantly reduce small roll motions in day-to-day sea-states. This suggests that the influence of non-linear roll damping on the fatigue damage/long-term accumulated load is limited.

To investigate the effect of non-linear roll-damping, long-term load accumulation calculations are made at the Glas Dowl for 1 year at the Sable field, offshore South-Africa. The same environmental data and structural data as used in section 3.1.4 are used in these calculations. The calculations are made for full-load condition. The loading condition data and structural data are specified in appendix A. Different long-term load calculations were made with RAOs calculated for different roll-damping coefficients and the results of these calculations were compared.

The vessel transfer functions are calculated with the strip-theory program Seaway. This program was used, since it is possible in this program to calculate quadratic roll-damping coefficients.

The motion and section load transfer functions are calculated for different roll amplitudes (ROLLAMP), ranging from 1-20 degrees with steps of 1 degrees. The non-linear roll damping has been evaluated with the (semi)-empirical method described by Ikeda et al. [73].

The significant roll amplitude was calculated per sea-state, taking into account the non-linear roll damping. A method to assess the roll motions of FPSOs taking into account the non-linear roll-damping is described by Orozco et al. [74]. They determine the correct roll damping value from the calculated roll responses. A similar approach is used below. The roll response of the vessel is calculated for a given roll damping value. From the responses, it is checked whether this roll damping value was correct. This process is repeated until the roll damping value matches with the found roll response.

Per sea-state, the roll response spectra due to wind waves and swell are calculated as:

$$\begin{aligned} S_{\phi_w} &= S_{\xi_w} RAO_{\phi} \\ S_{\phi_s} &= S_{\xi_s} RAO_{\phi} \end{aligned} \quad (3.16)$$

in which S_{ϕ_w} is the roll spectrum due to wind waves, S_{ϕ_s} the roll spectrum due to swell, S_{ζ_w} is the wind wave spectra, S_{ζ_s} is the swell spectra, and RAO_{ϕ} is the roll RAO.

The roll spectrum in combined seas, S_{ϕ_t} , is calculated as:

$$S_{\phi_t} = S_{\phi_w} + S_{\phi_s} \quad (3.17)$$

The zero-order spectral moment, m_0 , is calculated as:

$$m_0 = \int_0^{\infty} S_{\phi_t} d\omega \quad (3.18)$$

The significant roll amplitude, $\phi_{1/3}$, is calculated as:

$$\phi_{1/3} = 2\sqrt{m_0} \quad (3.19)$$

This calculation is repeated for all ROLLAMP values. The correct ROLLAMP value is determined as:

$$\phi_{1/3} = \text{ROLLAMP} \quad (3.20)$$

The calculation of the roll response in a given sea-state is shown in figure 3.18.

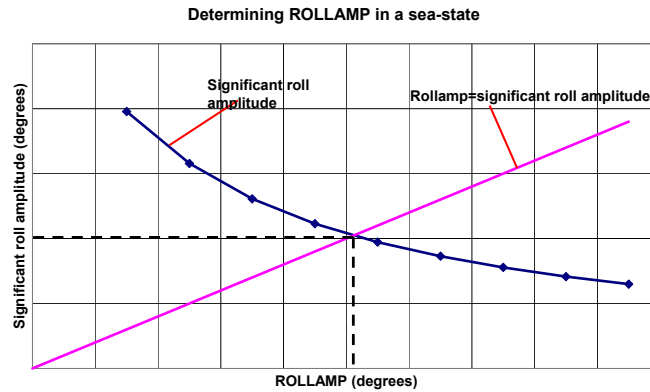


Figure 3.18 Determination of roll response in a sea-state

Per sea-state, the short-term load accumulation calculated with the correct ROLLAMP is selected and the long-term load accumulation is assessed as the sum of all these short-term accumulated loads.

Figure 3.19 shows the significant roll amplitude distribution in a year. The roll-motions in day-to-day sea-states are generally small. The significant roll angles are smaller than 1 degree in 65% of the sea-states.

The long-term accumulated load calculated for a fixed roll-amp value of 1, 3 and 5 degree are shown in figure 3.20. Furthermore, the long-term accumulated load is presented when linearising the roll-damping to the significant amplitude. Larger rollamp values give lower long-term accumulated loads, since the roll motions are smaller. The roll-damping only affects the wave pressures, and not the global loads. The effect of the roll-damping on the load-accumulation is small. This is due to the fact that the roll motions in day-to-day sea-states are small and the vessel is not excited in its natural roll period. This shows that the full non-linearity of the roll-damping does not need to be incorporated in the long-term load calculation. In this case, it is sufficient to model the roll-damping with one roll damping value.

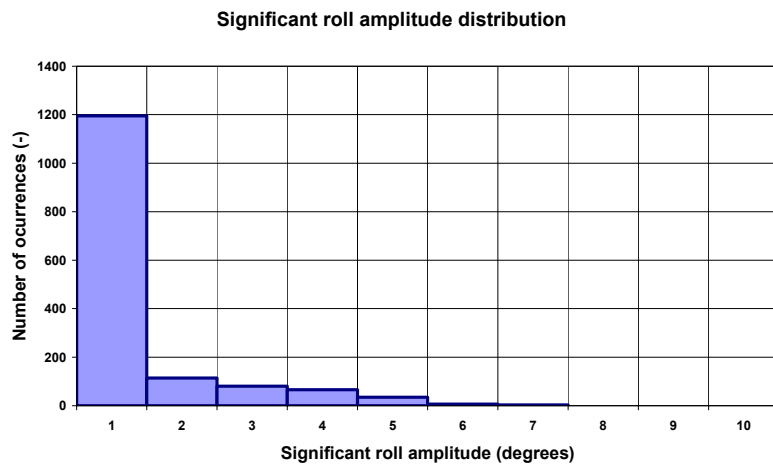


Figure 3.19 Long-term distribution of the ROLLAMP value

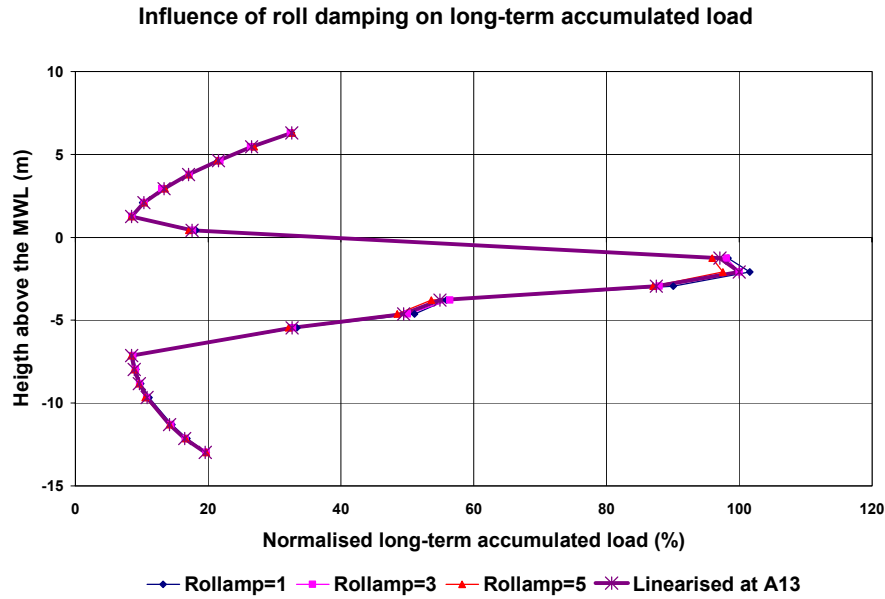


Figure 3.20 Influence of roll damping on side shell fatigue

3.5 Environmental Conditions

3.5.1 Accumulated Load as Function of Significant Wave Height

In chapter 1 and chapter 2 it was stated that most load accumulation is built-up in moderate sea-states. Mild sea-states occur regularly, but because the responses induced in these sea-states are low, their contribution in the load accumulation is limited. The induced responses in storm conditions are high, but because their occurrence is limited, their contribution in the load accumulation is small. This is investigated in the present section.

In section 3.1.4, fatigue calculations were made with a year of environmental data. The environmental data for the calculations were both wind wave and swell data per sea-state. For visualisation, the combined significant wave height in a sea-state with wind waves and swell is calculated as:

$$H_{s,c} = \sqrt{H_{s,w}^2 + H_{s,s}^2} \tag{3.21}$$

in which $H_{s,w}$ is the significant wave height of the wind wave system and $H_{s,s}$ is the significant wave height in the swell wave system.

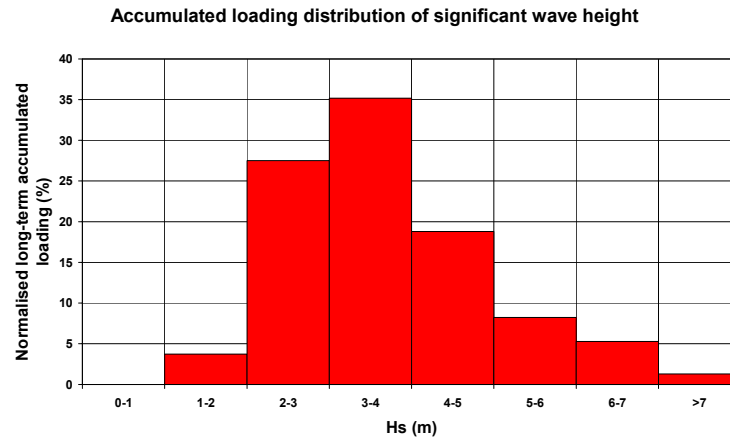


Figure 3.21 Accumulated load as function of significant wave height

The calculated short-term accumulated loads are classed per significant wave height and added up per class. Figure 3.21 shows the long-term accumulated load as function of the significant wave height. Most load accumulation is built up in moderate sea-states between 3-4 m. The accumulated load in low sea-states is small, because of low responses in these sea-states. The contribution in high sea-states is small, because they occur only rarely.

3.5.2 Contribution of Wind Waves and Swell

As was discussed in chapter 2, day-to-day sea-states can contain multiple wave systems with different characteristics and origins. Commonly, hindcasted wave data contains separate wind wave and swell data per time interval. In this section, the contribution of wind waves and swell in the total accumulated load are investigated. The long-term calculations in section 3.1.4 are used as a basis. Furthermore, additional calculations have been made for wind waves and swell separately to investigate the influence of both components on the results. The calculations were made with time-trace lengths of 200 seconds.

Figure 3.22 shows the long-term accumulated load due to wind waves, swell and due to wind waves and swell together. Most of the load accumulation is induced by the swell and the contribution of wind waves is smaller.

This is typical for the Sable field, where significant swell conditions are encountered due to its exposure to two oceans. The wave periods of swell are larger than for wind waves and are in the frequency range where they induce relatively large bending moments in the day-to-day conditions. This in contrast to the wave conditions at the North-Sea. As will be demonstrated in chapter 5, in North-Sea conditions most load accumulation is induced by wind waves and a smaller part by swell.

This calculation illustrate that both wind waves and swell need to be taken into account. The total accumulated load is larger than the sum of the load accumulation of wind waves and swell separately.

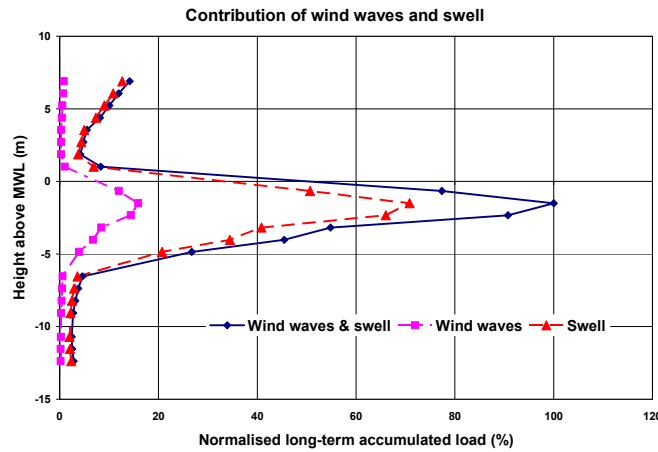


Figure 3.22 Contribution of wind waves and swell

3.5.3 Format of Environmental Data

For the present calculations, detailed hindcasted environmental data is available. However, in the design practice, it is more common practice that design wave data is only specified in the form of (onmi-directional or directional) wave scatter diagrams. The correlations between wind, waves, swell and current are lost in a scatter diagram and an assumption regarding the vessel heading towards the waves needs to be made.

In this section, the uncertainties associated with the use of a wave scatter diagram are investigated. The long-term load accumulation calculations that are described in section 3.1.4 are used as basis in this section.

The wind wave and swell data that were used in these calculations are summarised in a wave scatter diagram. With this wave-scatter diagram additional long-term load accumulation calculations are made. Furthermore, the design wave scatter diagram at the Sable field is used to make additional calculations.

Per sea-state, the significant wave height and mean zero upcrossing period due to wind waves and swell combined are calculated. The combined significant wave height is calculated with equation (3.21).

A method of finding the mean zero upcrossing period in a combined wind wave and swell sea-state is by adding the zero and second-order spectral moments.

The zero-order spectral moment, m_0 , is related to the significant wave height as:

$$m_0 = 16H_s^2 \quad (3.22)$$

The second order spectral moment, m_2 , is related to m_0 and the mean zero upcrossing period, T_z , as:

$$m_2 = \begin{cases} \frac{4\pi^2 m_0}{T_z^2} & T_z > 0 \\ 0 & T_z = 0 \end{cases} \quad (3.23)$$

Both m_0 and m_2 are calculated for wind waves and swell in a given sea-states. Wind waves and swell waves are statistically independent processes. In combined seas, the zero-order and second-order spectral moments can be added:

$$\begin{aligned} m_{0,c} &= m_{0,w} + m_{0,s} \\ m_{2,c} &= m_{2,w} + m_{2,s} \end{aligned} \quad (3.24)$$

in which the subscript c indicates combined seas, the subscript w indicates wind waves and the subscript s indicates swell.

The mean zero upcrossing period in combined seas is calculated as:

$$T_{z,c} = \begin{cases} \sqrt{\frac{m_{0,c}}{m_{2,c}}} & m_{2,c} > 0 \\ 0 & m_{2,c} = 0 \end{cases} \quad (3.25)$$

An omni-directional wave scatter-diagram is also available for the Sable field. Based on this scatter-diagram, long-term load accumulation calculation were made.

It is assumed in the calculations that the vessel is 50% of the time in headwaves, 25% of the time in bow-quartering seas (45 degrees off headwaves) and 25% of the time in beam seas (90 degrees off headwaves). Such an assumption often needs to be made in the design, because often there is no better information available.

The long-term accumulated loads over the side-shell when using the scatter diagram and the list of hindcasted environmental data are shown in figure 3.23. The calculation results are significantly different. Differences can be caused by the vessel heading assumption and by description of wind waves and swell in one wave spectrum. The format of the specified environmental data is important for the an accurate fatigue assessment.

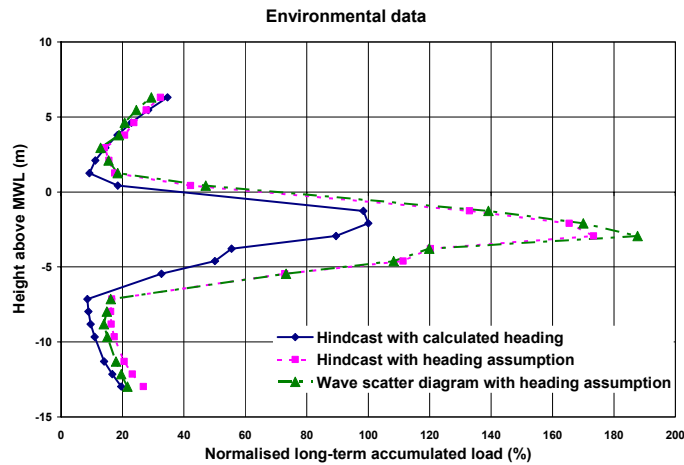


Figure 3.23 Scatter diagram vs. list of sea-states

3.5.4 Wave Spreading

Wave spreading in wave systems is commonly encountered in day-to-day sea-states [75]. In this section, the effects of wave spreading on the long-term load accumulation are investigated. Additional calculations were made to investigate the effect of wave spreading on the long-term load accumulation. The calculations with wave spreading are compared with the calculation results without wave spreading.

The calculations were made with one year of environmental data at the Sable field. The same environmental data and structural data as used in section 3.1.4 are used in these calculations.

In the present longterm load calculations, the wave spreading in the wind waves were modelled with a cosine-square distribution and swell waves were modelled as long-crested waves. The calculations were made for full-load condition, specified in appendix A. A fixed ROLLAMP value of 3 degrees was used in the calculations (see section 3.4). The transfer functions for vessel motions and section loads are calculated with the strip-theory program Seaway.

Figure 3.24 shows the long-term load accumulation with and without wave spreading. Particularly at locations near the mean waterline (MWL), where the wave pressure has a large contribution in the long-term load accumulation shows the influence of wave spreading. In the deck, the long-term accumulated load is mainly induced by the global loads. The effect of wave spreading on the long-term load accumulation is small in at these locations.

These calculations show that wave spreading has a considerable influence on the long-term load accumulation resulting from wave pressures. In this case the effect is in the order of 20%.

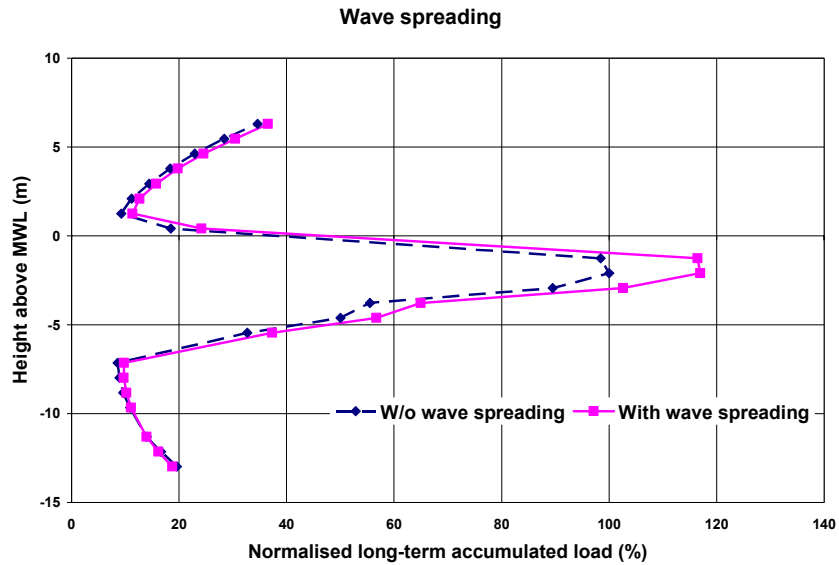


Figure 3.24 Influence of wave spreading

3.6 Vessel Loading Condition

To investigate the effect of the loading condition on the long-term accumulated load, long-term load accumulation calculations were made in 5 loading conditions, ranging from ballast load to full-load. These loading conditions are specified in appendix A. The motion and section load RAOs that are used for the long-term load calculations are determined with the strip-theory program Seaway. The RAOs have been calculated with a fixed ROLLAMP value of 3 degrees.

One year of environmental data at the Sable field is used for the analysis. These are the same environmental data and structural data that were used in section 3.1.4.

Figure 3.25 shows the long-term accumulated load as function of the height above base for the five loading conditions. The long-term accumulated load has been normalised to the maximum calculated long-term accumulated load in all longitudinals and loading conditions.

The loading condition has an important influence on the calculated long-term accumulated load, especially on the locations that are exposed to wave pressure, but also in the deck where only global loads induce fatigue damage. Representative loading conditions need to be available for a reliable fatigue analysis. Furthermore, the occurrence fraction of the loading conditions needs to be accurately known.

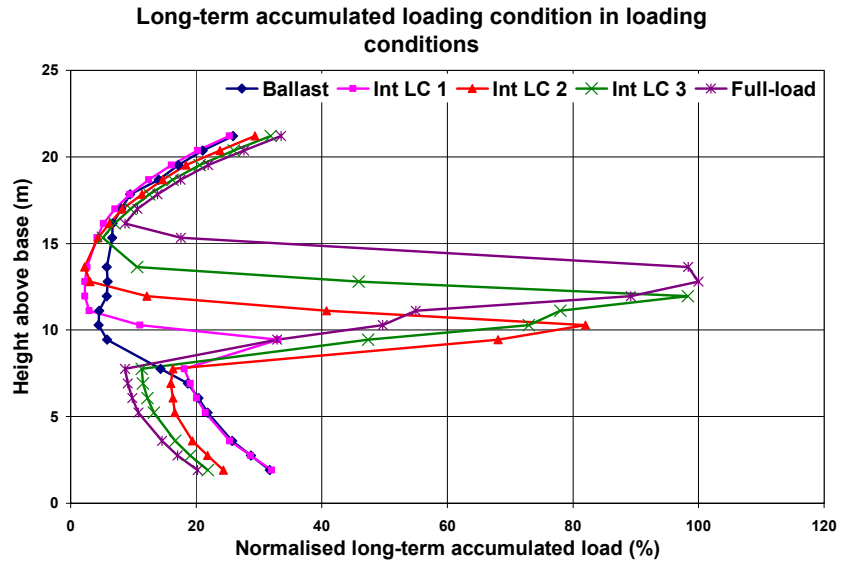


Figure 3.25 Influence of loading condition

4 Fatigue Monitoring Systems

4.1 Introduction

The development and validation of a long-term load accumulation model was described in chapter 2 and the model was illustrated in chapter 3. It was demonstrated that, apart from a physically accurate model, representative input data needs to be available for an accurate fatigue assessment. This requires a thorough knowledge of the intended operations of the vessel and the environment in which the vessel operates.

In the design, historical environmental data is generally used. As will be demonstrated in chapter 5, the actual wave conditions that the vessel encounters can be different than anticipated during design. Furthermore, sea-states are represented by theoretical spectrum formulations in design and wave spreading information is often not available. Furthermore, it is difficult to anticipate the encountered loading conditions and their occurrence fractions on forehand, since they also depend on the characteristics of the oil production and offloading rate.

The above suggests that design fatigue calculations can have significant uncertainties in them, simply because the input is uncertain. A monitoring system can be used to measure responses and remove a large part of this uncertainty in the load accumulation. The monitoring information can be used to support Inspection, Maintenance and Repair (IMR) programs, or to define life-time extension scopes during work at a yard.

The anticipated monitoring systems logs loads, but not fatigue capacity. The fatigue capacity of structural members also contains significant uncertainties. Consequently, monitoring systems can never replace inspections.

In this chapter, the application of fatigue monitoring systems (FMS) is investigated. First, a literature review of existing monitoring systems in shipbuilding and offshore industry is given. After this, a list of requirements for a FMS is specified. Finally, possible data post-processing techniques for FMSs are investigated. Most effort is put in statistical methods, since they may potentially require a simple and cost-effective measurement system.

4.2 Monitoring Systems in Shipping and Offshore Industry

Structural monitoring systems have been deployed for a wide range of applications in the shipping and offshore industry. Monitoring systems are applied for a variety of reasons, such as:

- Guidance of crew in or to avoid adverse weather conditions.
- Measurement data to support IMR programs.
- Verification and/or development of calculation procedures.
- Guidance for the crew in weather sensitive operations, such as helicopter or offloading operations on a FPSO.
- Monitoring of structural integrity through monitoring of the condition of critical structural joints.

Existing applications for structural monitoring systems in the ship-building and offshore industry are discussed below. This review is by no means exhaustive, and only a flavour of the possibilities is given. The following applications are reviewed:

- Structural monitoring systems onboard naval vessels to verify extreme load calculations during the life of the vessel,
- Structural monitoring systems onboard trading tankers to supply guidance to the crew in adverse weather conditions,
- Structural monitoring as part of Inspection, Maintenance and Repair (IMR) programs onboard tankers,
- Monitoring information to provide validation measurements for calculation procedures on sailing vessels,
- Damage monitoring onboard offshore units,
- Weather monitoring onboard offshore units for weather-sensitive operations.

4.2.1 Structural Monitoring onboard Naval Vessels

Brown [55] discusses the backgrounds for the measurements of strains onboard British naval vessels. The wave bending moment have a large contribution in the extreme bending moment and due to the slenderness of naval vessels the wave

bending moments need to be predicted with non-linear calculation methods. Operational requirements for a naval vessel demand that the vessel can sail to any part of the world with high speed despite adverse weather conditions. The vessel needs to have adequate strength to sail in all weather conditions. On the other hand these displacement vessels need to be built as light as possible to prevent extreme propulsion power requirements.

The knowledge about extreme loads that a marine vessel will encounter during its service life is limited [77]. Use of through-life monitoring can determine whether or not design methods are conservative. Furthermore, information about fatigue of the vessel is obtained through the deriving of hogging and sagging moments from the data.

Yuille [99] developed a strain recorder, which was installed on several naval vessels. He extrapolated extreme wave bending moments from the measured data and found that hogging and sagging moments could not be distinguished from the measurements. The strain recorder was improved by Smith who also added time and date. Smith found that there was little relation with the design rule that is based on balancing the vessel in a wave with height of $L/12$ and wave length equal to the length of the vessel. Furthermore he found that measurements were insufficient to check against design calculation procedures because of lack of recorded wave data. Correlating measurements with sea-states resulted in a new type of strain recorder [78]. Agreement between measurements and calculations remained poor because of the lack of accuracy in the estimated wave conditions, uncertainty in the section modulus of the vessels and because of the accuracy of the strip theory calculations. Strip theory was found to over-predict the measurements significantly [52]. Further research led to separating strains induced by the wave bending moment from whipping strains. The measurements showed that strains on Port and Starboard side of the vessel may deviate by as much as a factor of 1.5 due to horizontal wave bending.

Measurements onboard naval vessels have also been used to compare the performance of different designs. Andrews and Lloyd [79] and Clarke [80] describe trial-runs of 2 naval vessels to assess their relative performance in adverse weather conditions. Both vessels are performing the same test runs, where wave conditions are measured with a wave rider buoy. Performance criteria were: excessive vessel motions, slamming and deck wetness. It is recognised in the paper that the one ship may do worse in a particular sea-state but that in a different sea-state it may have a better performance. Because both vessels were similar in shape and dimension, this was judged to be of minor importance.

One of the key findings was that strip theory over-predicts wave bending moments by 10-20% [80]. Furthermore, differences between both vessels in performance in adverse weather were found to be significant, particularly in slamming occurrence at high speeds.

Although the measurement campaign was not intended for this purpose, the measured data has also been used for fatigue research [81]. The drive behind the research was that better understanding of fatigue can result in better design methods and help in more cost effective design. Long-term stress distributions at midship were derived from recorded strain data as input for the fatigue analysis. Very occasionally, cracks occurred in their vessels that needed immediate repairs, but the bulk of the cracks could be repaired after some time. Small fatigue cracks may influence the performance of sensitive electrical equipment because of water ingress. In the paper, it was estimated that a typical warship will experience approximately 100 fatigue cracks during its life that need repairing, which is a low number considering the amount of fatigue sensitive structural details.

4.2.2 Structural Monitoring onboard Tankers

Structural monitoring systems have been applied on trading tankers. Melitz et al. [82] describe the background of monitoring systems onboard BP tankers as part of a strategy towards the assessment of structural durability of the vessels. The immediate cause for this strategy was the near-loss of a 25000 dwt product tanker that experienced unstable crack growth at two places in the deck during sailing through the Skaggerak (Denmark). Through good seamanship, the vessel arrived safely in the port of Rotterdam. The cracking was caused by wave slamming in cold temperatures (brittle fracture).

The purpose was to identify practical measures for structural preventative maintenance or prevention thereof. Two basic risks were determined as brittle fracture due to dynamic peak loads and fatigue failure from cyclic loading. As part of this strategy, tankers were fitted with a structural monitoring system. This system was to provide measurement data but also to provide the crew information in adverse weather conditions.

The system is described by Witmer et al. [83] and by Ashcroft et al. [84]. The system contains of a suite of sensors measuring, amongst other things, vessel motions, wave pressures, strains in structural members and propulsion data. The data is presented real-time at the bridge of the vessel. This assists the crew in taking actions in adverse weather conditions, such as reducing speed or changing heading. Data can be stored for future analysis for engineering studies.

Monitoring systems can be linked to weather predictions via satellite [84]. With this information, it is possible to avoid adverse weather conditions. In case the vessel comes in adverse weather conditions the system helps the crew in taking actions and seeing the results of the actions.

Lacey and Edwards [85] and Lacey and Chen [86] discuss the application of a monitoring system on tankers owned by ARCO Marine that sail on the TAPS route (from Alaska to California). Weather conditions at the TAPS route are rough most time of the year and more severe than Northern Atlantic conditions, for which these tankers are designed. The tankers experienced damage quite often, which was thought to be caused by wave slamming. Because of the large size of the vessel slamming can not easily be observed by the crew, which increases the probability of structural damage. The solution was sought in providing the crew a means of monitoring the structural responses of the vessel and providing a means to foresee responses in bad weather to avoid bad weather conditions.

The tankers were equipped with a structural monitoring system [86]. The structural monitoring system consisted of pressure transducers under the bow foot, midship strain recorder, measurements of vertical accelerations, pitch and roll motions, engine RPM, torque, thrust and power and wind speed and direction, vessel course and position. A console was placed on the bridge from which the data could be reviewed in real-time by the crew. The system receives weather forecasts by satellite connection and enables the crew to avoid bad weather. If the vessel is in bad weather the responses of the vessel can be monitored and with this information the crew can take appropriate actions to reduce the risk of structural damage. The structural damage to the ships decreased significantly when using the system. The measured data was also used to develop a method for the prediction of slamming occurrence and severity.

Slaughter et al. [87] give a state of the art review of hull response monitoring systems. The goals of a hull response monitoring system are identified as to minimise the risk of encountering dangerous seas, alert the crew of the severity of vessel responses if in adverse weather conditions and provide guidance how to reduce vessel responses in extreme conditions. Visual display on the bridge is identified as an important feature of the systems. The right type of data should be displayed on the bridge and the presentation should be clear so that the crew can make fast decisions.

Lewis et al. [88] discuss the use of neural network techniques to provide operational guidance to the crew from recorded data. It is important that the system gives a valid advice, in case that the advice is wrong vessel responses may be increased instead of reduced. In these cases, it is better to give no advice than to give a wrong advice.

Xu and Haddara [94] also describe the application of neural networks in a monitoring system. In this system, the wave bending moments are derived from the measurements of vessel motions. In time-domain the vertical wave bending moment is expressed as a function of the heave and pitch accelerations, velocities and displacements. A neural network is built with as input the heave and pitch accelerations, velocities and displacements and as output the vertical wave bending moment. The neural network is trained with model test results. A fair agreement between predictions and measurements is found. Whipping and springing stresses can not be taken into account with the described method.

4.2.3 Structural Monitoring for Inspection, Maintenance and Repair Programs

Measurements of a structural monitoring system are also used as input for Inspection, Repair and Maintenance (IMR) programs. Brookings et al. [7] describe a structural monitoring system that is part of the ship structural integrity management. Not only loads on the vessel but also deterioration of the vessel, for instance corrosion, cause structural failures. These phenomena can not be recorded by a load measurement system. Consequently, one can not do without inspections. Brooks et al. [8] describe a hull condition monitoring scheme for bulk carriers in assisting during inspection and maintenance of bulk carriers. Monitoring will identify areas for close-up inspection. The drive behind the integrity management is the increased level of safety by awareness of the condition of the hull. Ultimately it is anticipated that increase knowledge of the hull status through monitoring will reduce overall costs.

Sanderson et al. [89] discuss the application of the monitoring of horizontal accelerations at the topside of a jacket. Failure of structural members is detected when the acceleration signature of the structure change. The system increases safety because structural failures are detected immediately. These systems also reduce inspection costs because the required number of inspections is less; underwater inspections using Magnetic Particle Inspection (MPI) are expensive. Piedras Lopez et al. [90] discuss a system in which the relation between structural response and wave measurements is described by a neural network. The system is used to determine inspection intervals and to determine which structural members need to be inspected.

4.2.4 Monitoring of Structural Damage

The systems discussed so far all measured loads on a structure. There are also systems, which directly measure crack growth in a structure. Burton et al. [95] discuss a system in which crack growth is monitored by the use of a meta-stable metal or so-called TRIP steel. After permanent deformation the material properties of these steel alloys changes from austenitic to ferritic. Austenitic and ferritic steels have different magnetic properties. These differences in magnetism can be measured and from these reading location and length of a crack can be determined. Since the damage in the TRIP steel is irreversible the method can only be used as a maximum strain sensor. To place the sensor, it must be known on forehand where the crack will develop. The material is reported to be sensitive to variations in temperature, which can be solved to some extend by choosing the suitable alloy. This method provides a good means to determine crack growth in structures once it is known where cracks may develop. The paper identifies locations that are difficult to inspect as a useful application.

Zubaydi et al. [96] describe a system that is able to detect damage in the sideshell of a ship through determining the natural frequencies of the local structure. Damage is detected from a change in the vibration signature of the structure. A neural network is built from which the extend and the location of the damage can be determined.

Cracks and crack growth can be detected by acoustic emission. Use is made of the fact that a growing crack produces high-frequency sounds that can be measured. Rogers [97, 98] describes a practical application for the offshore industry. The system is equipped with a set of microphones, which detects these sounds. The system identifies the sounds caused by cracks and with this information the location and length of the cracks in a structure can be determined. Both short-term and long-term tests can be performed with the method. In short-term tests, the test piece is overloaded and the cracks can be determined from the measurements. Long-term testing consists of monitoring the structure for a longer period, typically a couple of weeks or a few months. Cracks can be identified and the growth of cracks can be monitored, based on which an assessment is made about the criticality of a crack and the crack growth rate. This information is used to assess criticality of the crack and provide for decision support for possible repair actions.

4.2.5 Monitoring of Weather Conditions on-board Offshore Units

Weather data is of interest for weather sensitive offshore operations. Several weather sensitive offshore operations are identified by HSE [100] as helicopter operations, offloading operations, standby vessel assistance, repairs and maintenance, work overboard, etc. Sufficient environmental data should be measured to guarantee adequate safety during weather sensitive operations. Metocean data of interest on a floating offshore platform are wind, wave data, heading data and vessel motion data.

The accurate measurement of wind data is difficult, because the presence of the wind sensor itself disturbs the wind flow and because of wind shielding effects [101]. It is particularly difficult to measure wind reliably on a FPSOs, because of the weathervaning capabilities of the vessel, when the sensor shifts inside and outside wind shielded areas [100]. Feedback from the crew onboard Bluewaters FPSO 'Bleo Holm' indicated that wind measurements can also be influenced by flaring activities. This was determined by comparing wind measurements on the heli-deck with wind measurements from an arriving helicopter.

To prevent wind shielding, it is recommended that to install wind sensors at the highest possible location [100]. Additional wind tunnel tests could be used to determine the proper location of the wind sensor. Usually the wind speed is scaled to the reference height of 10 meters above the mean sea-level with a scaling law, such as given by OCIMF [43].

On fixed offshore installations wave conditions can be measured accurately with wave sensors. In ship-type structures the measurements of wave conditions is more difficult. Many systems have been developed to measure wave data from onboard. One type of systems determines the wave data from the relative wave elevation measurements onboard. Atwater [102] describes a system that uses this principle. The system measures the relative wave elevation at the bow by means of a pulsed laser wave height sensor and removes the vessel motions from this signal. Not the incident wave train is measured but the wave train that also contains wave diffraction and radiation. The system also measures the dynamic swell up due to the presence of the hull and the forward speed. Diffraction and dynamic swell-up are non-linear with the vessel speed and also vary with wave direction. This complicates the problem significantly. Atwater [102] investigates wave diffraction and radiation with model tests and corrects the measurements with them. Furthermore long waves are not registered correctly because the vessel tends to follow the wave nicely and no difference in relative wave elevation is registered.

The system described in [102] was tested, but tests were inconclusive because of a lack of ‘ground truth’, i.e., there was no indisputable source to compare wave data with.

A method to derive 2D wave spectra from the wave radars on a DP vessel is described by Waals and Pinkster. [103]. The method uses the measurements of 4 wave radars, which measure the relative wave elevation at a specific place. Using the maximum likelihood method the directional wave spectrum is derived from the measured relative wave elevations at all four locations. The application for this system is to apply it onboard a DP positioned shuttle tanker. The wave information is used as input for the feed forward system for the DP system so better can be anticipated against incoming waves. The system is under development but results indicate that the method is feasible.

Tucker and Pitt [37] discuss wave measurements by remote sensing. They conclude that this application improved, certainly for operational purposes, but is still associated with significant uncertainties. Grønlie [106, 107] discusses wave measurements by remote sensing. Two different classes of remote sensing exist, direct and indirect sensors. Direct sensors measure the quantities from which the wave data can be derived directly. Indirect sensors observe the surface waves via the interaction with another physical process, such as radar refraction. The relevant wave data is obtained through empirically determined calibration method. These methods work well under most circumstances, but may occasionally fail completely [106]. Grønlie concludes that for this reason it is impossible to quote reliable wave height performance figures valid for all conditions.

4.3 General Discussion for Fatigue Monitoring Systems

4.3.1 Purpose of Fatigue Monitoring

The purpose of a Fatigue Monitoring System (FMS) is to monitor the load accumulation in structural members in the hull. Furthermore, it needs to give insight in the reason why the load accumulation develops in the way it does. In this thesis, load accumulation in deck/bottom and side-shell longitudinals is studied.

The system can provide assistance for offshore Inspection, Maintenance and Repair (IMR) programs, and it can be used to support Life-Time Extension (LTE) programs during work at a yard. The FMS addresses loads and not the fatigue capacity of structural members. Therefore, tank inspections will be needed. The intension of the system is to provide guidance for inspections, but not to replace them.

The monitoring system onboard FPSO Glas Dowr is used as basis for the FMS development. This system was initially intended to gather data for the development and validation of the fatigue model as described in chapter 2 and 3.

4.3.2 Functional Requirements of Fatigue Monitoring System

The fatigue monitoring system (FMS) needs to be capable to continuously log the load in the side-shell, bottom and deck structure of an operating FPSO. In this thesis, a FPSO operating in a harsh environment, such as South-Africa and North-Sea conditions, is considered.

A continuous monitoring campaign onboard a FPSO is expensive. Not only there are the costs of the system itself and of the installation, the system also needs to be maintained and data needs to be post-processed on a regular basis.

Prior to analysing the data, the quality of the measurement data needs to be checked and erroneous measurement data needs to be discarded. Presently, it is not possible to fully automate the data qualification process and is presently done best by the human eye. In this aspect it is also advantageous to keep the amount of measured data limited.

The FMS needs to be practical from an operational point of view. The system console needs to be placed at a convenient location at the vessel and needs to be easy to operate. The sensors need to be easily accessible for inspection and, if needed, for maintenance and repair activities. Aspects related to the operational convenience of different sensors will be discussed in section 4.3.3. It is not necessary to review the measurement data in real-time to derive long-term load spectra. Therefore, data-processing need not be performed onboard, but can be performed at the office. However, it may be convenient for the crew to review vessel responses, for instance during weather sensitive operations.

4.3.3 Components of FMS

A FMS consists of a set of sensors, which feed their measured data to a data acquisition system. The acquisition system receives, stores the data and exports it to a different information carrier, such as a tape device or a DVD. Furthermore, the data acquisition system may perform some basic data processing and display system status and data.

The sensors can be connected to the data acquisition system through cabling and connection boxes, but also sensors exist with wireless connections to the storage computer. All sensors and connections need to be intrinsically safe when used in hazardous areas such as ballast tanks adjacent to cargo oil tanks. They must be placed such that they do not interfere with daily operational routines, and risk of damaging them is minimised.

The FMS that will be developed addresses loads and not the fatigue capacity of structural members. Therefore, the sensors are placed at so-called cold-spots, locations where the local stress geometry and welding don't influence the measurements. This makes it easier to interpret the measurements.

Sensors need to be operationally convenient. They need to be easily accessible for inspection and, if needed, maintenance and repair work. From up to down, the following sensors were found to be convenient to inconvenient during the measurement campaign at Glas Dowl:

- Motion sensors
- Long-based strain gauges (LBSGs) at deck
- Down looking radar on the side of the vessel
- Strain gauges in tanks
- Pressure gauges

Motion sensors can be installed at convenient locations. They are easily reachable and can easily be inspected and repaired if needed. The same holds for LBSGs, fitted at the deck to measure deck strains.

Down looking wave radars can be easily inspected, but operational experience with them showed high peaks in their measurements, which are caused by water spray on the sensor etc. Atwater [102] discussed similar difficulties with relative wave measurements using down looking radars. It may be possible to filter these peaks from the time-trace data.

Strain gauges have the disadvantage that, once failed, they can not be repaired. Consequently, they need not be inspected during service: they either work or they don't. Often, the average value starts to drift before failure of these sensors. In a practical FMS, these sensors could be used to derive a correlation between the measured strains and other measurements. With enough measurement data, the strain measurements are not needed anymore, and the strains can be predicted from these other measured responses. In such a measurement system, the strain gauges are allowed to fail after a time.

On Glas Dowlr, wave pressures, ballast pressures and cargo pressures are measured through pressure gauges. These sensors are fitted in the cargo and ballast tanks. They are drilled through the side-shell, and need proper sealing to prevent leakage. A disadvantage of these sensors is that once broken, they can not easily be repaired, particularly when they are located deep below the waterline. Inspection would require tank entrance, and consequently their inspection would require a lot of planning. Replacing broken sensor located below the MWL would require special arrangements. Consequently, these sensors are not practical from an operational point of view.

Tubby and Davenport [104] discuss the crackfirst sensor. A similar sensor, dubbed the fatigue damage sensor is described by Muragishi [105]. The sensors measure the Miner sum that the structure receives during its operational life. The sensor has a carefully made crack, which grows over time. The development of the crack is accurately known through fracture mechanics calculation. From the length of this crack, the amount of Miner sum that the structure has experienced, can be determined. This sensor measures the Miner sum and is still on the loading side, since the capacity of the structure itself is not measured. The application of this sensor has yet to be demonstrated in an offshore environment. The offshore application of the fatigue damage sensor described by Muragishi [105] will be investigated in the Monitas JIP [111].

The loading condition of the vessel is an important input parameter for fatigue damage accumulation. The loading conditions are continuously monitored onboard a FPSO. This data can relatively easily be stored for further analysis for fatigue onshore.

Wave data is another important parameter in the prediction of fatigue. Various possibilities are available to measure wave data. A method already discussed is to derive wave spectra through the measurements of relative wave elevation around the vessel. Another possibility is by deploying a wave rider buoy. During the measurement campaign at Glas Dowr at the Sable field, a wave rider buoy has been deployed that got lost quite a couple of times.

Possible reasons for loosing the buoy are that a vessel sails over it, adverse weather conditions or even sharks that nibble on the mooring. (The mooring line is made of rubber). The risk of loss makes that this not the preferred system to record wave data. It is also possible to measure the wave conditions with vessel-stationed radar systems.

Site-specific wave data can also be acquired though hindcast models. Over the years, these models have improved considerably, because more data becomes available to feed the hindcast models, but also because the models themselves are improved. The disadvantage is that wave spectra are specified in theoretical spectra and wave spreading information is lost. However, as was discussed earlier in section 2.2.1, it is also difficult to extract wave spreading information from wave rider buoy information.

Another parameter that can easily be monitored is the vessel compass heading. Any FPSO is equipped with a compass for operational purposes. Combined with the wave spectrum, it can be determined how the vessel was orientated in the waves during the measurements. As was seen in chapter 3, the vessel heading has an important influence on the long-term accumulated load.

4.3.4 Data Processing Techniques for FMSs

The lay-out of a FMS strongly depends on the processing of the measured data. In this thesis, three types of data processing are considered:

- Time-domain methods,
- Wave spectrum methods,
- Statistical response evaluation.

These post-processing methods are discussed separately.

4.4 Time Domain Methods

Response evaluation in time-domain derives the load accumulation data at an arbitrary point in the structure by direct time-trace manipulation of the measured signals. For instance, the stress time-series at a given hotspot can be calculated by the linear combination of the wave pressure, ballast pressure, Vertical Wave Bending Moment (VWBM) and Horizontal Wave Bending Moment (HWBM) time-series. The stress distribution and fatigue damage are derived from this stress time-series and the applicable SN curve.

This method is as closely as possible to reality, because the uncertainties in the calculation of these time-series are removed by directly measuring them. However, many sensors would be required in a system that exclusively uses this technique.

Even through direct measurements are used, uncertainties will remain. When measuring wave pressures, a structural model is needed to translate these measurements to stresses at the fatigue hotspot. When measuring strains, the stresses need to be determined from these strains with Hooke's law:

$$\sigma = E\varepsilon \quad (4.1)$$

in which E is the Young's modulus, σ is the stress and ε is the strain.

Hart and Rutherford [112] provide statistical data on construction steel. They discuss that the Young's modulus can be described by a normal distribution with a mean value and a standard deviation equal to 10% of the mean value. As an example, consider steel with a specified Young's modulus of $2.06 \cdot 10^6$ N/mm². When applying this normal distribution, 80% of the cases fall between $1.89 \cdot 10^6$ and $2.23 \cdot 10^6$ N/mm². This means that stresses derived from strains are within a band of 10% for 80% of the cases, and fatigue life is within a band of 25% for 80% of the cases. This shows that even when measuring loads or strains directly, uncertainties must be expected in the fatigue prediction. These uncertainties are 'before' considering the fatigue capacity.

4.5 Wave Spectrum Methods

Wave spectrum methods derive the stress time-series and fatigue statistics at the selected hotspot by applying the actual wave conditions and vessel conditions as input for the fatigue model. The fatigue model was previously described in chapter 2.

The wave spectra and loading condition need to be available as input for this system. Furthermore, the vessel orientation in the environment needs to be available. This vessel heading can be calculated, but measuring would remove additional uncertainties that are induced in the calculations.

Different methods to obtain wave data were previously discussed in section 4.2. They may be obtained through measuring them or through hindcasting. One other possibility is to derive the wave spectrum from recorded signals on the vessel. It is difficult to retrieve the full wave spectrum from narrow-banded responses, since the responses are induced by wave energy in a narrow frequency band that need not cover the entire frequency band range of the wave energy. This is particularly the case in wave conditions with low periods.

This is illustrated in figure 4.1 where a wave spectrum in a sea-state with a significant wave height of 4.0 m and mean zero upcrossing wave period of 7.0 seconds is shown (sea-state 1). A second wave spectrum with significant wave height of 4.0 m, and mean zero upcrossing wave period of 4.0 seconds is shown (sea-state 2). The wave spectra in both sea-states are described with a JONSWAP formulation with a peak factor of 3.3. Finally, the pitch RAO of Glas Dowl in headwaves is shown. The pitch spectra in sea-state 1 and 2 are shown in figure 4.2. They are calculated as:

$$S_{\theta}(\omega, \psi) = |\theta(\omega, \psi)|^2 S_{\zeta}(\omega) \quad (4.2)$$

where $S_{\theta}(\omega, \psi)$ is the pitch spectrum as function of the wave frequency ω , $\theta(\omega)$ is the pitch transfer function, ψ is the wave direction, and $S_{\zeta}(\omega)$ is the wave spectrum.

The waves in sea-state 1 have more energy in the frequency band where the vessel is sensitive to pitch motions than in sea-state 2. Consequently, the pitch response in sea-state 1 is higher than in sea-state 2.

The wave spectrum is calculated back from a known response spectrum and transfer function as:

$$S_{\zeta}(\omega, \psi) = \frac{S_R(\omega)}{|RAO(\omega, \psi)|^2} \quad (4.3)$$

For the high wave frequencies, where the RAO value is small and the response energy is small, the division of a number close to zero through a number close to zero will result in numerically unstable results.

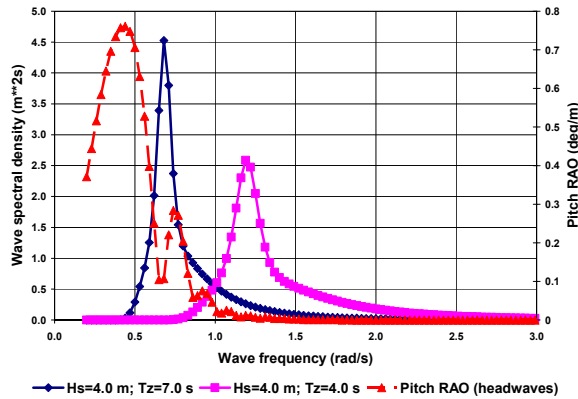


Figure 4.1 Wave spectra in day-to-day sea-state and pitch RAO

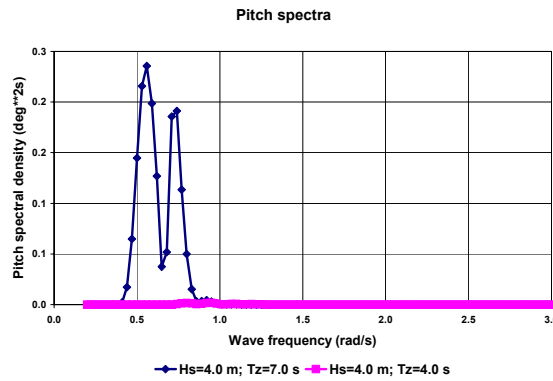


Figure 4.2 Pitch spectra in sea-state 1 and sea-state 2

4.6 Statistical Methods

The statistical methods aim at predicting the statistics of selected responses from statistics of measured responses. All responses are induced by the same wave conditions. All responses will be small in mild weather condition, where in storm conditions all responses will be large.

This implies that a long-term relation exists between different responses. If this long-term relation between different response statistics can be found, one response statistic can be predicted from a response statistic measured at a different location.

Statistical methods determine the long-term relation between input and target responses. With this relation, predictions of response statistics at other locations than at the measurement locations can be made.

The application of statistical methods is investigated in this section. First the nature of the long-term relation is investigated. Two calculation procedures are investigated to quantify the long-term relation between responses, the linear correlation method and neural networks. These methods are discussed and applied on a set of measurement data.

4.6.1 Statistical Correlation Method between Responses

The time record of the significant wave height and standard deviation of the wave pressure in one week are shown in figure 4.3. Both records comprise statistics of ½-hour time periods, which were measured during the measurement campaign at Glas Down the Durward & Dauntless field in the North Sea British sector. The wave data was measured with a wave rider buoy and the wave pressure was measured with a pressure gauge, fitted 2.8 m above the base at PS midship.

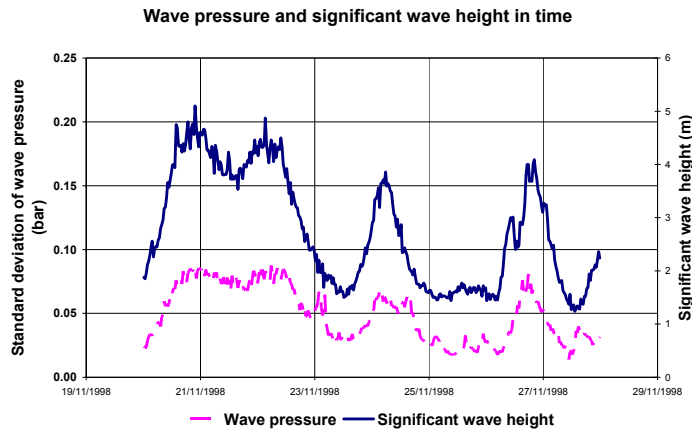


Figure 4.3 Significant wave height in time

The development of both records in time is similar. This is due to the fact that the recorded wave pressures are a direct result of the wave conditions. Consequently, both time registrations are correlated.

The accumulated wave loading per sea-state is calculated for a duration of 1800 seconds with the significant wave height as:

$$L_H = \left(3.11 \frac{H_S}{4}\right)^3 \frac{1800}{T_z} \quad (4.4)$$

in which H_S is the significant wave height and $T_{z,P}$ is the mean zero upcrossing period of the wave.

Similarly, the accumulated loading of the wave pressure loading per sea-state, L_P , is calculated as:

$$L_P = \left(3.11\sigma_p\right)^3 \frac{1800}{T_{z,P}} \quad (4.5)$$

in which σ_p is the standard deviation and $T_{z,P}$ is the mean zero upcrossing period of the wave pressure time-series.

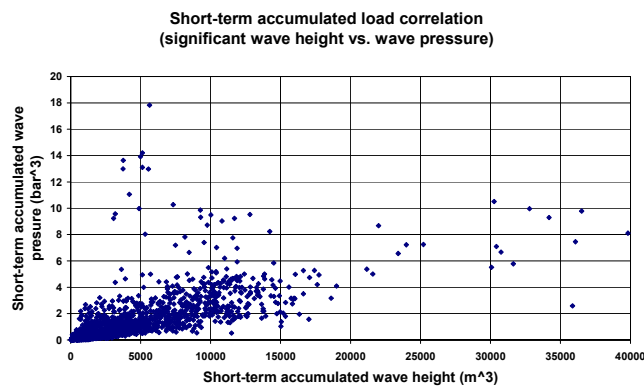


Figure 4.4 Standard deviation of wave pressures at frame 66.5 PS

The long-term accumulated loads are calculated as the sum of the short-term accumulated loads:

$$L_{LT} = \sum L_{ST} \quad (4.6)$$

Figure 4.4 shows L_H plotted against L_P for a period of 42 days. The figure shows a very scattered trend. The scatter is caused because the wave pressure depends on more parameters than on the wave height only. Other parameters are, for instance, the wave period, vessel draft, and the vessel heading relative to the sea.

The long-term accumulated loading of the significant wave height and the wave pressure are shown in figure 4.5. A relation between the long-term accumulated data of both measurements is observed. It appears that an average long-term relation between both parameters exists.

The time records of the measured pitch motion and wave pressure in the same week as in figure 4.3 interval are shown in figure 4.6. A similar development in time of the records is observed. This is due to the fact that both responses are induced by the same wave conditions.

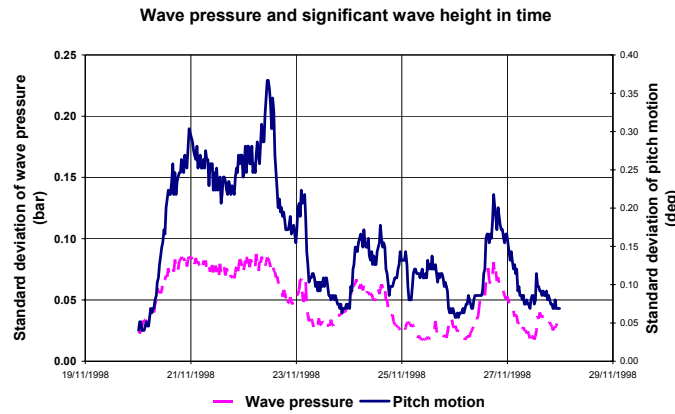


Figure 4.5 Short-term accumulated loading

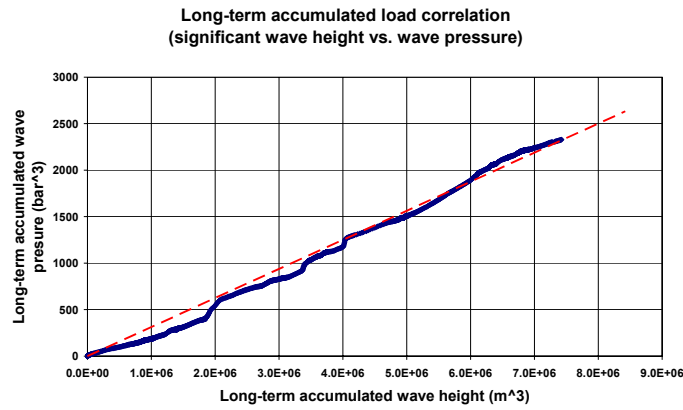


Figure 4.6 Long-term accumulated loading

The scatter plots of the short-term accumulated pitch motion and wave pressure are shown in figure 4.7. This plot comprises 42 days of data. The short-term relation between pitch and wave pressure shows more scatter than the plot between wave pressure and wave height. Pitch motions are mainly induced in a narrow frequency band of wave energy, where wave pressures are induced in all frequency bands. The fact that different responses react to different wave frequencies complicates the relation between the responses.

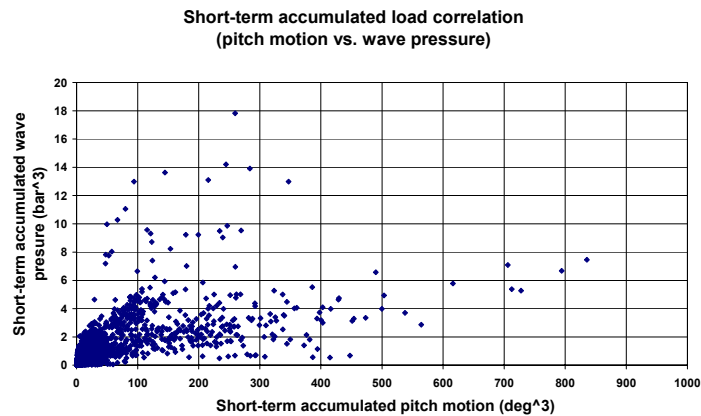


Figure 4.7 Short-term accumulated pitch and wave pressure data

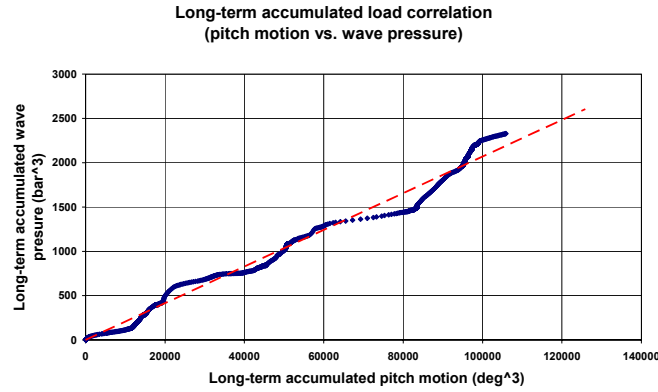


Figure 4.8 Long-term accumulated pitch and wave pressure data

The scatter plot of the long-term pitch and wave pressures is shown in figure 4.8. Although more scattered than the relation between wave height and wave pressure, an average long-term relation between both parameters can be observed.

The long-term relation gives an average relation between different responses. This relation is not analytical and needs to be determined by examining the responses of both signals. Responses that are physically closer related can be expected to give less scattered relations.

4.6.2 Linear Correlation Method

The method described in this section is denoted in this thesis as linear correlation method. In the method, the target response X_2 is calculated from the input response X_1 as:

$$X_2 = CX_1 \quad (4.7)$$

where C is an empirical constant. This correlation constant needs to be determined from a set of representative data with known X_1 and X_2 responses. C is determined as:

$$C = \frac{\sum (X_2)_t}{\sum (X_1)_t} \quad (4.8)$$

in which $(X_1)_t$ and $(X_2)_t$ are the responses in the training database with representative examples of responses X_1 and X_2 .

4.6.3 Neural Network Method

Neural networks provide a numerical method to derive complex relations between a set of known input and output data. This relation is trained from representative examples. If the network is trained adequately the output data can be calculated from the input data and the output data no longer needs to be measured. Neural networks have successfully been applied in a variety of areas, including monitoring applications [113].

This section only gives a brief overview of feed-forward neural networks. This review is based on the references [113-117]. Feed-forward neural networks are used, because this type of network is capable to describe the complex relation between responses in these types of applications. In this network, the information moves in only one direction, forward from the input nodes through the hidden nodes to the output nodes. There are no cycles or loops in this network. An example of a feed-forward neural network is shown in figure 4.9. The network consists of the following elements:

- Input data
- Neurons
- Connections between neurons
- Network output

The input data is introduced in the network through the input layer. The data is further transmitted in the network via connections from/to the neurons to the output layer, from which the network output is obtained. All these connections have their own weight. These neurons are organised in layers. The final layer is known as the output layer and all layers between the input layer and the output layer are known as hidden layers.

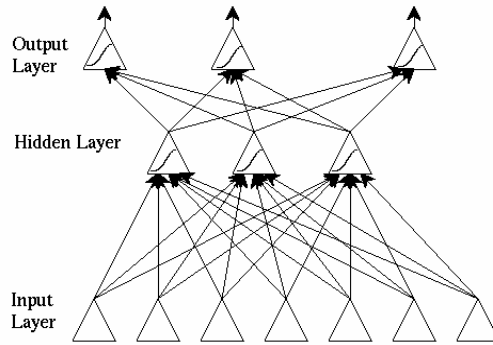


Figure 4.9 Example of Neural Network structure (cf. [114])

A neuron is the elementary element in a neural network. The neuron works as follows. It receives the numerical input values p_1, p_2, \dots, p_n from other neurons or from the input variables directly. All input connections have a weight w_i . Furthermore the neuron has a constant bias b . The numerical input of the neuron is calculated as the sum of the product of the weights and inputs:

$$i = \sum w_i p_i + b \quad (4.9)$$

In a neural network, an activation function or transfer function, f , is applied to obtain the output, a , of the neuron:

$$a = f(\mathbf{W}\mathbf{p} + b) \quad (4.10)$$

in which \mathbf{W} is the vector with weights and \mathbf{p} is the vector with input values. The output value of the neuron, a , is fed to the next neuron or is output of the network.

The (back-propagation) training algorithms require that the activation functions are continuous and differentiable. In this thesis, so-called sigmoid transfer functions in all hidden layers and the linear transfer function in the output layer are used. The log sigmoid transfer function is an activation function that scales the input value between zero and one. It has the following form:

$$y = \frac{1}{1 + e^{-x}} \quad (4.11)$$

The reason for using this transfer function is that it is capable of describing non-linear functions between input and output data.

The linear transfer function has as advantage that it can produce output between any limit.

The number of neurons in the network needs to be chosen by the user. With more neurons, the relation between input and output data can usually be better described. However, too many neurons will result in an ‘over learnt’ network. This is equivalent with the problem of over-fitting with polynomial functions; too many terms will result in unstable numerical behaviour. Too few neurons will result in a network that is not capable to adequately describe the relation between the input and output data. The choice of the number of hidden layers and neurons per hidden layer is arbitrary and the appropriate number needs to be determined on a trial-and-error basis.

Training of the network consists of choosing the weights and biases such that the input matches the output as closely as possible. In this thesis, the networks are trained with a so-called back propagation algorithm. In essence, a back propagation algorithm updates the weights and biases in the direction in which some chosen performance function decreases most rapidly.

In this thesis, the Levenberg-Marquardt back-propagation algorithm has been used, which is a common back-propagation algorithm that is suitable for the application. A set of known input and output data needs to be available. Per iteration a set of network weights and biases are calculated and the performance is judged from a performance function. Other functions are available, but in this case the mean square error (MSE) performance function is used [116]:

$$\varepsilon = \sqrt{\sum (t_i^2 - a_i^2)} \quad (4.12)$$

in which ε is the MSE, t_i is the target output and a_i is the network output of case i .

In the training algorithm, the MSE is minimised. The MSE performance function is a function in n -dimensional space. This performance function can have many local minimums but only one global minimum. Training algorithms will converge to a local minimum which need not be the global minimum. To overcome this problem to some degree, the dataset that is used to derive the correlations, is divided in a training set, a validation set and a test set. The set of updated weights and biases are calculated with the training set.

To keep the algorithm going in the right direction a second validation set is used. In case the error determined by this second data set starts to increase the training will be stopped. Because this validation set is effectively a part of the network training, it can not be used for the network testing. Therefore a third part of the test set is used to evaluate the performance of the network. This set of data is run through the network and the network output is compared with the target output.

4.6.4 Application of Linear Correlation Method

To illustrate the described methods and investigate the influence of relevant parameters, both post-processing methods have been applied on a set of measured data. The measurement dataset comprises 1996 ½-hour time records, measured during the monitoring campaign at Glas Dowl at the Durward & Dauntless field. Wave measurements were available during this period through a wave-rider buoy. The following responses are used: deck strain at midship PS, wave pressure at midship PS, 2.8 m above base, the pitch and the roll motion. The standard deviation, mean zero upcrossing period and short-term accumulated load of these measurements are used in this study. The draft at midship PS is determined with relative wave elevation measurements (downlooking radar) at that location.

The odd points in the dataset are used to determine the calibration constant for the linear correlation method, and the even points are used for testing. This ensures that the correlation coefficients are determined in a representative dataset.

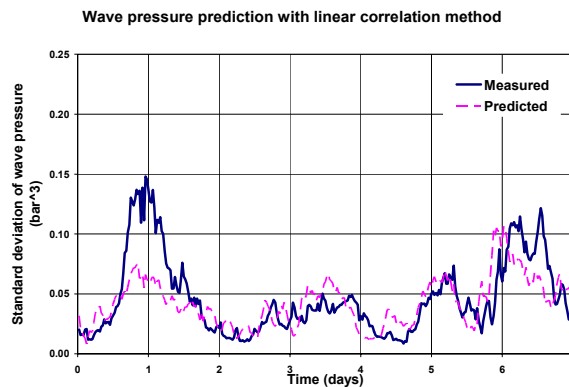


Figure 4.10 Simulated and predicted standard deviation of wave pressure

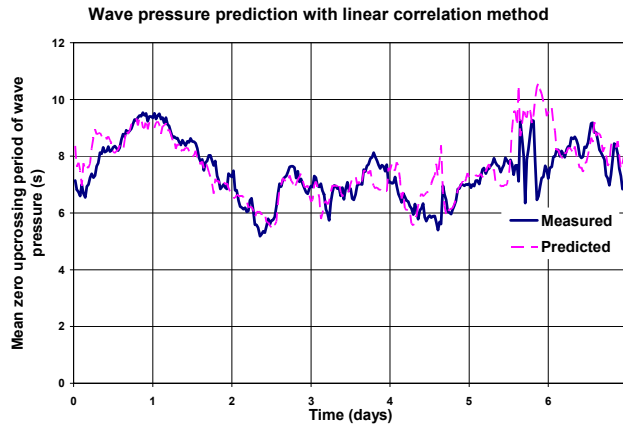


Figure 4.11 Simulated and predicted standard deviation of wave pressure

The standard deviation of the wave pressure that is calculated from the standard deviation of the deck strain is shown in figure 4.10. The plot also shows the measured standard deviation. The mean zero upcrossing period of the wave pressure as function of time is shown in figure 4.11. The predictions describe the long-term trends in the measurements reasonably. The differences between measurements and predictions are caused by the fact that the relation between input and target response is described by a linear relation, where this relation is not linear. Generally, the trend is predicted by the calculations, but the individual datapoints show spreading. This example shows that the method is not suitable for response predictions in individual sea-states.

The measured and calculated long-term distribution of the standard deviation are shown in figure 4.12 and the distributions of the mean zero upcrossing period of the wave pressure are shown in figure 4.13. The long-term distributions are represented well by the calculations. Since fatigue damage is accumulated through the sea-states, the long-term distribution is of interest rather than the responses in individual sea-states. This makes that the method applicable for fatigue analysis purposes.

The predicted and measured long-term accumulated wave pressure as function of time are shown in figure 4.14. The long-term accumulated load is calculated as the sum of the short-term accumulated loads. On the long term, a reasonable agreement between measurements and predictions is observed. In some periods the agreement between measurements and calculations is less well. These differences are particularly visible for high responses.

The differences are caused by the fact that the method uses an average relation, where the correlation between both responses is more complex in nature. For instance, the magnitude of the responses also depends on the wave period. In sea-states with different wave periods the ratio between the responses will be different. Furthermore, vessel draft and wave direction are important relations that are not explicitly taken into account in the model. Furthermore, differences between measurements and predictions are magnified because the load accumulation is proportional to the third power of the load.

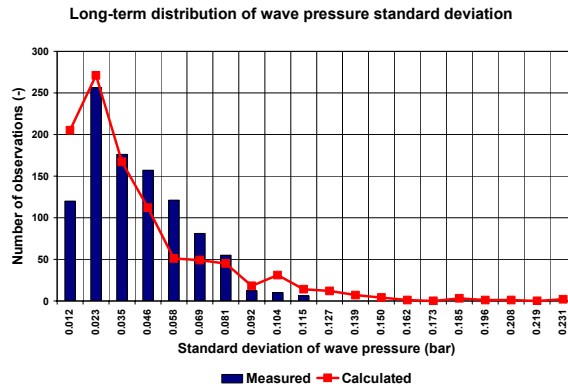


Figure 4.12 Long-term distribution of wave pressure standard deviation

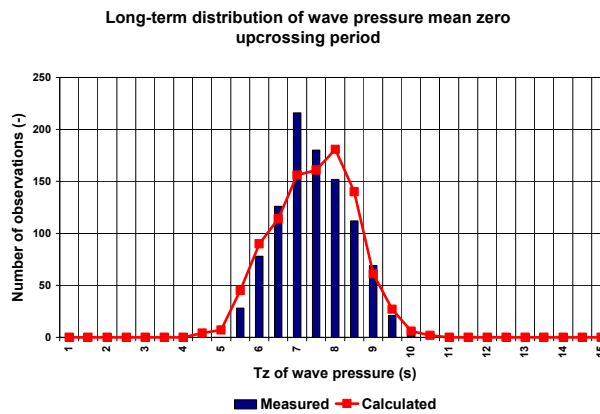


Figure 4.13 Long-term distribution of wave pressure mean zero upcrossing period

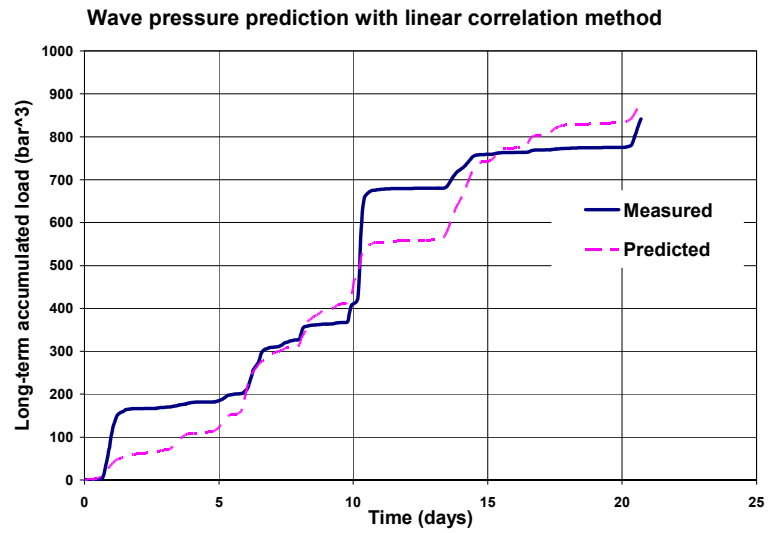


Figure 4.14 Long-term accumulated wave pressure with linear correlation method

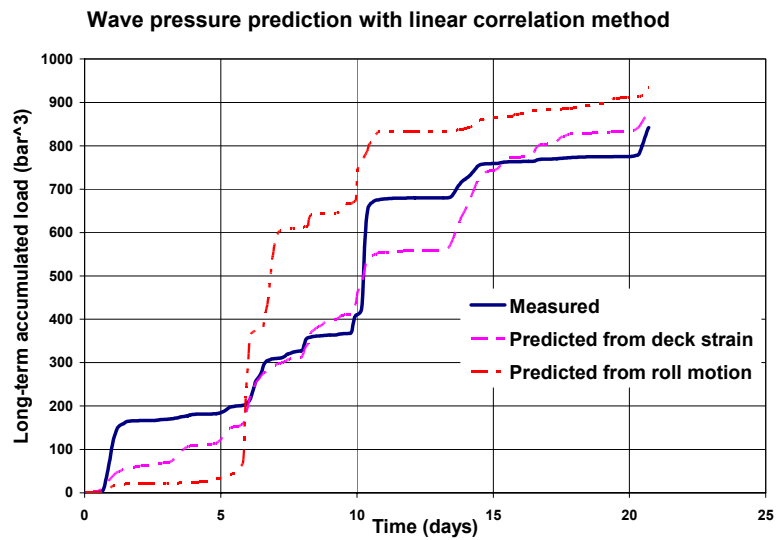


Figure 4.15 Long-term wave pressure predictions from different responses

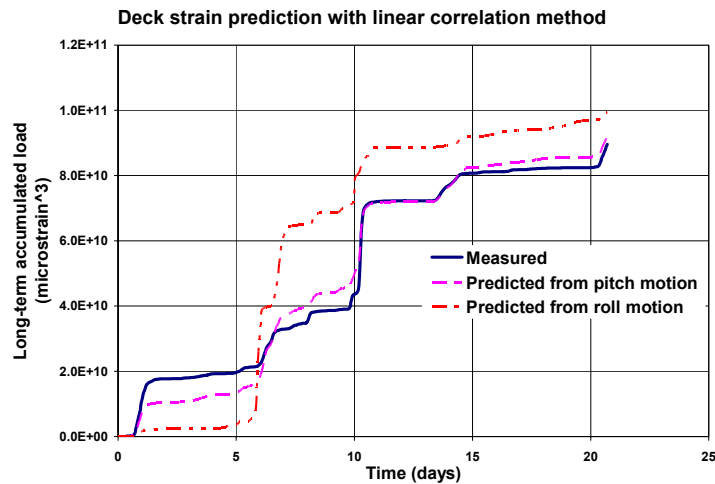


Figure 4.16 Long-term deck strain predictions from different responses

The long-term accumulated wave pressure that is predicted from the measured deck strains and from the measured roll motions is shown in figure 4.16. The predictions from the deck strain show better agreement with the measurements than the predictions from the roll motion. The wave pressure is physically more related to the wave bending moment than to the roll motion of the vessel. Therefore, the long-term relation between wave pressure and deck strain is better defined than the relation between wave pressure and roll.

This is also observed in figure 4.16 where the measured long-term accumulated deck strain is shown, and its prediction from the pitch and roll motion. The pitch motion and the deck strain are physically more related than the deck strain and the roll motion. This makes that the prediction from the pitch motion is better than the prediction from the roll motion.

This shows that it is important to consider which signals will be used for the prediction of other responses. It is best to predict responses from responses that are physically closely related.

In the previous calculations, the odd datapoints were used as training dataset to determine the calibration constants, and the even points were used for predictions. In this way, a representative training environment was created. Below, the performance of the method when determining the calibration constant from a non-representative dataset is investigated.

The distribution of the significant wave height in the test set and in the test set when using the first half of the data for training and the second half for simulations are shown in figure 4.17. There is a significant difference between both distributions. The average significant wave height in the training-set is 3.1 m and the average significant wave height in the test set 2.4 m. This difference is so large because the period in the database only covers 41 days. This is not a sufficiently long period to obtain statistically representative distributions.

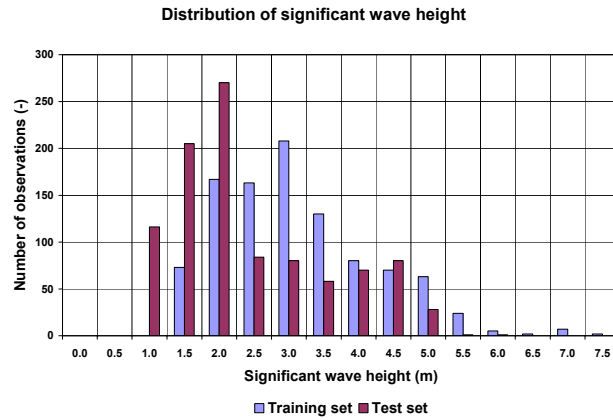


Figure 4.17 Distribution of significant wave height in training and test set

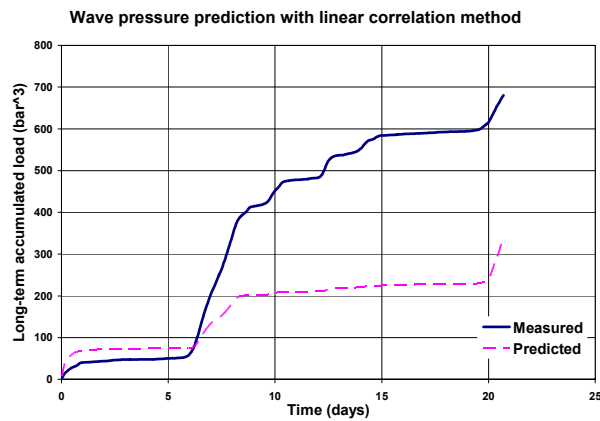


Figure 4.18 Long-term wave pressure prediction with non-representative training set

The predicted long-term accumulated wave pressure from the deck strain measurements are shown in figure 4.18. The calculations don't match well with the measurements. When considering the long-term deck strains that are predicted from the pitch motion in figure 4.19, the match is better, which is due to the fact that these responses are physically closer related.

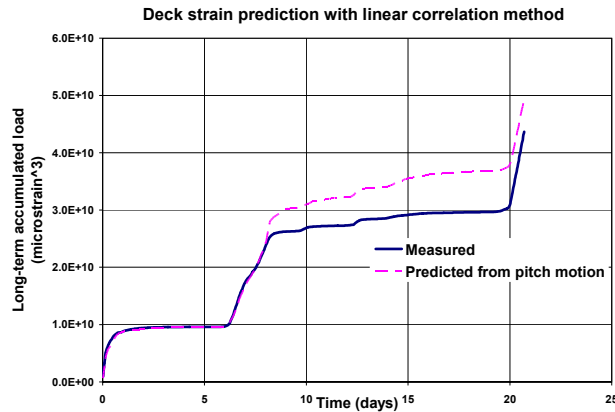


Figure 4.19 Long-term accumulated deck strain with non-representative training set

The linear correlation method performs better in a non-representative training-set when using input and target responses that are physically closer related. In the (hypothetical) case that a linear relation (with zero offset) between input and target response exists, the linear correlation method will find the exact relation between target and input response, regardless of the test-set that is used and the method will produce the exact target data.

4.6.5 Application of the Neural Network Method

In relation to the linear correlation methodology, a neural network is more flexible, because it can describe non-linear relations between input and target responses. Furthermore, a number of responses can be fed into the network to predict the target response.

Below, the application of a feed-forward neural network is investigated. The neural network consists of one hidden sigmoid layer and one linear output layer. Such a network is capable to determine the relation between measured responses.

The hidden layer contains 10 neurons, and the output layer contains 1 neuron. The choice of the number of neurons is arbitrary, but, as will be illustrated later in this section, the sensitivity of the results to the number of neurons was found to be small.

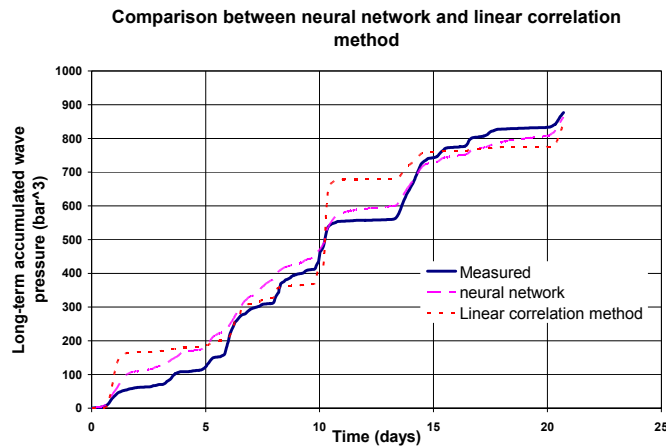


Figure 4.20 Performance of neural network and linear correlation method

The same data set as used for the linear correlation method is used here. Half of the dataset is used to train the network and the other half is used to make the calculations. The even points are used for the simulations. The odd points are used for training. Two-third of this dataset is used for network training and 1/3 is used for network validation.

The measured and predicted long-term accumulated wave pressures are shown in figure 4.20. The predictions are made with the short-term accumulated deck strain measurements. The calculation results with the linear correlation method are also included in the plot. The results of the neural network match closer to the predictions than the linear correlation method.

The predicted and measured long-term accumulated wave pressures are shown in figure 4.21. The predictions are made for three cases: (i) input data is short-term accumulated deck strain, (ii) input data is short-term accumulated deck strain and mean zero upcrossing period of deck strains, and (iii) input data is short-term accumulated deck strain, mean zero upcrossing period of deck strain and vessel draft. Including more measurements in the prediction does not significantly affect the prediction in this case.

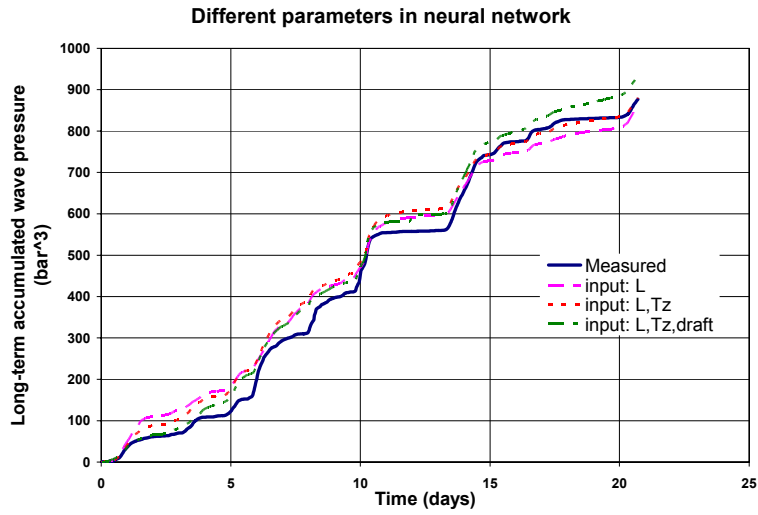


Figure 4.21 Neural network performance for different input sets

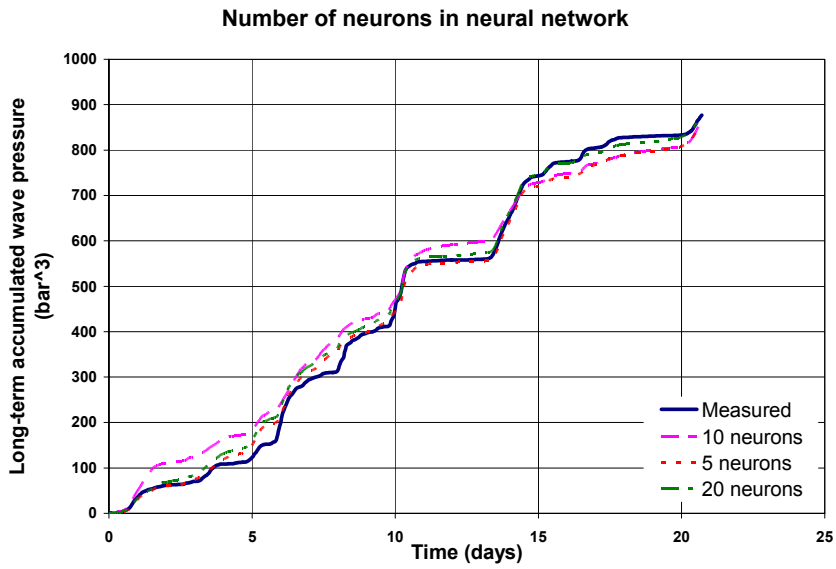


Figure 4.22 Neural network performance for different neurons

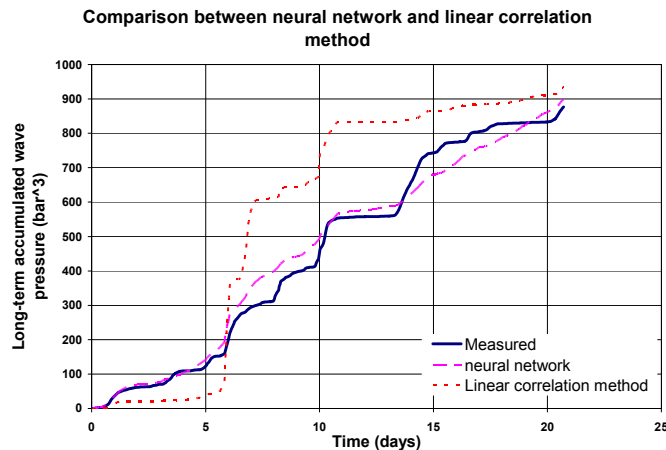


Figure 4.23 Method performances for physically non-related responses

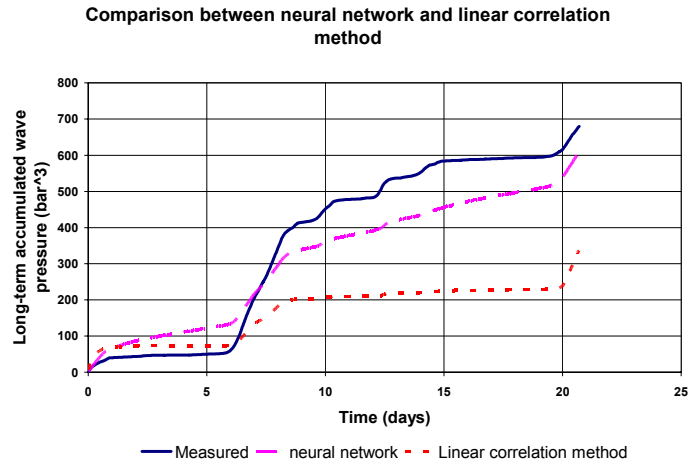
The predicted long-term accumulated wave pressure for networks with 5, 10 and 20 neurons are shown in figure 4.22. Although some differences are visible, the results are not sensitive to the choice of the number of neurons.

The long-term accumulated wave pressure when predicted from the short-term accumulated roll motions of the vessel are shown in figure 4.23. The measured data and the predictions with the linear correlation method are also shown. The roll motion and wave pressure are physically not strongly related. The predictions with the neural network are better than the linear correlation method predictions, but it is better to use responses that are physically closer related.

The separation in the dataset is such that the training data is representative for the test set. As was discussed earlier, the dataset is not representative when using the first half of the data for network training and the second part for network testing, see figure 4.17. Below, the performance of neural networks is investigated when using this training dataset. The network is trained with the first 2/3 part of the training set and validated with the last 1/3 part.

The measured and predicted long-term accumulated wave pressure are shown in figure 4.24. The accumulated load is simulated with short-term accumulated deck strain data. Furthermore, the results of the linear correlation method are shown. The performance of the neural network is better than the performance of the linear correlation method, but considerable differences between measurements and predictions are observed.

The performance of the neural network is better than the performance of the linear correlation method, since the relation between input and target response is better described.



Figurer 4.24 Method performances when using a non-representative training set

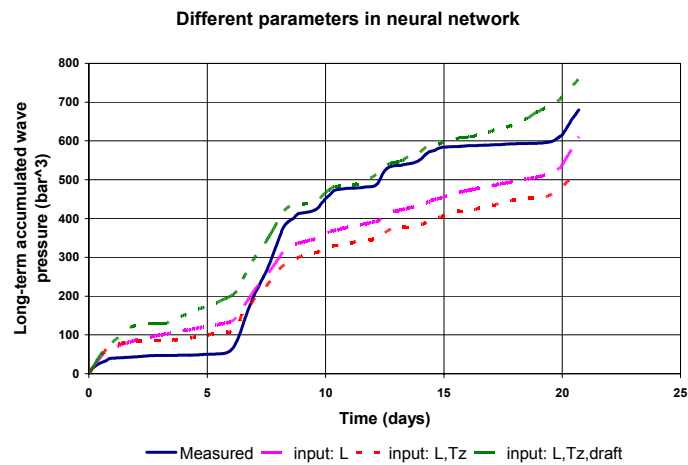


Figure 4.25 Network performance when using a non-representative training set and different input variables

The measured and predicted long-term wave pressure when also the mean zero upcrossing period of the deck strains and the vessel draft are used for the prediction are shown in figure 4.25. The predictions that include the mean zero upcrossing period are not better than when using only the accumulated deck strain data only. When also including vessel draft data, the predictions improve. This shows that the choice of the signals as input for the network are important.

4.7 Summary of Results

In the previous sections, the application of the linear correlation method and neural networks to predict target responses from measured responses has been discussed. Their applications have been tested on a set of measured data.

All responses are induced by the same wave conditions. This implies that a long-term relation between responses exists, in storm conditions all responses will be high where in mild sea-states all responses will be low. The linear correlation method and the neural network method predict this long-term relationship from a set of input and target data. This calculation technique is not suitable to apply to individual sea-states.

Both methods were found to provide satisfactory results when the input and target responses are physically related and a representative training set is used to determine the relation between input and output responses.

The performance of the methods deteriorates when physically less correlated responses are used. For instance, the pitch motion is physically more related to deck strains than the roll motion. The performance of the methods when predicting deck strain is better when using pitch motions than when using roll motions as input.

The training dataset needs to be sufficiently representative. Neural networks were found to deal better with non-representative training sets, because the relation between input and output can be better described than in the linear correlation method. Furthermore, the physically closer the responses are correlated, the less the output results will be affected by the selection of the training dataset. In the special case that the method describes the exact relation between input and target responses, the representativeness of the training dataset would not be important.

The neural network showed a better performance than the linear correlation method. Particularly when using physically non-related responses and when using a training dataset that is not representative, the neural network is superior to the linear correlation method. This is due to the fact that the relation between input and target response can only be represented by a linear relation in the linear correlation method, where a neural network is capable to describe a complex relation between input and target response.

Multiple responses can be fed into a neural network to predict the target response. The linear correlation method is capable to predict the target response from only one response. This makes the neural network more flexible in use than the linear correlation method.

Only the neural network methodology will be considered in the remainder of this thesis.

5 Application of Fatigue Model and Fatigue Monitoring System

In this chapter, a case study is described to demonstrate the fatigue prediction methodology and the fatigue monitoring system. First, long-term load calculations are made with the calculation procedure that is described in chapter 2. These calculations are compared with measurements at the Glas Dowr. After that, the methodology to determine correlations between different vessel responses is applied. These correlations are determined both from measured example data and from calculated example data.

5.1 The Fatigue Monitoring System and Structural Integrity management

As discussed in chapter 1, structural integrity comprises the capability of the unit to perform its function during its life. Structural integrity needs to be considered during design and maintained throughout the life of the unit. For fatigue this means that an accurate fatigue assessment needs to be made during the design, with a valid fatigue model, and that the fatigue capacity needs to be checked during operations of the vessel, by means of tank inspections.

A long-term fatigue model was developed and validated against available full-scale measurement data and model-test data in chapter 2. In chapter 3, the influences of various parameters on the long-term were investigated and it was found that representative input data, such as environmental data or loading condition data, is equally important as a correct model for accurate long-term fatigue calculations. However, the actual wave conditions and loading conditions that the vessel will encounter during its operational life are most likely different from the design wave conditions. Given the sensitivity of accumulated loading, it is advantageous to check calculated load distributions in design with a monitoring system. This removes considerable uncertainty in the long-term load distribution.

In chapter 4, techniques were investigated to post-process and interpret the measured response data. In particular, the application of neural networks to determine relations between responses was investigated, since this technique potentially provides a practical monitoring system with a limited amount of required sensors.

The fatigue calculation procedure in design and the fatigue monitoring system are complementary; the interpretation of the measurements follows from the fatigue model, and the calculated long-term response statistics can be checked with the help of the measurements of the fatigue monitoring system.

How the fatigue monitoring system fits in the integrity management of the vessel is shown in figure 5.1. The following actions (in the grey boxes) are anticipated:

- Calculate fatigue life of the identified structural members and calculate long-term response statistics of monitored responses
- Measure the responses during operations of the vessel
- Post-process the recorded response data in a meaningful format, to compare measured long-term response statistics with anticipated response statistics in design.

During design, fatigue calculations will be made at identified hotspot locations in the vessel, with an adequate model, using the best input data available. Simultaneously, long-term response calculations will be made at the sensor locations. These sensors will typically be placed at so called cold-spot locations. These are locations where representative responses are measured, and where the measurements are not influenced by local stress raisers in the structure.

The responses at the monitoring locations will be logged continuously and these measured responses will be statistically analysed. The comparison of the measured long-term distributions at the sensor locations with the calculations made during design gives a good indication if the long-term load statistics were correctly estimated in design.

A comparison between anticipated and measured loads at the coldspot locations is provided by this analysis. However, a comparison of response data at the hotspot locations is needed as well. Measured data at the sensor locations need to be translated to response data at these hotspot locations. This is done with the methodology described in chapter 4.

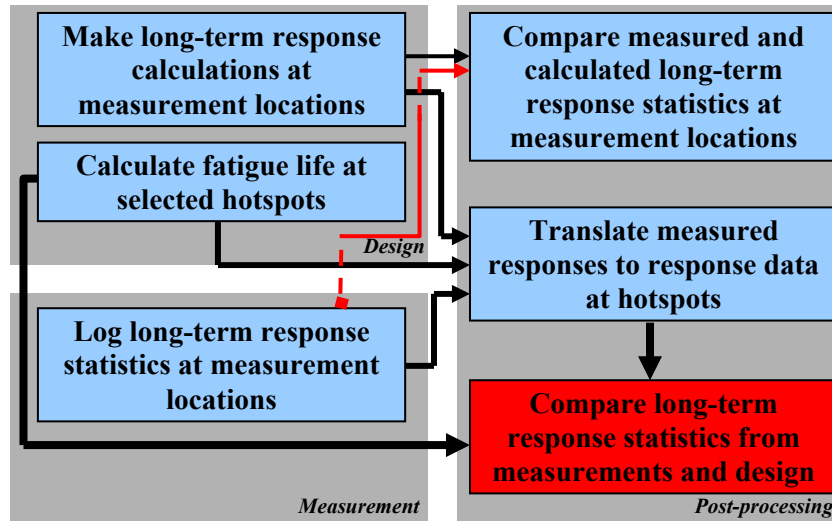


Figure 5.1 Structural integrity management and monitoring

5.2 Set-Up of Case Study

A case study is performed to investigate the use of the fatigue calculation procedure in combination with the Fatigue Monitoring System (FMS). The Glas Dowr operating at the Durward & Dauntless field on the UKCS has been used in this case study. This field has been selected because a significant amount of measurement data is available at this field, together with a detailed set of environmental data. The Durward & Dauntless can be classified as a 'harsh environment' field.

First, long-term load calculations of monitored responses are described and the calculated long-term response distributions at the sensor locations are compared with the measured response distributions. In section 5.4, the correlations between the monitored responses are investigated. The long-term relations between the the statistics of the monitored responses are determined from the calculated responses in the sea-states and applied to measured response data.

5.3 Long-term Load Calculations

5.3.1 Environmental Data and Loading Conditions

Five loading conditions that range from ballast load to full-load are taken into account in the calculations. These loading conditions are specified in appendix A.

Hindcasted wind, wave, current and swell data are available at the nearby Ross & Parry field for a period of 5 years. This data comprises the significant wave height, mean zero upcrossing period and direction of wind waves and swell, wind speed and direction and current speed and direction. These statistics are specified for periods of 3 hours. The recorded responses with the monitoring system were measured in a different period than covered in the environmental dataset. The wind wave and swell spectra are modelled with a JONSWAP wave spectrum. For wind waves, an average gamma value of 1.5 is given, where for swell an average gamma value of 4.0 is used.

5.3.2 Measured Response Data

The long-term response calculations are made for the wave pressures at the sensors P1 and P3 and for the deck strain at sensor L1. The location of these sensors are shown in figure 5.2 and the sensor locations are listed in appendix B. Wave pressure sensor P3 is located deep below the mean waterline where intermittent wetting does not occur. Sensor P1 is located above the mean waterline in ballast condition, and below the mean waterline in full-load condition. The sensors L1, P1 and P3 are situated near midship (frame 66.5) at PS.

The measurement data-set contains approximately 18,000 ½-hour measurement periods. This data has been measured over the period of 1997-1999. The data has visually been reviewed and erroneous data was discarded from the database. This was done by visually reviewing the data and by comparing the measured response data with recorded response data at other sensors. To illustrate this data review process, the standard deviation of the deck strains measured at Long-Based Strain Gauge (LBSG) L1 and LBSG L2 are shown in figure 5.3. L2 is situated at the same location as L1 but on the SB side of the vessel. Some measurement data at L1 is obviously erroneous measurement data and doesn't match with measurements at SB side of the vessel. The selected datapoints for the analysis are shown in figure 5.4. In this data-set, response statistics at PS and SB side show a similar development in time.

This left a data-set with 11,060 datapoints for L1, 12,775 datapoints for L3, 16,259 datapoints for P1, 16,423 datapoints for P3, 16,396 datapoints for P19 and 16,492 datapoints for P21. The dataset is not continuous over time. The mean values, standard deviation and mean zero upcrossing period are used in this case study. Wave data with the wave rider buoy is unavailable for a large period of the time.

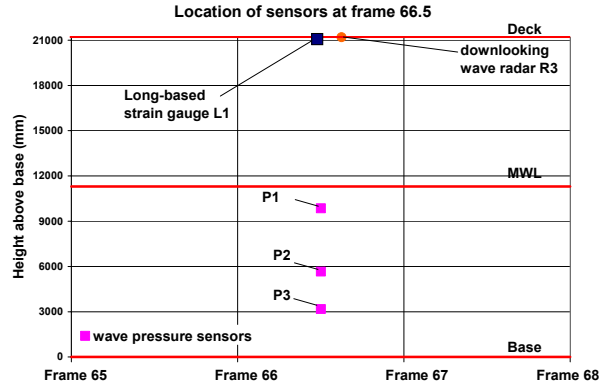


Figure 5.2 Locations of measurement sensors at frame 66.5 (near midship)

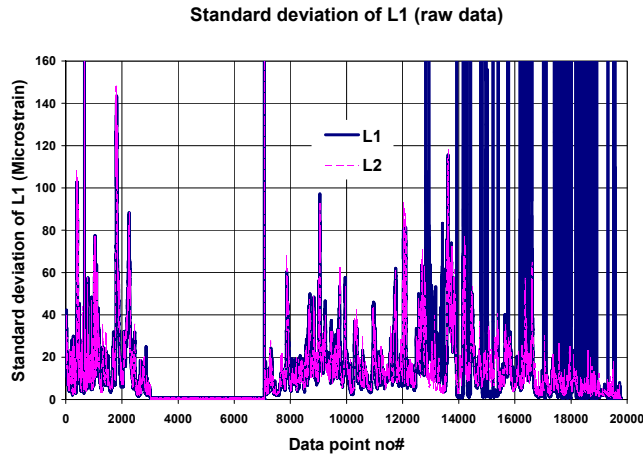


Figure 5.3 Response statistics before review

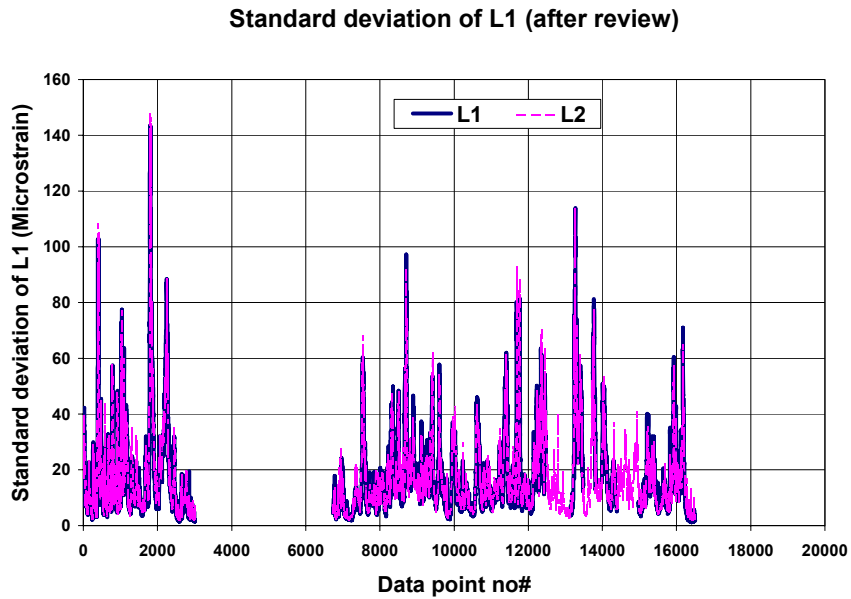


Figure 5.4 Response statistics after review

5.3.3 Calculation Procedure

The following calculation procedure is used:

- Evaluate the average vessel heading in every sea-state and loading condition
- Evaluate short-term response distribution in every sea-state, loading condition and selected location
- Determine long-term accumulated load and long-term response distributions per selected location

The vessel heading in a given sea-state and loading condition is evaluated with the procedure described in section 2.4. The average vessel orientation in wind waves and swell is calculated with this procedure per sea-state and for every loading condition.

With these calculated vessel headings, the responses per loading condition and sea-state due to wind waves and swell are calculated with the model described in chapter 2. It was discussed in section 3.4 that the full physics of the non-linear roll damping need not be addressed in the long-term assessment. Therefore, the calculations are made for a rollamp value of 3 degrees. It was demonstrated in section 3.1.4 that the sea-states can be modelled with short time-series. In these calculations, the sea-states are modelled with time-series of 200 seconds. Wave spreading is modelled in the wind wave spectra with a \cos^2 spreading function, and swell spectra are modelled as long-crested waves, which is a common assumption in design practice. Wave spreading information is specified in the hindcasted wave data.

The significant response amplitude distribution and the mean zero upcrossing period distribution are displayed. The significant (single) amplitude, $A_{1/3}$, is calculated from the standard deviation of the time-series as:

$$A_{1/3} = 2\sigma_R \quad (5.1)$$

where σ_R is the standard deviation of the response.

The short-term accumulated load, L_{st} , is calculated from the standard deviation and mean zero upcrossing period of the response as:

$$L_{st} = (3.11\sigma_R)^3 \frac{T}{T_z} \quad (5.2)$$

in which T is the duration of the sea-state (3 hour) and T_z is the mean zero upcrossing period of the response.

The long-term accumulated load is the summation of the short-term accumulated loads in the individual sea-states:

$$L_{lt} = \sum L_{st} \quad (5.3)$$

The long-term accumulated load is weighted over the occurrences of the loading conditions.

5.3.4 Calculated Vessel Heading

The calculated relative wind wave direction as function of the significant wave height of the wind waves is shown in figure 5.5. The relative swell direction is shown as function of the significant wave height of the swell in figure 5.6. The same coordinate system as was adapted in section 2.4 is used here. The data in these graphs represents the intermediate loading condition 3, which is a regularly occurring loading condition where the draft of the vessel is 11.42 m.

The vessel tends to head into the wind waves rather than into the swell. When the significant wave height of the wind waves exceeds 2 meters, the relative wave direction is not more than 30 degrees off headwaves in these calculations.

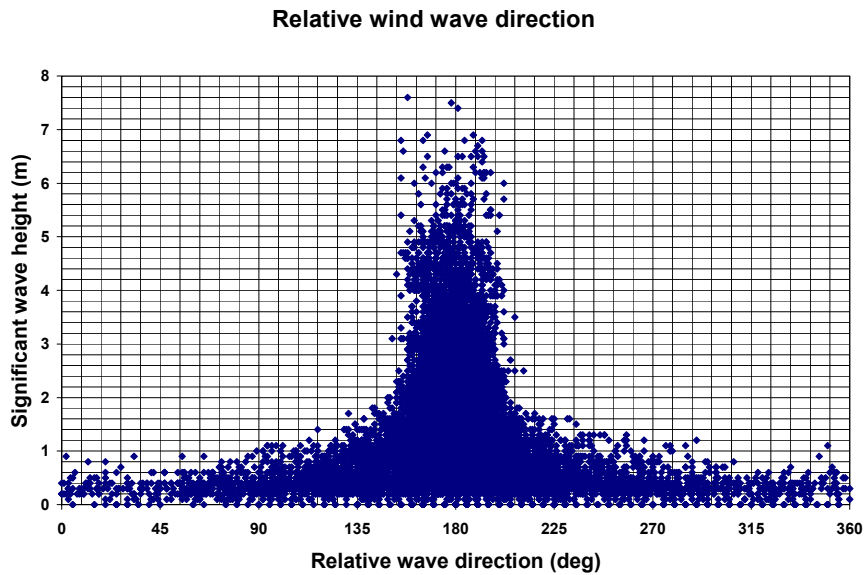


Figure 5.5 Relative wind wave direction

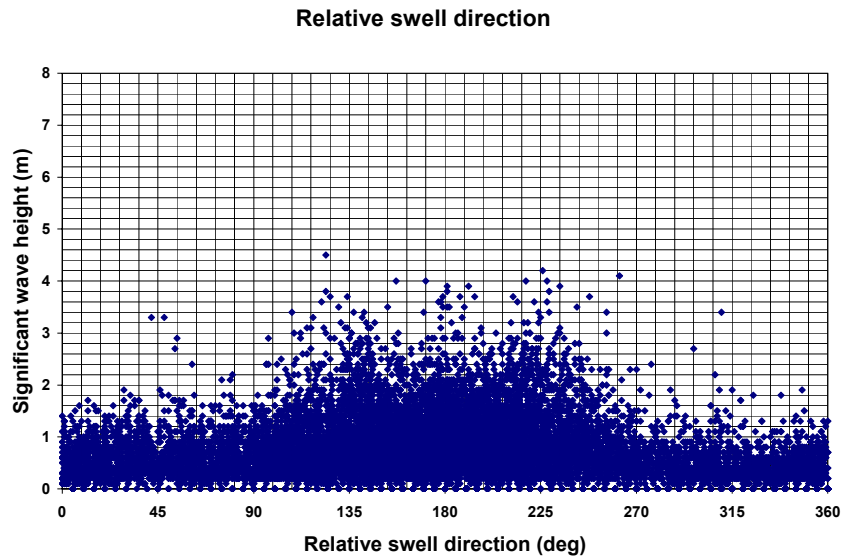


Figure 5.6 Relative swell direction

5.3.5 Comparison of Measured and Calculated Response Statistics

The measured and calculated long-term distributions of the significant deck strain amplitude at sensor L1 are shown in figure 5.7. A fair comparison between measurements and calculations is found. Averagely, the mean zero upcrossing period is calculated higher than the measured values.

The calculated and measured long-term accumulated deck strains are shown in figure 5.8. The first bar is the measured value and the second bar is the calculated value when weighted over the occurrences of the loading conditions. The last five bars are the long-term accumulated load per loading condition when they occur 100% of the time. L1 is the ballast condition, L5 is the full-load condition, and the others are intermediate loading conditions with increasing midship draft. The long-term accumulated loads are presented in percentages. The 100% case is the measured long-term accumulated load. A fair agreement between measurements and calculations is observed and it can also be observed that the deck strains are not sensitive to the loading condition.

The comparison for the wave pressure measurements at P3 is shown in figure 5.9. This sensor is located far below the mean waterline where no intermittent wetting occurs. A fair agreement between measured and calculated amplitude distribution is shown in figure 5.9. The average mean zero upcrossing period of the wave pressure from calculations is lower than from measurements.

The measured and calculated long-term accumulated wave pressure at pressure sensor P3 are shown in figure 5.10. The calculations overestimate the measurements value by a factor of 1.6. The long-term accumulated wave pressure depends heavily on the loading conditions and the occurrence thereof. This is due to the fact that the amplitude of the wave pressure is a function of the distance below the mean waterline.

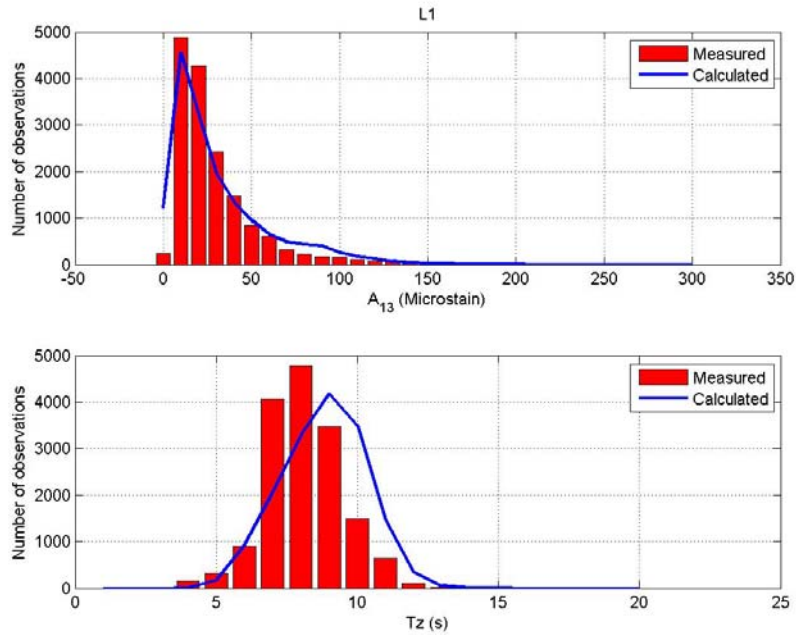


Figure 5.7 Measured and calculated long-term distributions at deck strain sensor L1

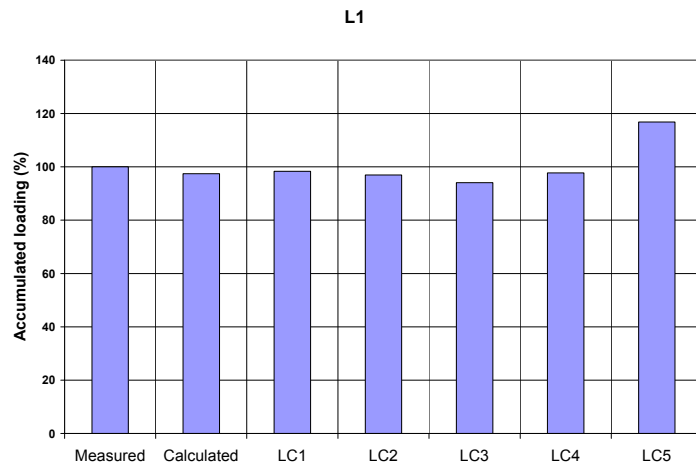


Figure 5.8 Measured and calculated long-term accumulated load at deck strain sensor L1

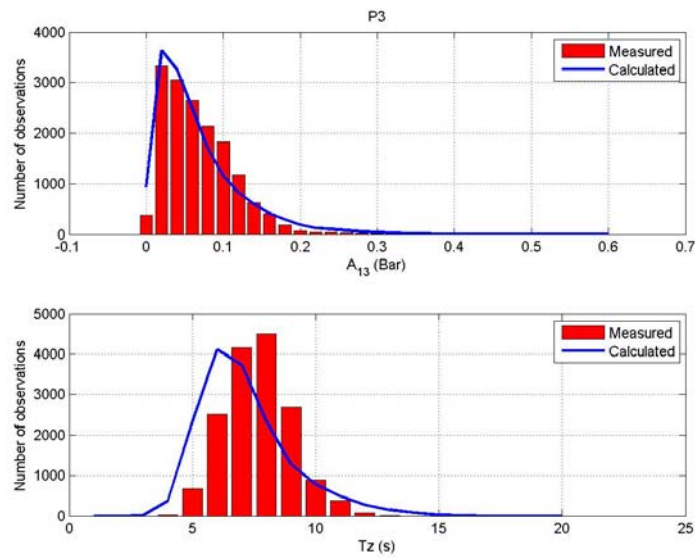


Figure 5.9 Measured and calculated long-term distributions at wave pressure sensor P3

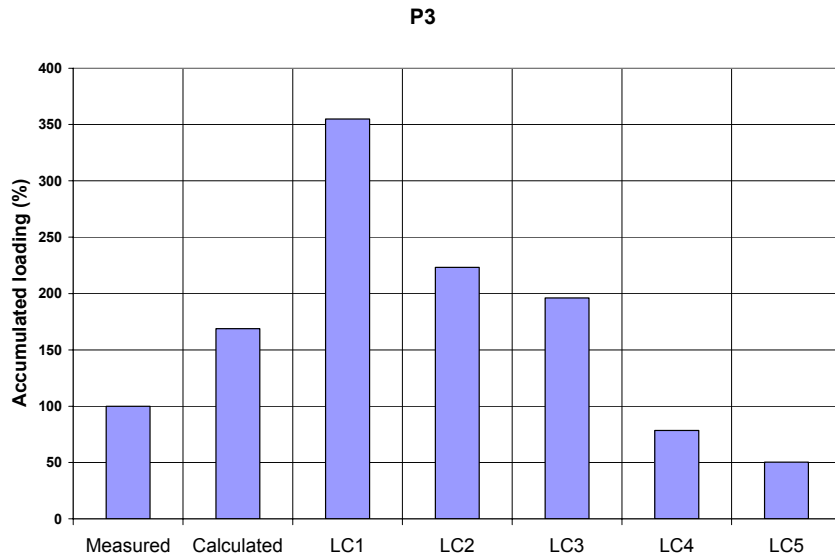


Figure 5.10 Measured and calculated long-term accumulated load at wave pressure sensor P3

The measured and calculated significant amplitude and mean zero upcrossing period distribution of the wave pressure at sensor P1 is shown in figure 5.11. This sensor is situated above the mean waterline in LC1 and LC2, and below the mean waterline in the other loading conditions. Intermittent wetting effects occur at this sensor. A fair agreement between measured and calculated amplitude distribution is observed. The averagely predicted wave pressure is smaller than the averagely measured period.

The measured and predicted long-term accumulated wave pressure at wave pressure sensor P1 are shown in figure 5.12. The calculations over-estimate the long-term accumulated wave pressure with a factor 1.2. The loading condition has a significant influence on the wave pressure at this location. The accumulated wave pressure is small in loading conditions where P1 is situated above the mean waterline.

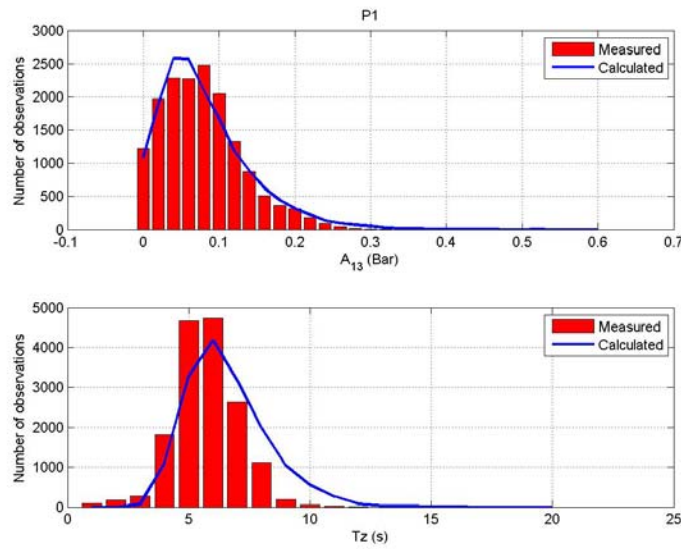


Figure 5.11 Measured and calculated long-term distributions at wave pressure sensor P1

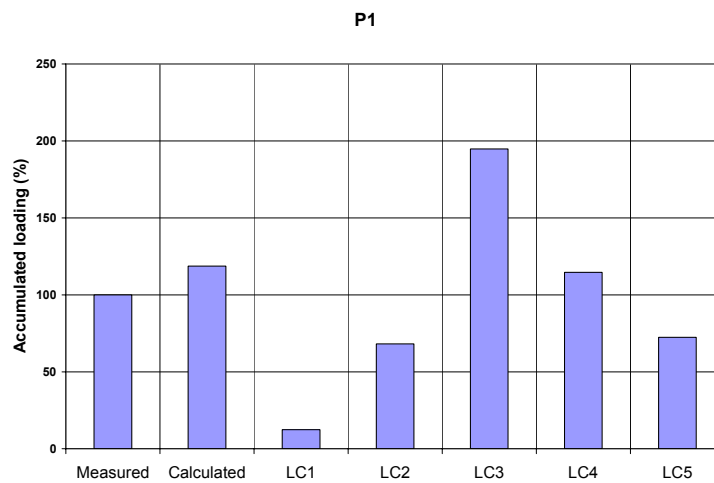


Figure 5.12 Measured and calculated long-term accumulated load at wave pressure sensor P1

5.3.6 Discussion of Comparison measurement vs. calculations

The measured significant amplitude distributions were predicted better by the calculations than the mean zero upcrossing period distributions. Generally, it is more difficult to accurately predict periods than response amplitudes. This is due to the fact that apart from the area below the response spectrum, also the tail of the response spectrum needs to be predicted well. This can be seen as follows. The significant response amplitude is calculated from the response spectrum as:

$$A_{1/3} = 2\sigma_R = 2\sqrt{m_0} \quad (5.4)$$

where m_0 is the zero-order spectral moment, calculated as:

$$m_0 = \int_0^{\infty} S_R(\omega) d\omega \quad (5.5)$$

where ω is the wave frequency and S_R is the response spectrum.

The mean zero upcrossing period, T_z , is calculated from the response spectrum as:

$$T_z = 2\pi \sqrt{\frac{m_0}{m_2}} \quad (5.6)$$

where m_2 is the second-order spectral moment, calculated as:

$$m_2 = \int_0^{\infty} \omega^2 S_R(\omega) d\omega \quad (5.7)$$

This formulation shows that m_2 is more sensitive to higher wave frequencies than m_0 and to accurately predict m_2 the tail with high wave frequencies also needs to be predicted accurately to get an accurate number of cycles. Theoretical wave spectra have a smooth tail, ensuring more or less smooth tails in the calculated response spectra, where in reality these tails need not be smooth.

The calculated long-term response distributions compare reasonably well with the calculations. Nevertheless, significant differences may exist between measured and calculated long-term accumulated load. This is due to this third-power influence and inherent to fatigue assessments. Consider that the slope of the SN curve has a constant value of three. Then, the fatigue damage due to a load cycle is proportional to the third power of this load and proportional to the occurring amount of load cycles. This makes the long-term accumulated load very sensitive to the calculation input data.

The wave pressures are more sensitive to the actual loading conditions than the deck strains. Consequently, more uncertainty in long-term accumulated wave pressure than in long-term accumulated deck strain from loading conditions can be expected.

5.4 Correlation between Response Statistics

In this section, the capability of the neural network method to describe the long-term relation between responses is investigated. These relations are determined from the calculated response statistics in section 5.3 and the determined long-term relations are applied on the measured data.

5.4.1 Measured Response Data

The deck strain measurements at L1 and L3 and the wave pressure measurements at sensors P1, P3, P19 and P21 are used in this study. The locations of these sensors are given in appendix B. The locations of sensors L1, P1 and P3 were previously shown in figure 5.2; the locations of the sensors L3, P19 and P21 are shown in figure 5.13. Sensors L1, P1 and P3 are situated at PS near midship. Sensor P3 is located far below the surface where intermittent wetting effects do not occur.

The location of wave pressure sensor P1 depends on the loading condition; in ballast condition the sensor is located above the mean waterline and in full-load conditions below the mean waterline. Significant intermittent wetting occur at this location.

Deck strain and wave pressure measurements at L3, P19 and P21 are included to investigate the performance of the technique when applied to different sections where the local draft can be different due to trim of the vessel. The location of P19 relative to the mean waterline depends on the draft of the vessel and significant intermittent wetting occurs at this pressure sensor. Pressure sensor P21 is located far below the surface, where intermittent wetting does not occur.

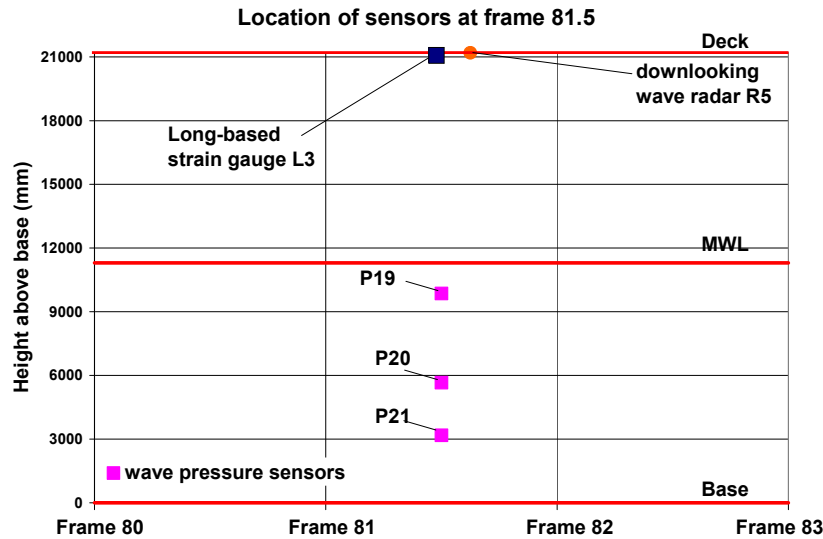


Figure 5.13 Locations of measurement sensors at frame 81.5 (near $\frac{3}{4}$ Lpp)

The same data-set with measured responses that was used in the section 5.3 is used in this study. The used measurement statistics are the standard deviation, mean zero upcrossing period and average values.

5.4.2 Calculation Procedure

The long-term relation between input and target response statistics is determined per loading condition with a feed-forward neural network. As in chapter 4, this network contains 1 layer with 5 sigmoid neurons, and a linear output layer with 1 neuron. The networks are trained with the Levenberg-Marquardt back-propagation algorithm, which is a standard back-propagation algorithm for network training.

The relations between the responses are trained with the calculated response data with the developed long-term fatigue model. One year of calculated response data is used to train the network. The first half part of the data is used for training the network, the following $\frac{1}{4}$ part is used for validation and the last $\frac{1}{2}$ -part for testing. The test set is used to visually check that the networks are properly trained.

Measured response statistics are fed into the trained network to simulate the target response statistics. The target response is predicted for all five loading conditions and the response is linearly interpolated to the correct vessel draft. The vessel draft in the sea-state, T , is calculated from the average wave pressure at sensor P3, p_3 , as:

$$T = z_0 + \frac{p_3 - p_0}{\rho g} \quad (5.10)$$

in which p_0 is the atmospheric wave pressure (1 bar), ρ is the density of seawater (1.025 t/m^3) and z_0 is the height of the pressure sensor above base (2.757 m).

The neural network is used to predict the standard deviation and the mean zero upcrossing period of the response. The short-term accumulated load, L_{st} , is calculated as:

$$L_{st} = (3.11\sigma_R)^3 \frac{T}{T_z} \quad (5.11)$$

in which σ_R is the standard deviation of the response, T is the duration of the sea-state (1/2-hour) and T_z is the mean zero upcrossing period of the response.

The long-term accumulated load, L_{lt} , is the summation of the short-term accumulated loads:

$$L_{lt} = \sum L_{st} \quad (5.12)$$

Table 5.1 shows the cases that are evaluated in this comparison. Trim and draft are not specifically used as parameters in the network, since separate networks are calculated for separate loading conditions. The effect of the local draft is incorporated by interpolating the calculated responses with the different networks to the actual (local) vessel draft.

Case no#	Input data	Output data
1	L1	L3
2	L1	P3
3	L1	P1
4	P3	P1
5	P3	P21
6	P3	P19
7	L1	P21

Table 5.1 Input cases for comparison

5.4.3 Calculation Results

The simulated and measured short-term accumulated in deck strain L3 (case 1) are shown in figure 5.14 for a period of 100 days. To make the plot more clear, the short-term accumulated loads are raised to the power $1/3$. The measured and simulated long-term accumulated deck strains are plotted in figure 5.15. The simulations are made with deck strain measurements at sensor L1 as input.

The simulated and measured statistics follow a similar trend in time. Differences between measurements and simulations are visible in individual sea-states and sometimes these differences are large. This is due to the fact that the network describes an average relation between input and target responses. The actual realisation in a sea-state may be higher or lower than described by the network. Furthermore, it can be observed that the network tends to underestimate the large accumulated loads. However, the differences between the measured and calculated long-term accumulated loads remain within 10%. This is due to the fact that the bulk of the load accumulation is induced in sea-states with moderate responses that occur regularly (see figure 3.21). Because the sea-states in which large load accumulations are induced occur relatively rare, their contribution on the long-term load accumulation remains limited.

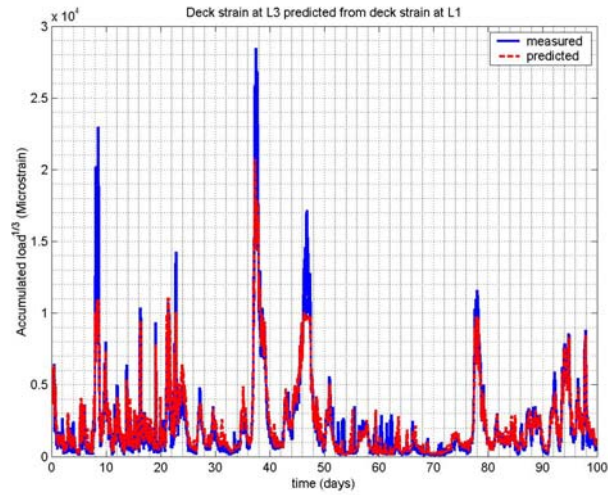


Figure 5.14 Measured and predicted deck strain statistics at deck strain sensor L3

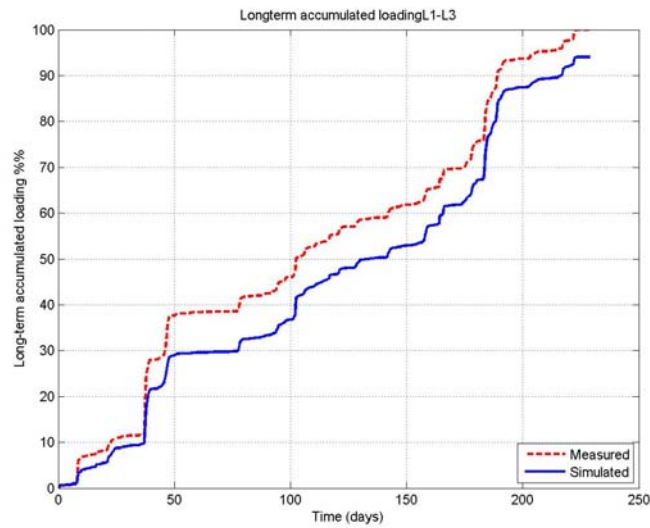


Figure 5.15 Predicted and measured long-term accumulated deck strain at sensor L3

The simulated and measured accumulated wave pressures at sensor P3 (case 2) are shown in figure 5.16. The data in this plot is raised to the third power to make the picture clearer. The predictions are made with deck strain measurements at sensor L1 as input.

The simulated and measured accumulated loads follow a similar trend in time, but can be significantly different in individual sea-states. This is due to the fact that wave bending moment and wave pressure are weakly correlated. For example, little wave bending moment response is induced in small and short waves, where many wave pressure cycles are encountered at the side-shell. Furthermore, the deck strains are less sensitive to the local vessel draft than wave pressures.

The measured and simulated long-term accumulated wave pressures are plotted in figure 5.17. In general, a good agreement between predictions and measurements is observed, but in events with high load accumulation, significant differences are visible. The difference between measurements and calculations is less 10% in these calculations.

The long-term accumulated wave pressure at sensor P1, predicted from deck strain sensor L1 (case 3) are shown in figure 5.18. In comparison with the longterm relation between L1 and P3, the long-term relation between L1 and P1 is more complicated, because, depending on the loading condition, sensor P1 is located above or below the mean waterline. This makes that the local draft is an important parameter for the prediction of the wave pressures at P1, where the deck strains are relatively insensitive to the local draft. Despite these differences, a fair agreement between predictions and measurements is found, the difference between measurements and calculations is smaller than 12%.

The predicted wave pressure at P1 from the predicted wave pressure at P3 (case 4) is shown in figure 5.19. Wave pressure measurements at P1 and P3 are physically closer related than the deck strain at L1 and the wave pressure at P1, because they are both sensitive to the local draft. Depending on the loading condition, sensor P1 is located above or below the mean waterline, and sensor P3 is always below the mean waterline. This complicates the relation between the the wave pressures measured at P1 and P3. The difference between measured and calculated long-term accumulated loads is less 15%. When comparing figure 5.18 and 5.19, the predictions with wave pressure responses at P3 are in general better than the predictions with the deck strains at L1, except in two events with large load accumulation (around day 50 and day 250).

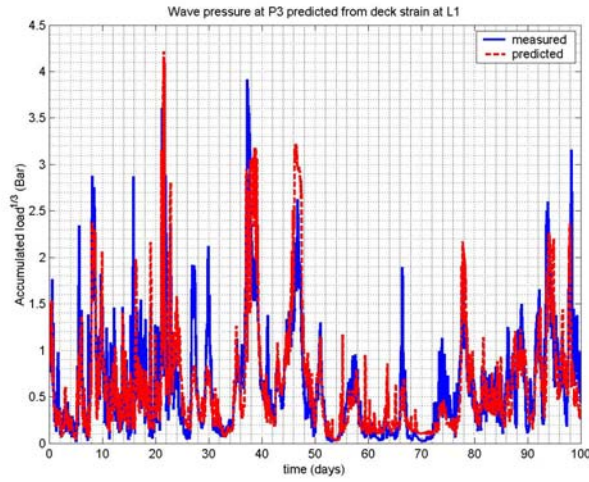


Figure 5.16 Measured and predicted deck strain statistics at wave pressure sensor P3

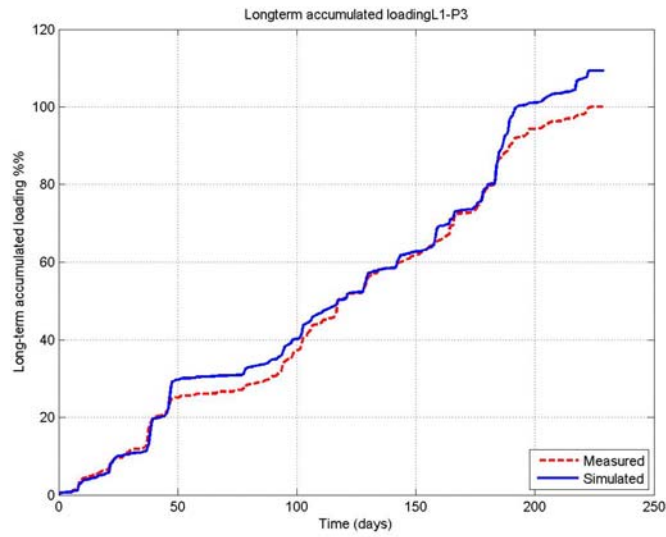


Figure 5.17 Predicted and measured long-term accumulated wave pressure at sensor P3

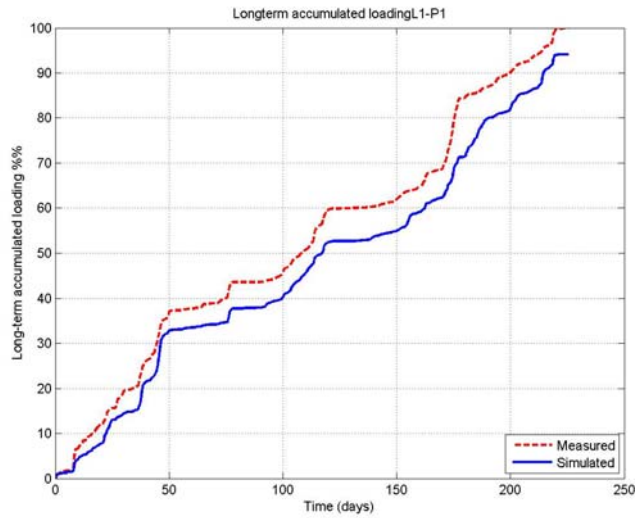


Figure 5.18 Predicted and measured long-term accumulated wave pressure at sensor P1 from deck strain sensor L1

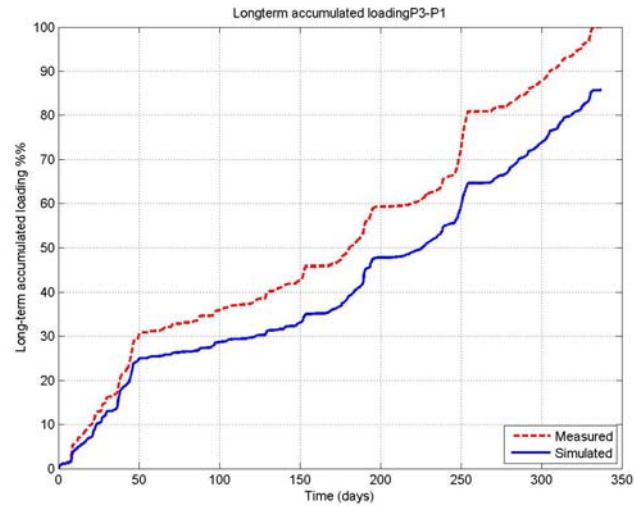


Figure 5.19 Predicted and measured long-term accumulated wave pressure at sensor P1 from wave pressure sensor P3

The measured and simulated wave pressure measurements at sensor P21 (case 5) are shown in figure 5.20. The simulations are made with wave pressure statistics recorded at sensor P3. Since the sensors P3 and P21 are located at different sections, the local draft can be different and the trim of the vessel is an additional parameter that complicates the long-term relation between the pressure statistics at both locations. The networks are trained for 5 loading conditions with given draft and trim, but in reality a range of vessel trims can occur with a given draft. This is visible in the results; starting from approximately day 60, the calculations appear to systematically over-predict the measurements. The difference between measurements and calculations is less than 23%.

The simulated and measured long-term accumulated pressure at sensor P19 (case 6) are shown in figure 5.21. The predictions are made with the wave pressure measurements at sensor P3. Depending on the loading condition, the sensor P19 can be located above or below the mean waterline. This further complicates the relation between pressures at P3 and P19, because the local draft is an important parameter for the prediction of P19. Because the sensors P3 and P19 are situated at two different sections, the local draft at both sections needs to be described with two parameters (trim and draft). This is reflected in the results. For instance, the trend of the measured long-term accumulated load between day 50 and 100 is different than that of the calculated long-term accumulated load in figure 5.21. This is not the case in figure 5.19 where the long-term accumulated wave pressure at sensor P1 is predicted from pressure responses at P3. The difference between the predicted and measured long-term accumulated wave pressure at sensor P19 is less than 15%.

The measured and simulated long-term accumulated wave pressure at sensor P21, predicted from deck strain measurements at L1, vessel draft and trim (case 7) are shown in figure 5.22. The local draft is not an important parameter for the deck strains, but it is for the prediction of the wave pressure at sensor P21. The local draft at section 81.5 is determined by both the vessel draft and the trim of the vessel, which makes the relation between the deck strain at L1 and the wave pressure responses at P21 more complicated than the relation between deck strain at L1 and wave pressure responses at P3. This is visible in the results; the agreement of the trend between predictions and measurements is better in figure 5.18, where the measured and calculated accumulated wave pressure at sensor P3 are shown, than in figure 5.22, where the measured and predicted long-term accumulated wave pressure at sensor P21 are shown. The simulated accumulated load is predicted within 25% of the measured accumulated load.

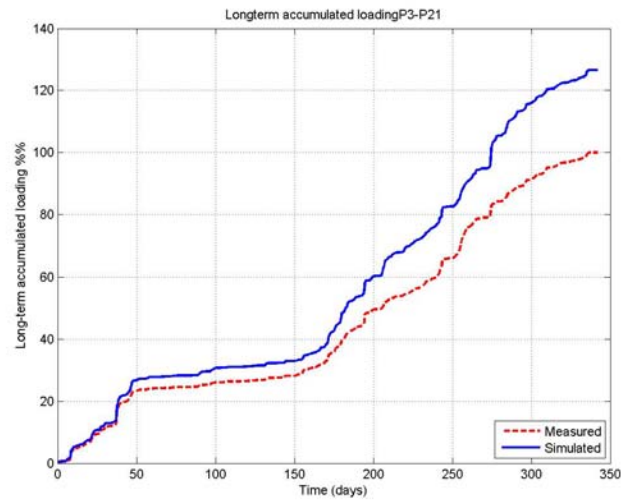


Figure 5.20 Predicted and measured long-term accumulated wave pressure at sensor P21 from wave pressure sensor P3

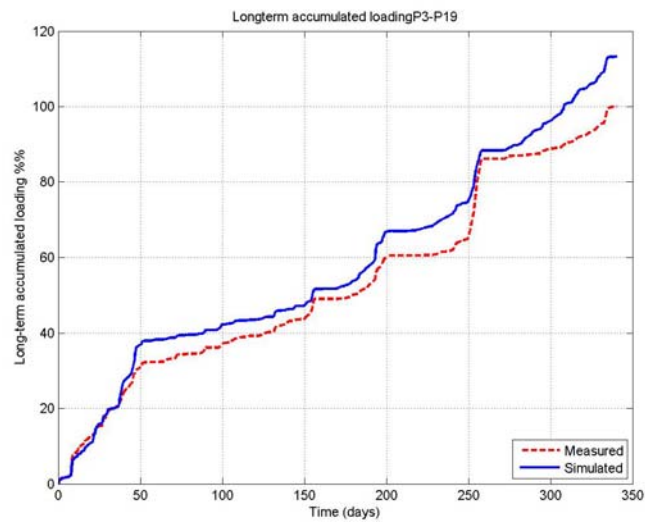


Figure 5.21 Predicted and measured long-term accumulated wave pressure at sensor P19 from wave pressure sensor P3

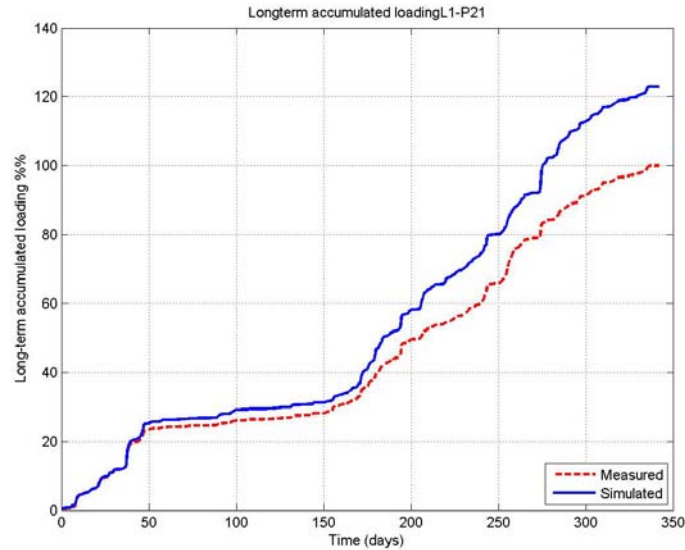


Figure 5.22 Predicted and measured long-term accumulated wave pressure at sensor P21 from deck strain sensor L1

5.4.4 Summary of Results

The simulations in this section show the capability of the methodology to predict response statistics from response measurements at different locations. The long-term relations between different response statistics can be derived from data that is calculated with the fatigue calculation procedure that is described in the chapters 2 and 3.

Depending on the combination of input and target responses, the differences between the measured and calculated long-term accumulated loads were within 10-25% in the presented calculations. It was found that the methodology performs best if the relation between input and target response is influenced by a limited number of parameters and if the input and target responses are physically closely related.

6 Conclusions and Recommendations

6.1 Conclusions

The following conclusions are made in relation to the developed and validated long-term fatigue model in the chapters 2 and 3.

- Representative environmental data and loading condition data are equally important for an accurate fatigue assessment as a physically correct model.
- The wave pressure and vertical wave bending moment contribute most to the load accumulation and fatigue damage in the side-shell/bottom and deck longitudinals. Although the contribution of cargo pressures and the horizontal wave bending moment on the long-term stress accumulation and fatigue damage are small in magnitude, they should be taken into account.
- The intermittent wetting effect around the mean waterline has an important contribution in the fatigue damage and can not be neglected in the fatigue analysis.
- The phase relations between the wave pressure, the vertical wave bending moment, the horizontal wave bending moment and the cargo pressures need to be taken into account in an accurate fatigue calculation.
- A procedure for the calculation of the fatigue life of deck, side-shell and bottom longitudinals was developed in time-domain. Because many sea-states need to be considered in the fatigue analysis, the sea-states can be modelled with short time-series. This saves considerable amount of computational time and makes fatigue calculations in time-domain feasible.
- A fair agreement between measured and calculated long-term response statistics distributions was found. Wave pressure statistics are sensitive to the loading conditions and deck strains are less sensitive to the loading conditions.

The following conclusions are made regarding the investigated post-processing techniques for a fatigue monitoring system:

- The uncertainty in the long-term load distributions that the vessel experiences at the field can be reduced significantly by measuring them. This measured data can provide valuable information to support tank inspections and work at a yard.
- Because all responses are induced by the same wave conditions, long-term relations exist between them. These long-term relations can be described with a neural network.
- The neural network can be trained with measured data and with calculated data. Both data-sources provided a fair indication of accumulated response at target locations.
- The capability of the neural network to predict the target response from an input response increases when the target and input responses are physically closer correlated. Furthermore, the more representative the training data-set becomes for the target data-set, the better the performance of the method.

6.2 Recommendations

The following recommendations are made:

- A large part of the uncertainty in load accumulation is caused by the fact that the input data (environmental data, loading condition data) for the fatigue assessment in design is based on historical data, and will be different than in reality. It is recommended to store data, such as loading condition data or vessel heading data on a continuous basis, because this data is monitored for operational purposes on the FPSO. Furthermore, wave conditions can be retrieved fairly easily through hindcasting afterwards. Logging and collecting these data and redoing the assessment with these updated data could already reduce the uncertainties in the loads considerably.
- In this thesis, a methodology has been developed to predict response statistics at different locations from measured response statistics. This methodology can be used as basis for a monitoring system. The specification of this monitoring system needs to be further developed.

- Fatigue design as part of integrity management involves the entire life of the unit, from design throughout operation. Fatigue design and fatigue monitoring are complementary and not separate issues, as it is treated now mainly. Calculations are needed for the understanding of the measurements and putting the consequences of the measurements into practical measures. On the other hand, monitoring information provides feedback to the design calculations, to determine whether load regimes are as anticipated in the design calculations. This synergy between a fatigue model that is supported by measurements from a monitoring system can provide valuable information to support inspection, maintenance and repair work and conversion work at a yard. At the moment, this is not common practice yet. It would be beneficial to further develop this.

References

- [1] Millar, J. and White, R.J., The Structural Integrity of FPSO's/FSU's – A Regulator's View, Proceedings of the 9th Offshore Symposium, 1-4 May 2000, Houston, Texas
- [2] Goranson, U. G., Elements of Structural Integrity Assurance, Fatigue 1994, Volume 16, Number 1 pp. 43-65
- [3] Van der Cammen, J.J., Kaminski, M.L., Krekel, M.H., FPSO Fatigue analysis: comparison between prediction and measurements, Proceedings of the 11th Offshore Symposium, February 17 2002, Houston, Texas
- [4] Bea, R.G., Marine structural integrity programs, Marine Structures 7, 1994, pp. 51-76
- [5] Shinozuka, M., Relation of inspection findings to fatigue reliability, Ship Structure Committee Report SSC-355, 1990
- [6] Bea, R.G., Human & organisational factors in reliability of 'minimum' offshore structures, OMAE 2002 conference Oslo, paper OMAE2002-28198
- [7] Brookings, M, Barltrop, N., Ship structural management for improved safety, International conference on tankers and bulk carriers – The way ahead, 1992
- [8] Brook, A.K., Improving the safety of tankers and bulk carriers through a hull condition monitoring scheme, International conference on tankers and bulk carriers – The way ahead, 1992
- [9] Francois, M., Mo., O., Fricke, W., Mitchell, K., Healy, B., FPSO Integrity: comparative study of fatigue analysis methods, Offshore Technology Conference 2000, Houston, Texas
- [10] ABS, Report on the development of a unified procedure for fatigue design of ship structures, American Bureau of Shipping, 1995

References

- [11] DNV 1998 Fatigue assessment of ship structures, Det Norske Veritas, Classification Notes 30.7, Oslo, Norway
- [12] Basar, N.S., Jovino, V.W., Guide for ship structural inspection, Ship Structure Committee Report SSC-332, 1990
- [13] Ma, K., Orisamolou, I.R., Bea, R.G., Huang, R.T., Towards optimum inspection strategies for fatigue and corrosion damage, SNAME Transactions, Vol. 105, 1997, pp. 99-125
- [14] Shinozuka, M., Relation of inspection findings to fatigue reliability, Ship Structure Committee Report SSC-355, 1990
- [15] Demsetz, L., Cario, R., Schulte-Strathaus, R., Inspection of marine structures, Ship Structure Committee Report SSC-389, 1996
- [16] Cramer, E. H., Loseth, R., Olaisen, K., Fatigue assessment of ship structures, Marine Structures 8 (1995) pp. 359-383
- [17] MacMillan, A., Effective FPSO/FSO hull structural design, Offshore Technology Conference, Houston, 2000
- [18] S. Bultema et al, OTC 12142 'FPSO Integrity: JIP on FPSO Fatigue Loads', May 2000
- [19] I. Lotsberg OTC 12145 'FPSO Capacity JIP', May 2000
- [20] Van den Boom, H., Krekel, M., Aalberts, P., OTC 12143 'FPSO Integrity: Structural Monitoring of 'Glas Dowr'', May 2000
- [21] M. Francois et al, OTC 12144 'FPSO Integrity: Comparative Study on Fatigue Load Predictions', May 2000
- [22] François, M., Morandini, C., Gorf, P. and Lewin, M., Relative heading of a FPSO in harsh environment, OMAEFPSO'04-0043, September 2004
- [23] Lotsberg, I., Recommended Methodology for Analysis of Structural Stress for Fatigue Assessment of Plated Structures, OMAE-FPSO'04-0013

-
- [24] IIW, Fatigue Design of Welded Joints and Components – Recommendations of IIW Joint Working Group XIII-1539-96/XV-845-96, edited by A. Hobbacher Abington Publishing, The International Welding Institute, 1996
- [25] Hong, J.K., Dong P., Hot Spot Stress and Structural Stress Analyses of FPSO Fatigue Details, OMAE-FPSO'04-0023
- [26] Komen, G.J., Forecasting wind-driven ocean waves, from ocean forecasting – conceptual basis and applications, edited by Nadia Pinardi and John Woods, Springer 2000
- [27] British Maritime Technology Ltd 'global wave statistics', BMT Group, <http://www.globalwavestatisticsonline.com>
- [28] Massel, S.R., Brinkman, R.M., On the determination of directional wave spectra for practical applications, Applied Ocean Research 20 (1998) pp. 357-374
- [29] Alves, J.H.G.M., Melo, E., On the measurement of directional wave spectra at the southern Brazilian coast, Applied Ocean Research 21 (1999) pp. 295-309
- [30] Massel, S.R., Brinkman, R.M., On the determination of directional wave spectra for practical applications, Applied Ocean Research 20 (1998) pp. 357-374
- [31] Alves, J.H.G.M., Melo, E., On the measurement of directional wave spectra at the southern Brazilian coast, Applied Ocean Research 21 (1999) pp. 295-309
- [32] Aage, C., Allan, T.D., Carter, D.J.T., Lindgren, G., Olagnon, M., Ocean from space – a textbook for offshore engineers and naval architects, published by Ifremer, France, September 1998
- [33] The WAMDI Group, The WAM model – A third-generation ocean wave prediction model, Journal of Physical Oceanography Vol. 18 (December 1988) pp. 1775-1810
- [34] Cox, A.T., Swail, V.R., A global wave hindcast over the period 1958-1997: Validation and climat assessment, Journal of geophysical research, Vol. 106, No. C2, pp. 2313-2329, 15 February 2001

- [35] Thomas, J.P., Retrieval of energy spectra from measured data for assimilation into a wave model, *Quart. J. R. Met. Soc.* (1988), 114 pp. 781-800
- [36] DnV Classification Notes 30.5 – Environmental Conditions and Environmental Loads, March 2000
- [37] Tucker, M.J., and Pitt, E.G., *Waves in ocean engineering*, Published by Amsterdam Elsevier, 2001
- [38] Baar, J.M., Heyl, C.N., Rodenbusch, G., Extreme responses of turret-moored tankers, Paper OTC2000-12147, Offshore Technology Conference 2002, Houston, Texas
- [39] Nordstrom, C.D., Grant, B., Lacey, P.B., Hee, D.D., Impact of FPSO heading on fatigue design in non-collinear environments, paper OMAE2002-18133, OMAE 2002 Conference Oslo, Norway
- [40] De Souza Jr., J.R., Morishita, H.M., Dynamic behaviour of a turret FPSO single and tandem configuration in realistic sea environments, Paper OMAE2002-28134, OMAE 2002 Conference Oslo, Norway
- [41] Vestbostad, T., Andersen, A.J., Haver, S., Albert, A., Prediction of extreme roll motion on an FPSO using long-term statistics, Paper OMAE2002-28117, OMAE Conference 2002, Oslo, Norway
- [42] Van der Cammen, J.J., Hoogeland, M., Koning, J., Comparison of measured and calculated vessel heading of a turret-moored FPSO, Submitted for publication in Proceedings of the 12th Offshore Symposium, February 19 2003, Houston, TX, Texas Section of the Society of Naval Architects and Marine Engineers
- [43] OCIMF, 2nd edition –Prediction of wind and current loads on VLCCs, 1994
- [44] Hsao, H, Chen, S.S., Correlation of theoretical and measured hydrodynamic pressures for SL-7 containership and the Great Lakes bulk carrier S.J. Cort, Ship Structure Committee Report SSC-325, 1984
- [45] Friis Hansen, P., Winterstein, S.R., Fatigue damage in the side shells of ships, *Marine Structures* 8 (1995), pp. 631-655

-
- [46] Cramer, E.H., Loseth, R., Bitner-Gregersen, E., Fatigue in side shell longitudinals due to external pressure, Proceedings of the OMAE Conference 1993 – Volume II, Safety and Reliability
- [47] Ren, B., Wang, Y., Spectral analysis of irregular wave impact on the structure in splash zone, OMAE 2002 conference Oslo, paper OMAE2002-28091
- [48] Følso, R., Spectral fatigue damage calculation in the side shells of ships, with due account taken of the effect of alternating wet and dry areas, Marine Structures 11 (1998) pp. 319-343
- [49] Journée, J.M.J., Massie, W.W., Offshore Hydromechanics, first edition, January 2001
- [50] ASTM Designation E1049-85 (re-approved 1990), standard practices for cycle counting in fatigue analysis
- [51] Van der Cammen, J.J., Francois, M., Kaminski, M.L., Is Uncertainty of Wave Induced Fatiguing Loading on FPSOs Uncertain?, OMAE-FPSO'04-0055
- [52] Clarke, J.D., Wave loading in warships, Advances in Marine Structures, 1986
- [53] Guedes Soares, C., Schellin, T.E., Long term distribution of non-linear wave induced vertical bending moments on a containership, Marine Structures 9 (1996), pp. 333-352
- [54] Wu, M., Hermundstad, O.A., Time domain simulations of wave-induced non-linear motions and loads and its Application in Ship Design, Marine Structures 15 (2002), pp. 561-597
- [55] Brown, J.C., A Wave-induced fatigue strain recorder for surface ships, 1999
- [56] Marine Report 13170-20-TM - Dynamic pressure loading in cargo and ballast tanks on board Glas Dowr (analysis no 1), July 1999
- [57] Bishop, R.E.D. and Pryce, W.G., Probabilistic theory of ship Dynamics, Published by Chapman and Hall, London, 1974

- [58] Ochi, M.K., Applied probability and stochastic processes in engineering and physical sciences, John Wiley & Sons, Inc., 1990
- [59] Marin Report 13170-08-OE - Diffraction and Dynforc calculations on FPSO Glas Dowr, May 1998
- [60] Journée, J.M.J., Theoretical Manual of Seaway, Release 4.19, February 2001
- [61] Lygre, A. and Krogstad, H., Maximum Entropy Estimation of the Directional Distribution in Ocean Wave Spectra, Journal of Physical Oceanography, Volume 16, December 1986
- [62] Robinson, R.W., Stoddart, A.W., An Engineering Assessment of the Role of Non-Linearities in Transportation Barge Roll Response, Trans. RINA, Vol. 129. 1987
- [63] Mathisen, J., Analysis of Experiment and Functional Model for Ship Rolling, A.S. Veritas Report No.90-2000, Reprint of PhD Thesis, 1988
- [64] Kinnas, S.A., Yu, Y.-H., Kacham, B., Lee, H., A Model of the Flow around Bilge Keels around FPSO Hull Sections Subject to Roll Motions, Proceedings of the 12th Offshore Symposium, Texas Section of the Society of Naval Architects and Marine Engineers, February 12 2003, Houston, Texas
- [65] Himeno, Y., Prediction of ship roll damping-state of the art, The University of Mitchigan, Report No. 239, September 1981
- [66] Ikeda, Y., Himeno, Y., Tanaka, N., On eddy making component of roll damping force on naked hull, Journal of the Society of Naval Architects of Japan, 1978
- [67] Gerritsma, J., Golven, Scheepsbewegingen, Sturen en Manoeuvreren 1, June 1994 (in Dutch)
- [68] Brook, A.K., Standing, R.G., A Theoretical and Experimental Investigation of Roll Barge Damping
- [69] Van den Boom, H. and Wichers, J.E.W., leaflet FPSO Roll JIP – reducing the roll motions of floating production units, 2002

-
- [70] Kragtwijk, M.H.J., Vestbostad, T.M., Vugts, J.H., Gudmestad, O.T., On the Sensitivity of the Roll Motion of an FPSO, Proceedings of the OMAE2002, Oslo, Norway
- [71] Ferrari, J.A., Ferreira, M. D. A., Assessment of the Effectiveness of the Bilge Keels as an Anti-Roll Device in VLCC-Sized FPSOs, Proceedings of the Twelfth International Offshore and Polar Engineering Conference (ISOPE), 26-31 May 2002, Kitakyushu, Japan
- [72] Na, J.H., Woo, Lee, W.C., Shin, H.S., Park, I.K., A Design of Bilge Keels for Harsh Environment FPSOs, Proceedings of the Twelfth International Offshore and Polar Engineering Conference (ISOPE), 26-31 May 2002, Kitakyushu, Japan
- [73] Ikeda Y., Himeno Y. & Tanaka N.: "A Prediction Method for Ship Roll Damping", Report of University of Osaka, 1978
- [74] Orozco, J.M., Raposo, C.V., Malenica, S., A Practical Procedure for the Evaluation of the Roll Motions of FPSO's Including the Non-Potential Damping, OTC 2002
- [75] Forestall, G.Z., and Ewans, K., Worldwide Measurements of Directional Wave Spreading, Journal of Atmospheric and Oceanic Technology, Volume 15 (1997), pp. 440-469
- [76] Dijkshoorn, N.A., Determination of Extreme Vertical Wave Bending Moments on FPSO Glas Dowr, M.Sc. Thesis Work, 1999
- [77] Brown, J.C., Clarke, J.D., Recent progress on wave induced loading measurements in warships, Marine Structures 6 (1993)
- [78] Lloyd, A.R.J.M, statistic ship motion recorders, Naval Architect May 1981
- [79] Andrews, R.N., Lloyd, A.R.J.M., Full-scale comparative measurements of the behaviour of two frigates in severe head seas, Naval Architect 1980
- [80] Clarke, J.D., Measurement of hull stresses in two frigates during a severe weather trial, Naval Architect May 1981

- [81] Clarke, J.D., Fatigue crack initiation and propagation in warship hulls, *Advances in Marine Structures* 2, 1993
- [82] Melitz, D.T., Robertson, E.J., Davidson, N.J., Structural performance management of VLCCs – an owner’s approach, *Marine Technology*, Vol. 29, No.4 Oct. 1992 p.p. 250-262
- [83] Witmer, D.J., Lewis, J.W., The BP oil tanker structural monitoring system, *Marine Technology*, Vol. 32, No. 4, Oct 1995 p.p. 277-296
- [84] Ashcroft, F.H., Witmer, D.J., The role of shipboard structural monitoring systems in the design and safe operation of ships, *Prads* 1998
- [85] Lacey, P., Edwards, R., ARCO tanker slamming study, *Marine Technology*, Vol. 30, No. 3, July 1993, pp. 135-147
- [86] Lacey, P., Chen, H., Improved passage planning using weather forecasting, manoeuvring guidance, and instrumentation feedback, *Marine Technology*, Vol. 32, No. 1, January 1995, pp. 1-19
- [87] Slaughter, S.B., Cheung, M.C., Sucharski, D., Cowper, B., State of the art in hull response monitoring systems, *Ship Structure Committee Report SSC-401*, 1997
- [88] Lewis, G., May, R.A., Story, E.D., The application of hull monitoring and ISIT technology to ship safety operation, *SNAME and SSC – Ship Structure Symposium*, 1996
- [89] Sanderson, D.J., Price, A.G., Nelson, A., Killbourn, S., Dougan, A, The application of online monitoring for the assurance of fixed jacket structures’ structural integrity, *OMAE 2002 conference Oslo*, paper OMAE2002-28614
- [90] Piedras Lopez, T.A., Ebecken, N.F.F., In-time fatigue monitoring using neural networks, *Marine Structures* 10 (1997) pp. 363-387
- [91] Vulovich, R., Hirayama, T., Toki, N., Mizuno, H., Characteristics of hull stresses measured on a large containership in rough seas, *SNAME Transactions*, Vol. 97, 1989, pp.397-428

-
- [92] Fain, R.A., Design and installation of a ship response instrumentation system onboard SL-7 class containership SS Sea-Land McLean, Ship Structure Committee Report SSC-238
- [93] Fritch, D.J., Bailey, F.C., Wise, N.S., Results from full-scale measurements of midship bending stresses on two C4-S-B5 dry cargo ships operating in North-Atlantic service
- [94] Xu, J., Haddara, M.R., Estimation of wave-induced ship hull bending moment from ship motion measurements, *Marine Structures* 14 (1999), pp. 593-610
- [95] Burton, B., Verijenko, V., Structural health monitoring in marine structures, OMAE 2002 conference Oslo, paper OMAE2002-28278
- [96] Zubaydi, A., Haddara, M.R., Swamidas, A.S.J., Damage identification in a ship's structure using neural networks, *Ocean Engineering* 29 (2002) pp. 1187-1200
- [97] Rogers, L.M., Crack detection by acoustic emission, *Offshore Engineer*
- [98] Rogers, L.M., Structural and engineering monitoring by acoustic emission methods – fundamentals and applications, *Lloyd's Register Paper* September 2001
- [99] Yuille, I.M., Longitudinal Strength of Ships, *Trans. Royal Inst. Nav. Arch*, 105 (1963) pp 1-33
- [100] HSE Publication 2001/022 – Weather-sensitive offshore operations and metocean data, 2001
- [101] Advances in underwater technology and offshore engineering, volume 4: evaluation, comparison and calibration of oceanographic instruments, Published by Graham & Trotsham Ltd., London 1985
- [102] Atwater, R., Shipboard wave height sensor, Ship Structure Committee Report SSC-362, 1990
- [103] Waals, O.J., Aalbers, A.B., Pinkster, J.A., Maximum likelihood method as a means to estimate the directional wave spectrum and the mean wave drift force on a dynamically positioned vessel, OMAE 2002 conference in Oslo, paper OMAE2002-28560

References

- [104] Tubby, P., and Davenport, J., CrackFirst – a new sensor system to assist structural health monitoring, Connct no 135, March/April 2005, p.2
- [105] Muragishi, O., Fatigue Life Diagnosis of Steel Structures with a Fatigue Damage Sensor, Welding International 2006 20 (2) pp. 95-99
- [106] Grønlie ,Ø., Wave Radars, A comparison of Concepts and Techniques, Hydro International, April 2006
- [107] Grønlie ,Ø., Wave Radars: Techniques and Technologies – Advantages and Disadvantages of Different Ground-Based Radar Remote Sensors, October 2006
- [108] Van den Boom, H., On Board Wave and Motion Estimator – Prediction of Quiescent periods in floater motion to assist motion critical offshore operations, Leaflet of Joint Industry Proposal, 2006
- [109] Blok, J.J., and Huisman, J., Relative Motions and Swell-Up for a Frigate Bow, The Naval Architect, July/August 1984
- [110] Hoogeland, M., Van der Nat, C.G.J.M., and Kaminski, M.L., FPSO Fatigue Assessment: Feedback from In-Service Inspections, OTC 15064, 2003
- [111] Kaminski, M.L., Sensing and Understanding Fatigue Lifetime of New and Converted FPSOs, OTC 18913, 2007-02-19
- [112] Hart, D.K., Rutherford, S.E., Wickham, A.H.S., Structural Reliability Analysis of Stiffened Panels, The Royal Institute of Naval Architects 1985
- [113] Statsoft Inc., Neural Networks, 2003
- [114] Smith, L., An Introduction to Neural Networks, 1996
- [115] Bishop, C.M., Neural Networks for Pattern Recognition, Published by Oxford University Press Inc., New York, Reprinted 2000
- [116] Demuth, H., Beale, M., Neural Network Toolbox for Use with Matlab, User's Guide Version 4, 2004

- [117] Fausett, L.V., Fundamentals of Neural Networks – Architectures, Algorithms, and Applications, Published by Prentice-Hall, Inc., 1994
- [118] Malenica, Š., Zalar, M., Chen. X.B., Dynamic Coupling of Seakeeping and Sloshing, ISOPE 2003-JSC-267, 2003

Appendix A Data for Long-Term Load Calculations

A.1 Diffraction Calculations in FPSO Integrity JIP

Vessel motions and section loads were calculated for FPSO Glas Dowl in full-loaded condition with the 3D diffraction program Diffrac for the FPSO Integrity JIP [59]. The relevant loading condition data is specified in table A.1.

Designation	Symbol	Magnitude	Unit
Length between perpendiculars	L_{pp}	232.00	m
Width	B	42.00	m
Mean draft	T_m	14.307	m
Trim (draft aft-draft fore)	Trim	-0.398	m
Displacement weight	Δ	114,793	tonnes
LCG from midship	LCG	6.59	m
Centre of gravity above base	KG	11.137	m
Transverse metacentric height	GM_t	6.389	m
Transverse radius of gyration in air	K_{xx}	14.94	m
Longitudinal radius of gyration in air	K_{yy}	57.31	m
Vertical radius of gyration in air	K_{zz}	58.13	m
Location of turret centre before $1/2 L_{pp}$	L_t	92.8	m
Frontal wind area	A_F	1616	m^2
Lateral wind area	A_L	4015	m^2

Table A.1 Vessel characteristics

These transfer functions are used in chapter 2 to investigate the influence of the time-trace length on the long-term accumulated load the influence of separate loads. The RAOs are shown for four directions in the figures A1-A8.

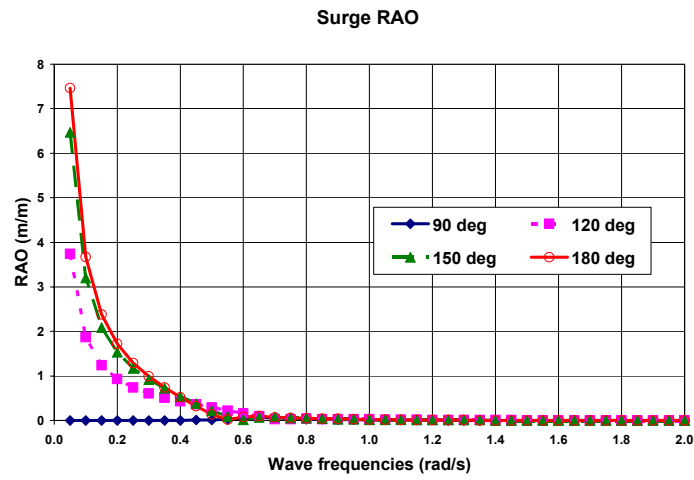


Figure A.1 Surge RAO

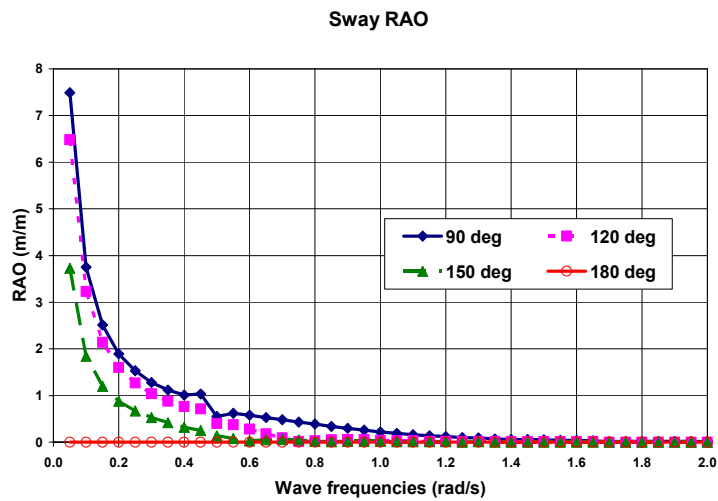


Figure A.2 Sway RAO

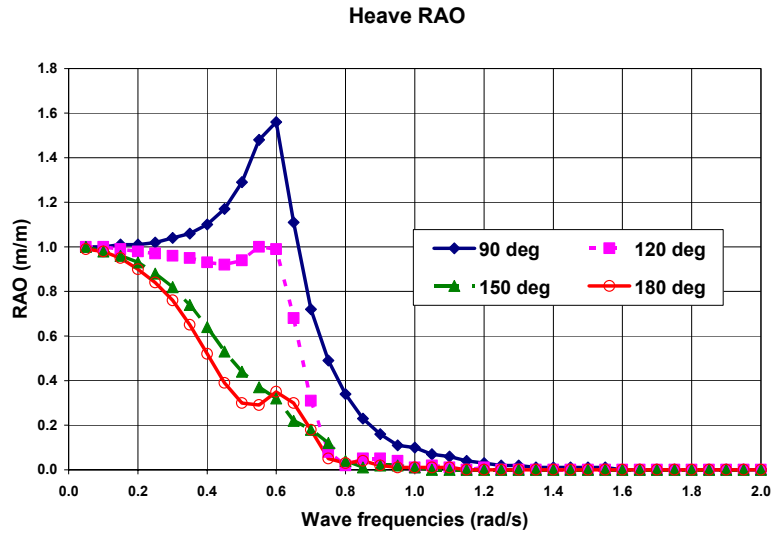


Figure A.3 Heave RAO

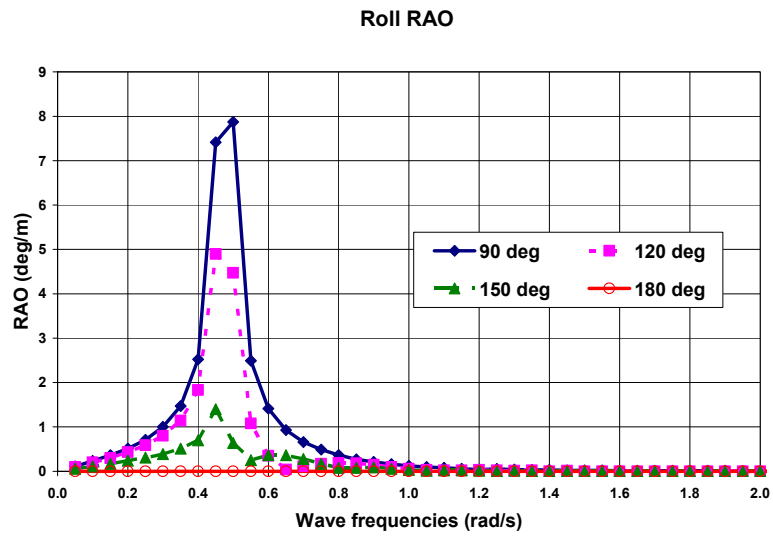


Figure A.4 Roll RAO

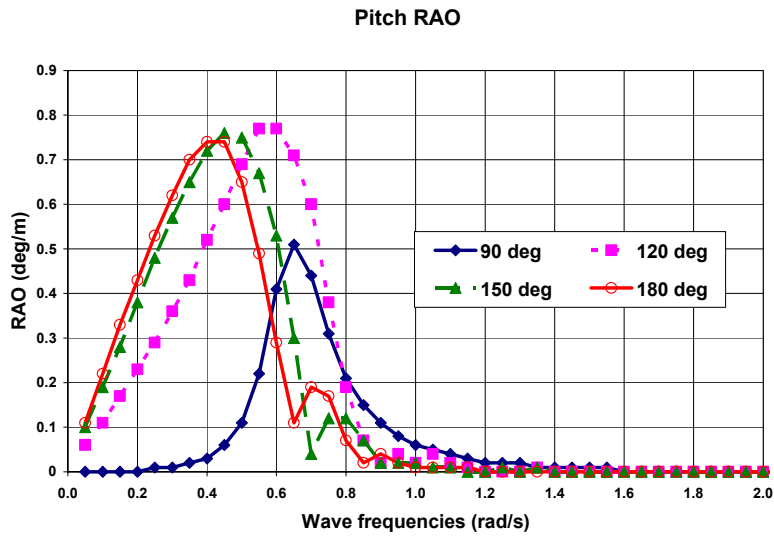


Figure A.5 Pitch RAO

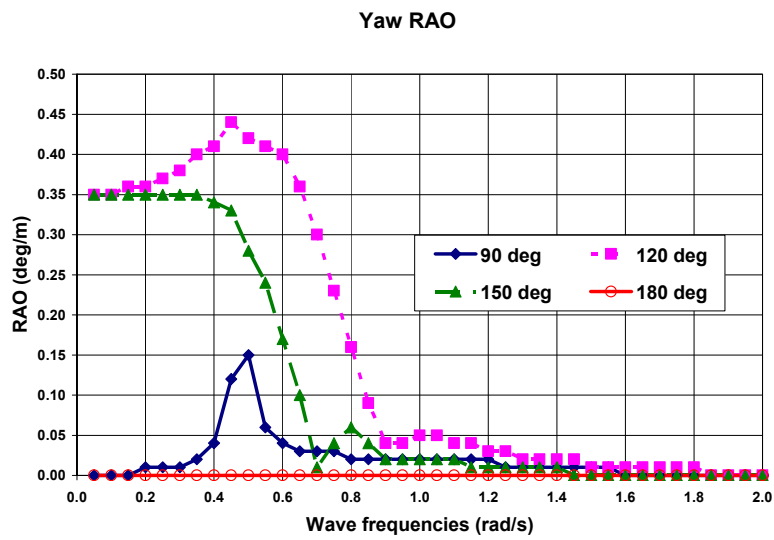


Figure A.6 Yaw RAO

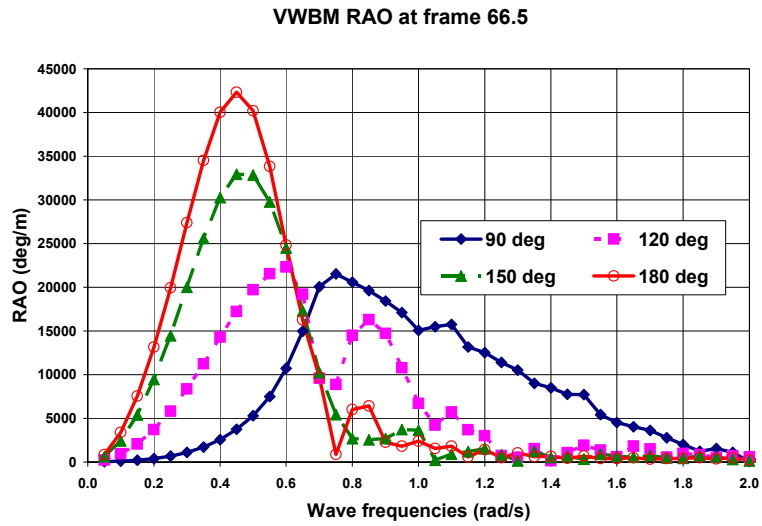


Figure A.7 VWBM RAO at frame 66.5

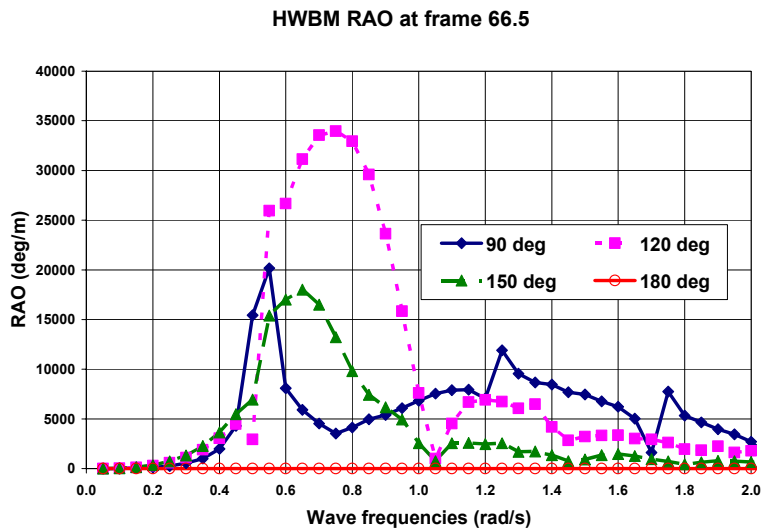


Figure A.8 HWBM RAO at frame 66.5

A.2 Motion Calculations for Operational Loading Conditions

The motion analysis in the FPSO Integrity JIP was performed for a fixed roll-damping value. In reality, the roll-damping depends on the amount of roll motions in the sea-state.

The vessel motions and section loads were calculated in 5 operational loading conditions of Glas Dowl to study influence of the roll-damping and the influence of different loading conditions on the long-term load accumulation. These loading conditions range from ballast load to full-load and are specified in table A.2. The calculations were made with the strip-theory program Seaway [60]. An in-house study confirmed a good agreement between the motion RAOs in Seaway and diffraction theory [76].

	LC 1 (ballast)	LC 2	LC 3	LC 4	LC 5 (fully-loaded)
Draft at midship (m)	8.71	9.90	11.42	13.00	14.85
Trim (m)	2.38	0.72	0.01	0.01	0.41
K-xx (m)	17.87	15.19	14.22	14.00	13.87
k-yy (m)	64.03	59.34	59.50	56.00	53.36
k-zz (m)	64.03	60.62	60.69	58.50	57.45
GM solid (m)	9.12	6.36	5.65	5.00	4.67
GM liquid (m)	8.70	4.79	5.79	4.86	4.31
Occurrence (%)	8.4	22.0	31.2	33.3	5.1

Table A.2 Summary of operational loading conditions

Non-linear roll-damping was evaluated with the method described by Ikeda et al. [73]. Glas Dowlr is fitted with a bilge keel with length 68 m and height of 0.70 m at the Sable field. At the Durward & Dauntless field, the Glas Dowlr was fitted with a bilge keel with a height of 0.35 m. The calculations were made for a range of rollamp values from 1-20 degrees with steps of 1 degree.

A.3 Structural Data

The calculations in chapter 2 are made over the height of the side-shell at $\frac{1}{2} L_{pp}$ PS of Glas Dowlr. Table A.4 specifies the location and structural data for the longitudinals. Table A.5 specifies the structural properties of the hull-girder cross-section.

The pressure coefficients, c_p , are calculated as:

$$c_p = \frac{bl^2}{12W} \quad (A.1)$$

in which c_p is the stress-to-load ratio for wave/ballast pressure to stress, b is the plate width, l is the web-spacing and W is the section modulus of the longitudinal.

The coefficient for the vertical wave bending moment is calculated as:

$$c_{my} = \frac{z - z_0}{I_{YY}} \quad (A.2)$$

in which C_{my} is the stress-to-load ratio for the VWBM, z is the height of the longitudinal above base, z_0 is the height of the neutral axis of the hull-girder above base and I_{YY} is the vertical moment of inertia of the cross-section.

The coefficient for the horizontal wave bending moment is calculated as:

$$c_{mz} = \frac{y}{I_{ZZ}} \quad (A.3)$$

in which C_{mz} is the stress-to-load ratio for the HWBM, y is the lateral distance of the longitudinal to the centreline and I_{ZZ} is the transverse moment of inertia of the cross-section.

This thesis focuses on loading, and therefore no local stress concentration factors have been taken into account in the calculation of the stress-to-load factors.

Longitudinal No#	Height above base (m)	Section modulus (mm³)	Web spacing (mm)	Longitudinal spacing (mm)
Deck	21.20	846733	4800	840
L46	20.36	846733	4800	840
L45	19.52	846733	4800	840
L44	18.68	952416	4800	840
L43	17.84	4808579	4800	840
L42	17.00	1544299	4800	840
L41	16.16	1544299	4800	840
L40	16.34	1230610	4800	840
L38	13.64	1230610	4800	840
L37	12.80	1230610	4800	840
L36	11.96	1230610	4800	840
L35	11.12	1381017	4800	840
L34	10.28	1381017	4800	840
L33	9.44	1544299	4800	840
L31	7.76	615493	2400	840
L30	6.92	615493	2400	840
L29	6.08	615493	2400	840
L28	5.24	615493	2400	840
L26	3.60	615493	2400	840
L25	2.76	615493.3	2400	840
L24	1.92	615493.3	2400	840

Table A.4 Properties of side-shell longitudinals

Property	Value	Unit
I_{zz}	349.8	(m ⁴)
z_0	9.887	(m)
I_{yy}	1102	(m ⁴)

Table A.5 Hull-girder properties

A.4 Environmental Data

A.4.1 Sable Field

Calculations are made for 1500 sea-states at the Sable field, offshore South-Africa. This data covers more than a year. This data set is part of the environmental data used for the design of Glas Dowl at the Sable field. Per sea-state, the wind speed and direction, current speed and direction, significant wave height, mean zero upcrossing period and mean wave direction of wind waves and swell are specified. Wind and wave data are obtained through hindcasting, validated against satellite data. Current data is obtained from correlating wind data with available current measurements using neural network techniques. Each sea-state has a duration of 6 hours. This long duration is due to the coarse spatial resolution of measurement stations at the Southern hemisphere to feed the hindcast model.

Wind waves are modelled with a JONSWAP wave spectrum with a peak factor of 1.5 and swell waves are modelled with a JONSWAP wave spectrum with a peak factor of 4.0. These peak factors are averaged values.

The probability distribution of the significant wave height at the Sable field is shown in figure A.9. The probability distribution of the mean zero upcrossing period at the Sable field is shown in figure A.10.

Probability distribution of significant wave height at Sable field

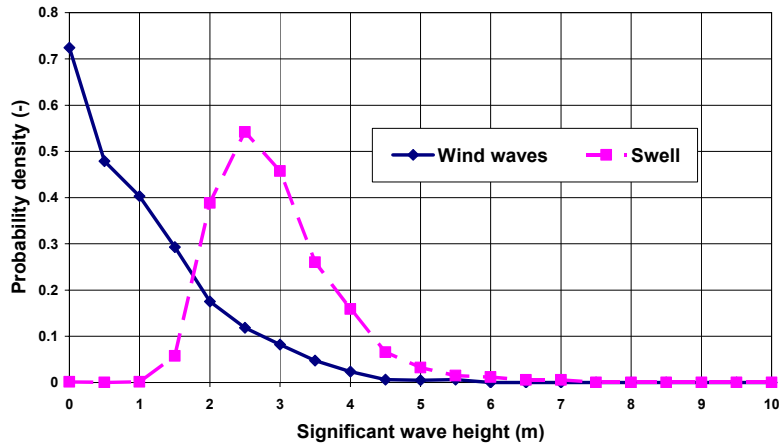


Figure A.9 Distribution of significant wave height at the Sable field

Probability distribution of mean zero upcrossing period at Sable field

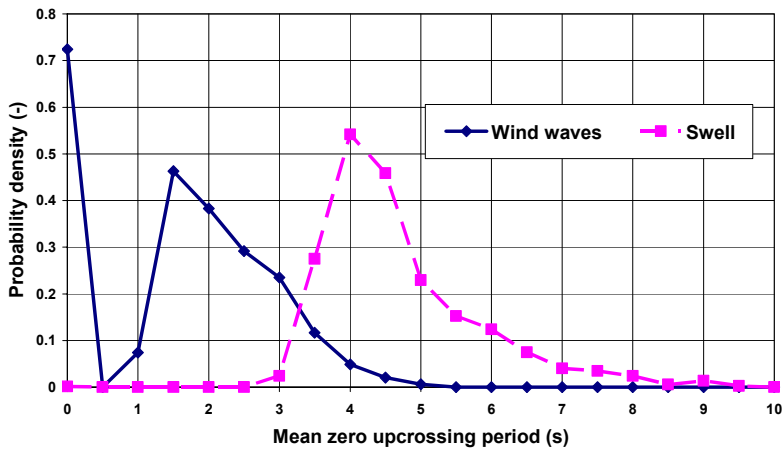


Figure A.10 Distribution of mean zero upcrossing period at the Sable field

A.4.2 Durward & Dauntless Field

The long-term response calculations at the Durward & Dauntless field (UKCS) in chapter 5 are made with 5 years of hindcasted environmental data at the nearby Ross & Parry field. These statistics are specified for 3-hour sea-states. Per sea-state, the wind speed and direction, current speed and direction, significant wave height, mean zero upcrossing period and mean wave direction of wind waves and swell are specified.

Wind waves are modelled with a JONSWAP wave spectrum with a peak factor of 1.5 and swell waves are modelled with a JONSWAP wave spectrum with a peak factor of 4.0. These peak factors are averaged values.

The probability distribution of the significant wave height at the Sable field is shown in figure A.11. The probability distribution of the mean zero upcrossing period at the Sable field is shown in figure A.12.

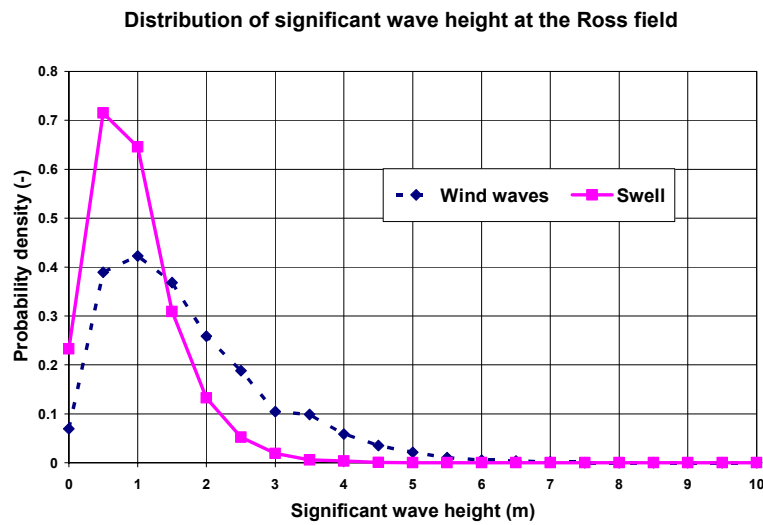


Figure A.11 Distribution of significant wave height at the Ross field

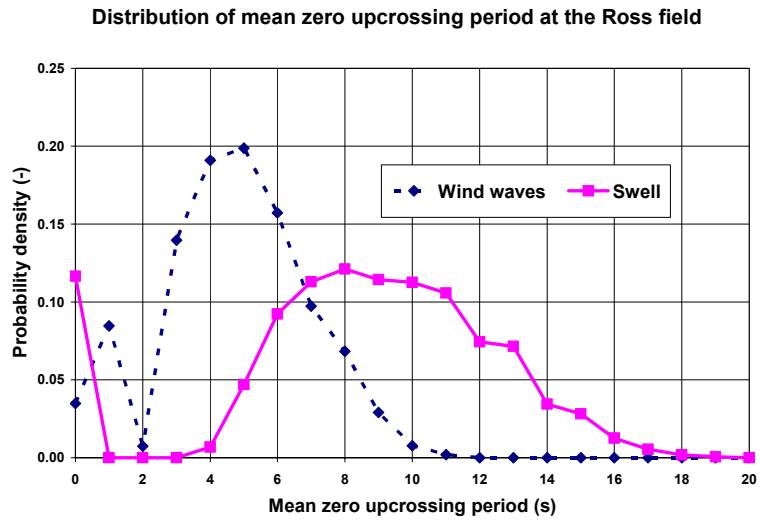


Figure A.12 Distribution of mean zero upcrossing period at the Ross field

Appendix B Sensor Locations

Table B.1 specifies the locations of the deck strain sensors and wave pressure sensors that are used in the case study in chapter 5. The deck strains are recorded with long-based strain gauges (LBSG). A photo of a fitted LBSG onboard Glas Dowr is shown in figure B.1. The wave pressures are measured with pressure gauges fitted in the side-shell of the vessel. Figure B.2 shows a picture of a wave pressure sensor fitted in the side-shell of Glas Dowr.

Sensor	X-location (fore of APP) (m)	Y-location (left from CL) (m)	Z-location (up from base) (m)	Unit
L1	115.250	18.300	21.294	(Microstrain)
L3	187.250	18.300	21.294	(Microstrain)
P1	112.850	21.000	9.860	(bar)
P2	114.050	21.000	5.660	(bar)
P3	114.050	21.000	3.177	(bar)
P19	184.850	21.000	9.860	(bar)
P20	186.050	21.000	5.660	(bar)
P21	186.050	21.000	3.177	(bar)

Table B.1 Location of deck strain sensors and wave pressure sensors



Figure B.1 Long-based strain gauge fitted on Glas Dowr



Figure B.2 Wave pressure sensor fitted on Glas Dowr

Curriculum Vitae

Jeroen van der Cammen was born on 29 December 1975 in Rotterdam, the Netherlands. He went to highschool (atheneum) at the Thomas More College in Oudendijk, and graduated in 1994. After which, he studied Maritime Engineering at Delft University of Technology. He graduated in January 2000 on the subject reliability and ultimate hull girder capacity of FPSOs, in the faculty of ship constructions under the supervision of Prof. ir. B. Boon.

Since then, he has been working with Bluewater Energy Services BV in Hoofddorp. He has been involved with different joint industry projects (JIP) such as the JIP FPSO Integrity, the JIP FPSO Capacity and the JIP FPSO Roll. Furthermore, he has been involved with design work in engineering projects in the field of hydrodynamics and fatigue.

In 2003, Jeroen started his PhD research in the field of fatigue prediction and structural monitoring on FPSOs. This research was a close co-operation between Delft University of Technology, faculty of Hydrodynamics, and Bluewater Energy Services BV. This thesis work is a result of this study.

At the moment, Jeroen is working with Bluewater Energy Services BV in Hoofddorp. He is involved in engineering and research projects in the field of fatigue and hydrodynamics.